THE UNIVERSITY OF CHICAGO

STUDY OF A NOVEL CYANOBACTERIAL CLOCK INTERACTOR KIDA AND THE EFFECT OF RHYTHMIC GLUCOSE ON BETA CELLS

A DISSERTATION SUBMITTED TO
THE FACULTY OF THE DIVISION OF THE BIOLOGICAL SCIENCES
AND THE PRITZKER SCHOOL OF MEDICINE
IN CANDIDACY FOR THE DEGREE OF
DOCTOR OF PHILOSOPHY

GRADUATE PROGRAM IN BIOCHEMISTRY AND MOLECULAR BIOPHYSICS

BY
SOO JI KIM

CHICAGO, ILLINOIS
JUNE 2023

TABLE OF CONTENTS

LIST OF FIGURES vi

LIST OF TABLES viii

ACKNOWLEDGMENTS ix

ABSTRACT xiii

1 INTRODUCTION 1

2 KIDA, A MULTI-PAS DOMAIN PROTEIN, TUNES THE PERIOD OF THE CYANOBACTERIAL CIRCADIAN OSCILLATOR 7
2.1 Foreword 7
2.1.1 Authors and affiliations 8
2.1.2 Author contributions 8
2.2 Abstract 9
2.3 Introduction 9
2.4 Results 11
2.4.1 Identification of KidA via co-IP/MS of Fold-Switched KaiB. 11
2.4.2 The Period of the Circadian Rhythm Varies with KidA Expression Level. 13
2.4.3 KidA Overexpression Alters the Relationship of Entrained Phase to Photoperiod. 14
2.4.4 The N-Terminal Region of KidA Is Composed of Multiple PAS Domains, Which Are Responsible for the Period-Shortening Effect of KidA. 17
2.4.5 KidA Directly Binds Fold-Switched KaiB through PAS Domains In Vitro. 20
2.4.6 Reconstitution of the Period-Shortening Effect of KidA In Vitro. . . . 23
2.4.7 KidA Binding to KaiB in the Fold-Switched Form Shortens the Period in a Mathematical Model. 23
2.5 Materials and methods 31
2.5.1 fsKaiB-HA co-IP/MS. 31
2.5.2 Monitoring In Vivo Clock Rhythms Using Bioluminescence Reporters. 31
2.5.3 Protein Expression and Purification. 32
2.5.4 In Vitro Co-IP and Fluorescence Polarization. 33
2.5.5 Mathematical Modeling. 33
2.6 Discussion 34
2.7 Supporting information 36
2.7.1 Supplementary Materials and Methods 36
2.7.2 Supplementary Information Tables 51
2.8 Acknowledgments 70

3 THE EFFECT OF RHYTHMIC FEEDING OF GLUCOSE ON THE PANCREATIC BETA CELLS . . . 71
3.1 Abstract . . . 71
3.2 Introduction . . . 72
3.3 Preliminary results . . . 75
3.3.1 Beta-TC-6 cells exposed to constantly high or constantly low concentrations of glucose experience growth impairment . . . 75
3.3.2 Local effect of cycling high glucose and optimal glucose on beta-TC-6 cell growth . . . 77
3.3.3 Overall effect of cycling high glucose and optimal glucose on beta-TC-6 cell growth . . . 80
3.3.4 The effect of balancing with mannose . . . 81
3.4 Materials and methods . . . 81
3.4.1 Cell culture . . . 81
3.4.2 Preparation of the beta-TC-6 cells in microplates . . . 81
3.4.3 Glucotoxicity experiment . . . 83
3.4.4 Time-course imaging of cells using Incucyte . . . 84
3.4.5 Analysis of Incucyte data . . . 85
3.5 Discussion . . . 86
3.6 Supporting information . . . 88
3.6.1 Supplementary figures . . . 88
3.7 Conclusions and future directions . . . 89

4 CONCLUDING REMARKS . . . 91

A UNPUBLISHED FOLLOW UP RESULTS FOR KIDA . . . 93
A.1 Settled culture appearance of the KidA-overexpression strain . . . 93
A.1.1 The unique appearance of settled culture of KidA-overexpression strain in a glass tube . . . 93
A.1.2 The unique appearance of settled culture of KidA-overexpression strain in a 24-well microplate . . . 94
A.1.3 Discussion and future directions . . . 96
A.2 Fluorescence polarization of KidA+KaiB reaction . . . 97
A.2.1 Results . . . 97
A.2.2 Discussion and future directions . . . 98
A.3 In vivo interaction of KidA with KaiC throughout the day . . . 99

B APPENDIX TO CHAPTER 2 . . . 101
B.1 Predicted structures of KidA . . . 101
B.2 Additional supplementary data that were not included in Chapter 2 or the published article . . . 104
B.2.1 Including c-di-GMP in the in vitro clock reaction does not affect the period . . . 104

B.2.2 Overexpression of a diguanylate cyclase or a phosphodiesterase does not affect the in vivo clock period 105

REFERENCES 107

LIST OF FIGURES

1.1 KaiABC complex in the day form and the night form 2
1.2 The Kai oscillator and the output pathway 3
1.3 TTFLs in the mammalian clock 4

2.1 KidA is identified as a potential clock interactor from fsKaiB co-IP/MS. 12
2.2 KidA is a putative diguanylate cyclase/phosphodiesterase. 13
2.3 KidA overexpression (KidA-OX) mutants exhibit shorter *in vivo* clock rhythms and altered entrainment. 15
2.4 KidA overexpression strain has IPTG-dependent expression level of KidA protein, and high levels of IPTG induction cause arrhythmicity. 16
2.5 An N-terminal fragment of KidA is sufficient for the clock phenotype and binds to fold-switched KaiB. 18
2.6 PAS-D alignment to LOV and MmoS/NifL domain sequences. 19
2.7 Kinetics of KidA PAS-ABC binding to KaiB. 21
2.8 No obvious inhibition of Kai complex assembly caused by KidA PAS-ABC. . . . 21
2.9 KidA PAS-ABC does not noticeably affect KaiA-stimulated phosphorylation and dephosphorylation of KaiC *in vitro*. 22
2.10 *In vitro* and *in silico* reconstitution of the KidA period-shortening effect. 24
2.11 Dependence of the period and the amplitude on KidA concentration for sampled parameter sets. 26
2.12 Correlation of model parameters with the slopes of the period and amplitude. . 27
2.13 KidA promotes KaiB re-binding to KaiC, which alters the dynamics of phosphorylation in the model. 28
2.14 Shifting the equilibrium between the ground state and fold switched forms of KaiB alters the period and amplitude. 29

3.1 The composition and context of the pancreatic islet within the pancreas. 72
3.2 Cell death of primary rodent beta cells is higher in both hypoglycemic and hyperglycemic conditions. 74
3.3 Beta-TC-6 cell growth is impaired during constant exposure to too-low or too-high concentrations of glucose. 76
3.4 More beta-TC-6 cell death occurs when grown in high concentrations of glucose. 78
3.5 Instantaneous beta-TC-6 cell growth is most affected by the present glucose concentration in cycling glucose condition. 79
3.6 Beta-TC-6 cells grew better in cycling glucose conditions compared to constant glucose conditions. 80
3.7 Mannose rescues beta-TC-6 cell growth impairment in hypoglycemic condition . 82
3.8 Example raw trajectories of beta-TC-6 in cycling or constant glucose 88
3.9 Beta-TC-6 cell growth in optimal glucose concentration after the termination of 48-hour cycling or non-cycling glucose feeding 89

A.1 Appearance of KidA-OX culture settlement at the bottom of the glass tube . . . 94

A.2 Appearance of KidA-OX culture settlement at the bottom of the flat bottom wells in a microplate 95
A.3 Incidents of KidA-OX culture developing a blobby structure 95
A.4 FP signals from the KidA PAS-ABC + FITC-KaiB reaction 97
A.5 Averaged FP values in the saturation regime 98
A.6 The amount of KaiC pulled down by KidA *in vivo* changes throughout the day . 100

B.1 AlphaFold predicted structure of full length KidA colored by confidence score . 102
B.2 AlphaFold predicted structure of full length KidA colored by domain assignment 102
B.3 Predicted 3D structures of individual domains of KidA with PAS-like folds . . . 103
B.4 c-di-GMP addition to the *in vitro* clock reaction 104
B.5 Overexpression of a diguanylate cyclase and a phosphodiesterase does not affect the *in vivo* clock period 105

LIST OF TABLES

2.1 Strains information 51
2.2 List of proteins detected in co-IP/MS experiment performed using fsKaiB as bait in light (L) condition 51
2.3 List of proteins detected in co-IP/MS experiment performed using fsKaiB as bait in dark (D) condition 63
2.4 Model parameters introduced in the modified model. 70

ACKNOWLEDGMENTS

I owe many thanks to multiple individuals for their contribution to my work and life throughout my time in graduate school.

First and foremost, I want to thank Mike Rust, who truly has been the best PI I could have ever asked for. He allowed me to have the freedom to explore different research questions, while always being available for insightful discussion and helpful guidance. It was remarkable to work with a mentor who happily gives a ton of support and inspiration for my growth as a scientist and as a person.

I want to thank the current and previous members of the Rust lab, Gopal Pattanayak, Yi Liao, Lu Hong, Diane Schnitkey, Lily Burton, Steven Wasserman, Chaitra Agrahar, Andrew Schober, Michelle Chiu, and Yujia Liu, for being such great colleagues and friends. I especially want to thank Gopal, who generously trained me with so many techniques in the lab and guided me to try the experiment that led to the discovery of KidA.

I want to thank Chris Chi and Aaron Dinner for their contribution of KidA modeling results, which were highly informative and insightful. I appreciate that we had an ideal collaboration setting where we met regularly and exchange inquiries and suggestions both in experimental and modeling directions, which I think was extremely helpful for efficiently pushing the project forward in optimal directions.

I want to thank my thesis committee, Bob Keenan, Phoebe Rice, and Sean Crosson, for providing me with invaluable expert suggestions for my research and making me feel supported throughout the PhD training. I really enjoyed and appreciated all the communications with my committee members.

I want to thank the researchers of the cyanobacterial clock, especially Drs. Andy LiWang, Carrie Partch, Carl Johnson, and Susan Golden, who generously provided input on the KidA project at various meetings or conferences. Special thanks to Andy for providing a protein that was used for important experiments in the KidA project, and Carrie for providing

invaluable insight on the domain prediction and general feedback for the KidA project. I also want to thank Dr. Stu Brody for his interest, support, and suggestions for the KidA project.

I want to thank Sampriti Mukherjee and her lab for their interest and suggestions for potential future projects on KidA.

I want to thank Nicolas Chevrier and his lab for allowing me to use their equipment for the beta cell glucotoxicity project. I am especially grateful to Adil Mohamed for training me on the cell culture techniques and giving helpful suggestions for my experiments. I also want to thank Katerina Cheronis for answering so many of my questions and all the help she gave me.

I want to thank Bogdan Budnik and Renee Robinson at Harvard Center for Mass Spectrometry for performing and analyzing the mass spec data for the KidA project. I also want to thank Eugene Xu and Chun-Yi Chiang at UChicago Cellular Screening Center for their assistance with my Incucyte experiments for the beta cell glucotoxicity project.

I want to thank the BMB department for granting me the opportunity to do research and pursue a PhD.

I want to thank the student community of BMB for social support and friendship. Special thanks to the students who took on leadership roles to organize fun gatherings or other departmental functions. I also want to give a shout-out to my cohort, Jane Lodwick, Nicole Ladd, Caraline Sepich Poore, and Yujiao Wu, for the camaraderie we built from walking the path of BMB graduate students together.

I want to thank the BMB graduate program administrator Shani Charles for her administrative help throughout the process. I am also grateful to Lisa Anderson, the former BMB graduate program administrator, for her support during my second year when I had to face a lot of hardship from switching labs. I want to thank Joe Piccirilli, the BMB curriculum committee chair, for his support on this matter as well.

I want to thank all my friends at the University of Chicago who gave me lots of joy and comfort. Special thanks to Lindsey Montefiori and Charlie Lang for all the climbing sessions and other fun events indoors and outdoors, to Haneul Yoo, Younghoon Koh, and Boram Lee, for all the relaxing times we had together, to Rebecca Reis, for being such a wonderful neighbor-friend and generous provider of home-cooked meals and desserts, to Jane Lodwick, for being a friend I can rely on to honestly talk about things, to Stephanie Sang, for her generous and loyal friendship and leadership in our multi-department friend group assembled at our first-year Q-bio bootcamp, and Yeonwoo Park and Carlos Marcelo for joining me in following Stephanie's lead, and to the softball teammates Matt Reyer et al. for lots of softball.

I want to thank Dr. Tae Seok Moon for allowing me to work in his lab as an undergraduate and later as a lab technician, as well as the Moon lab members from that time. I learned the joy of research from the experience and got inspired to apply for grad school.

I want to thank Kenneth Ng for our lasting friendship and for having taught me molecular cloning skills. Everything he taught me is still serving me well.

I want to thank all my friends from my childhood, from KMLA, and from Wash U, for their continued friendship and support.

I want to thank my parents, Sang Ho Kim and Young Joong Kim, for their everlasting love and support. They really deserve to be able to spend more time with their children, but instead they gave me full blessing to chart my own path, even if it led me to the opposite side of the globe.

I want to thank my brother, William Sooyong Kim, for always being on my side and trusting me.

I want to thank my mother-in-law Heidi Solz and my father-in-law Roger Kerr for welcoming me without question from the first time we met and showing so much support for my well-being and career.

I am thankful to my dog Maru for being an amazing companion and providing opportunities for mutual growth. He provided me the healthy kind of pressure to always maintain a certain level of physical and mental strength and rewarded me by being a good boy.

Lastly, I want to thank Daniel Kerr, who is my climbing buddy, tennis buddy, co-pet-parent, colleague, and husband, among others. I am grateful for the trust we have in each other and appreciate that I can "believe in him who believes in me" when I have self-doubts.

ABSTRACT

Earth's daily rotation creates a cyclic solar environment to which every living thing is subjected. Naturally, organisms in all kingdoms of life have evolved ways to govern their physiology according to the predictable daily changes of the environment. The external daily rhythms and internal physiological rhythms are coordinated by circadian clocks, biochemical oscillators with 24-hour periods. Circadian clocks regulate numerous pathways that are important for the survival of organisms such that their disruption can lead to fitness defects. The aim of my research was to expand our understanding of the connection of the circadian clock to the physiological processes that it regulates. In Chapter 2, I report our discovery of KidA, a novel interactor of the well-studied cyanobacterial circadian clock, which has an unexpected ability to tune the period of the clock. We unveil molecular details of the KidA-clock interaction and the period-tuning using *in vivo*, *in vitro*, and *in silico* methods. Containing multiple PAS domains, KidA has the potential to serve as an integrator of multiple environmental signals including the time-of-day information, motivating further research investigating its broader roles in the cell. Chapter 3 discusses my exploration of how glucose rhythms affect pancreatic beta cells, which perform important roles in glucose homeostasis through clock-regulated mechanisms. Prolonged exposure to consistently high concentration of glucose has a detrimental effect on beta cell function and survival and is linked to Type 2 Diabetes. The preliminary *in vitro* results from beta-TC-6 cells suggest that such glucotoxicity experienced by beta cells can be alleviated by cycling high glucose and low glucose treatments in a circadian manner, similar to the time-restricted feeding approach.

CHAPTER 1

INTRODUCTION

Circadian clocks are 24-hour biochemical oscillators that coordinate various biological processes with the daily solar cycles of the Earth. Prolonged disruption of circadian clocks have been shown to have detrimental effects on the fitness of different organisms [1, 2, 3].

Generally, chronobiologists use three criteria to define a circadian clock: 1. It should be able to free-run, 2. It should be temperature-compensated, and 3. It should be entrainable [4, 5]. If the oscillation persists in a constant environment, without receiving any external signal, it is called a free-running rhythm. The ability to free-run allows robust clock control, because the clock can continue outputting rhythms even when the organism is removed from an environment that provides regular timing cues. Temperature compensation describes the ability of the clock to maintain its period across a range of temperatures. Being robust against temperature fluctuations is not a trivial challenge for a biological clock composed of multiple biochemical reactions, but a temperature-compensated clock can perform its normal function even when the ambient temperature fluctuates and drifts. Lastly, entrainability refers to the ability of the circadian clock to synchronize with the environmental signal, aligning the internal time-of-day information to match the actual time. Together, these properties provide robustness to the circadian clock by allowing the clock to anticipate expected changes in the environment, such as changes in the light intensity or temperature, throughout the day.

Different organisms have different clock systems, although there are some shared design principles [1, 6]. Among them, cyanobacteria have the simplest known clock composed of only three proteins, KaiA, KaiB, and KaiC. *S. elongatus* PCC 7942, the organism in which the kai genes were first discovered, serves as the model organism for the cyanobacterial circadian clock [7]. Post-translational mechanisms involving the three Kai proteins are sufficient to drive the oscillation, which engenders the remarkable *in vitro* reconstitutability of the Kai

oscillator. Simply by mixing the three purified proteins in ATP-containing buffer, one can reproduce $\sim$ 24 hour rhythms in a test tube [8]. Multiple investigations from the fields of structural biology, biochemistry, genetics, and others over the past couple of decades have revealed the molecular details of the Kai oscillator, which is briefly summarized below.

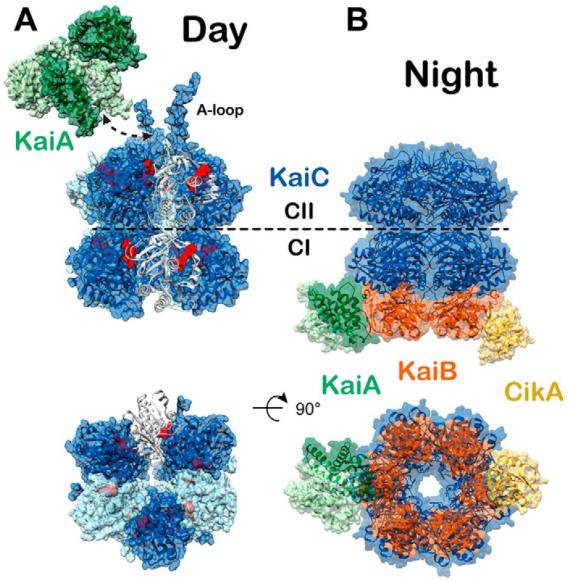

Figure 1.1: KaiABC complex in the day form and the night form (Reproduced from [9]).

The distinct molecular state of the Kai proteins that cycles in a 24-hour period encodes the time-of-day information. KaiC, a hexameric ATPase, is the core pacemaker of the cyanobacterial clock. It takes a double-doughnut structure composed of two halves, CI domain and CII domain. Two residues in KaiC get sequentially phosphorylated and dephosphorylated in a specific order [10], driven by the interaction of KaiC with KaiA and KaiB. When KaiA is bound to the CII domain of KaiC, it stimulates the autophosphorylation of KaiC. On the other hand, KaiB binding the CI domain of phosphorylated KaiC sequesters KaiA, leading to autodephosphorylation of KaiC.

The binding of KaiB to KaiC involves fold-switching of KaiB, in which the protein goes through both secondary and tertiary structure shift into a thioredoxin fold [11]. As KaiC gradually gets dephosphorylated, KaiB dissociates from KaiC and returns the clock back to the initial state of the cycle. In this slow cyclic biochemical reaction, KaiC in KaiA-CII

associated state marks the daytime, and KaiB-CI associated, KaiA-sequestered state marks the nighttime (Figure 1.1) [9].

The clock state information is transferred to RpaA, a master transcriptional regulator that drives genome-wide rhythmic gene expression [12, 13]. The switching of RpaA between its phosphorylated DNA-binding active form and its unphosphorylated inactive form is regulated by two antagonistic histidine kinase proteins, SasA and CikA [14]. SasA, which has a thioredoxin fold like fold-switched KaiB, binds phosphorylated KaiC and in turn phosphorylates RpaA. CikA associates with KaiC-bound KaiB and stimulates dephosphorylation of RpaA. The cyanobacterial clock can be entrained by metabolic signals; resetting of the

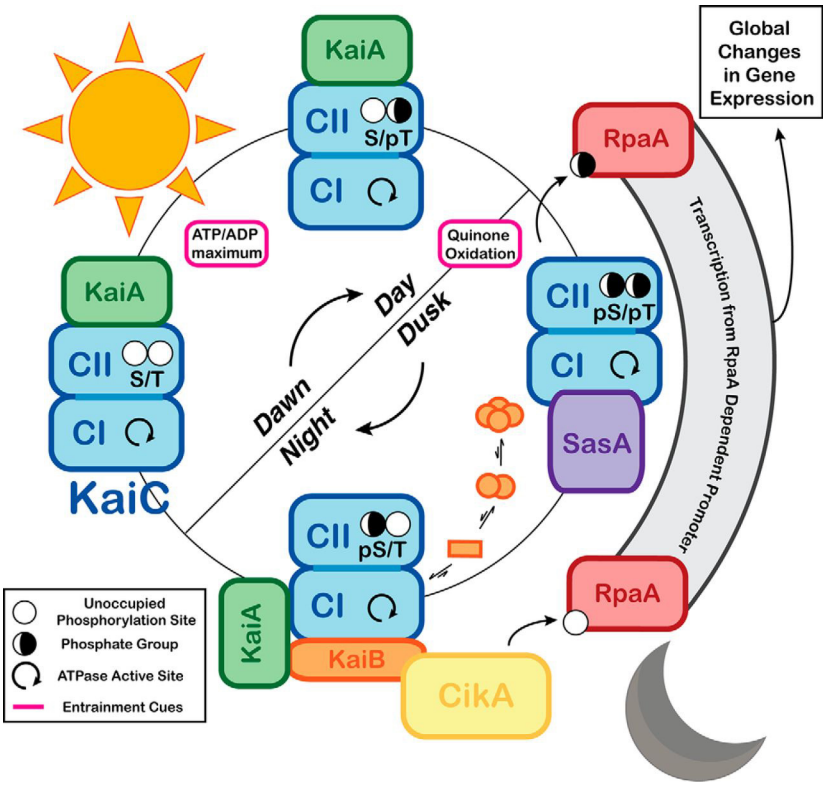

Figure 1.2: The Kai oscillator and the output pathway (Reproduced from [9]).

clock was shown to be possible by changing the ATP/ADP ratio [15] and the redox state of the quinone [16]. The molecular changes of the core oscillator and the output pathway throughout the day are summarized in Figure 1.2 [9].

Unlike the cyanobacterial clock composed of a single oscillator, some organisms have multiple oscillators that perform the function of the circadian clock. For example, mammalian circadian biology involves the central pacemaker residing in the brain and multiple peripheral clocks in other organs [1, 3]. Mechanistically, while the core cyanobacterial clock is a PTO (post-translational oscillator), mammalian clocks are composed of TTFLs (transcription-translation feedback loops) [3]. The components of the core clock and their relationship are summarized in Figure 1.3. Briefly, the core mammalian clock is composed of transcription factors, BMAL1 and CLOCK. The BMAL1:CLOCK complex binds Enhancer box (E-box) sequences to drive rhythmic expression of clock-controlled genes (CCGs), including Period (PER) and cryptochrome (CRY), which in turn inhibit the BMAL1:CLOCK. There are additional layers of feedback, including ROR and REV-ERB that regulate Bmal1 gene transcription and epigenetic regulations through methylation and acetylation (Figure 1.3).

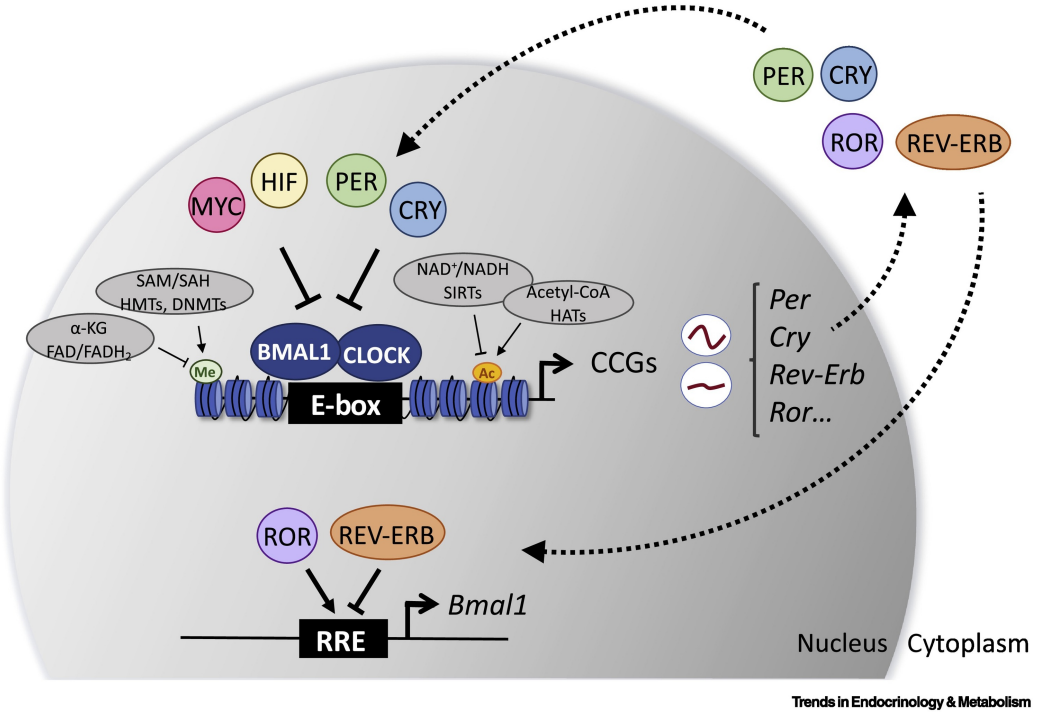

Figure 1.3: TTFLs in the mammalian clock (Reproduced from [17]).

In both the cyanobacterial clock and the mammalian clock systems, we have a relatively

good understanding of the timekeeping mechanism of the key oscillators. There is also a growing list of cellular and physiological processes that are clock-controlled.

In cyanobacteria, links were found between the clock and glycogen storage [18], DNA replication [19], natural competence [20], protein condensation [21], defense against oxidative stress [22], cell division [23], UV resistance [24] and chromosome compaction [25], in addition to the fitness defect observed when the internal clock and the external light-dark cycle were mismatched [26].

Even in physiological processes that are identified to be clock-controlled, the molecular pathway between the clock molecules and the effector systems that give rise to the physiology is often not fully understood. A particularly interesting question is how the cyanobacterial cells would regulate clock-associated physiology during the night during which mRNA levels are globally repressed [13] and transcriptional or translational regulation could be tricky. Inspired by this question, I attempted to find previously unknown protein interactors of the clock, which might have the ability to relay clock information via post-translational mechanisms. This line of work culminated in the discovery of KidA, a novel interactor of the cyanobacterial clock, reported in Chapter 2.

In mammals, circadian disruptions are implicated in various health defects including metabolic disorders such as Type 2 Diabetes, cardiovascular diseases, and cancer [27, 28, 17], rendering the consideration of the circadian clock an important factor in disease prevention and treatment. Time-restricted feeding is an example of intervention methods designed to boost the normal function of the circadian clock [29]. Multiple studies showed health benefits associated with time-restricted feeding or eating, in which subjects consume food only within a limited time window each day. The effect of time-restricted feeding is understandable considering that various metabolic processes are under the regulation of circadian clock [30]. On a similar note, there are reports of detrimental effects when there is a circadian misalignment between the feeding rhythms and the environment [31, 32]. Such mismatches between

behavioral rhythms that influence the peripheral clocks and the environmental cues such as light that influence the master clock likely contribute to elevated health risks associated with shift work and jet lag.

Inspired by the apparent importance of the circadian clock in metabolic regulation and the power of clock-minded intervention, I sought to study the potential interplay of the rhythm of nutrient intake and circadian control in pancreatic beta cells, which perform crucial functions in maintaining glucose homeostasis and whose failure leads to Type 2 Diabetes. Indeed, it was inferred that circadian disruption contributes to insulin resistance based on a large body of evidence [33, 34]. Among many interesting questions concerning the clock-regulated processes in beta cells and Type 2 Diabetes, I investigated the effect of different glucose concentrations and glucose rhythms on beta cells using immortalized cell lines. This question is particularly interesting, considering we might get cellular level insight on the effect of time-restricted feeding approach. Preliminary results from this line of work are reported and discussed in Chapter 3.

CHAPTER 2

KIDA, A MULTI-PAS DOMAIN PROTEIN, TUNES THE PERIOD OF THE CYANOBACTERIAL CIRCADIAN OSCILLATOR

This chapter was published as Kim et al. 2022 [35]

doi:10.1073/pnas.2202426119

2.1 Foreword

The KaiABC oscillator is one of the best understood circadian clock systems. Not only the molecular details of the core oscillator but also the key output regulators that drive rhythmic transcription are well documented. However, there still are under-explored areas in the circadian biology of cyanobacteria, especially regarding how the clock interfaces with other systems in the cell. We hypothesized that there could be previously undocumented protein-protein interaction-based mechanisms by which the cyanobacterial circadian clock can interface with the downstream processes. Our search for potential players involved in such interplay with the clock led to the line of investigation shown in this chapter, beginning with the discovery of a novel interactor of the clock, followed by the unveiling of the clock properties it modulates and the underlying mechanism. The protein of interest, KidA, has numerous intriguing implications and potential regulatory roles in the broader physiology, which are explored in the Discussion section of this chapter as well as the Appendix.

In the following sections of this chapter, the entire content of the article published in [35] appears with minor formatting changes, including the arrangement of both main figures and supporting figures within the main body of text. Additional unpublished information related to KidA is included in the Appendices: Preliminary follow up experiments are reported and discussed in Appendix A, and extra information that supplements materials covered in this

chapter is attached in Appendix B.

The co-authors of the published article [35] and their contributions are listed below.

2.1.1 Authors and affiliations

Soo Ji Kim[a], Chris Chi[b], Gopal Pattanayak[c], Aaron R. Dinner[b,d,e], and Michael J. Rust[c,d,f]

[a]Department of Biochemistry and Molecular Biology, The University of Chicago

[b]Department of Chemistry, The University of Chicago

[c]Department of Molecular Genetics and Cell Biology, The University of Chicago

[d]Institute for Biophysical Dynamics, The University of Chicago

[e]James Franck Institute, The University of Chicago

[f]Department of Physics, The University of Chicago

2.1.2 Author contributions

Conception of the initial co-IP/MS approach: G.P., M.J.R.

Experimental data: S.J.K.

(G.P. contributed the fsKaiB overexpression strain used in co-IP/MS)

Modeling data: C.C.

Experimental and modeling design/data analysis discussions: S.J.K., C.C., M.J.R., A.R.D

Data analysis: S.J.K.

Writing the paper: S.J.K., C.C., M.J.R., A.R.D

Grant acquisition and advisory support: M.J.R., A.R.D

The authors declare no competing interest.

2.2 Abstract

The cyanobacterial clock presents a unique opportunity to understand the biochemical basis of circadian rhythms. The core oscillator, composed of the KaiA, KaiB, and KaiC proteins, has been extensively studied, but a complete picture of its connection to the physiology of the cell is lacking. To identify previously unknown components of the clock, we used KaiB locked in its active fold as bait in an immunoprecipitation/mass spectrometry approach. We found that the most abundant interactor, other than KaiC, was a putative diguanylate cyclase protein predicted to contain multiple Per-Arnt-Sim (PAS) domains, which we propose to name KidA. Here we show that KidA directly binds to the fold-switched active form of KaiB through its N-terminal PAS domains. We found that KidA shortens the period of the circadian clock both *in vivo* and *in vitro* and alters the ability of the clock to entrain to light-dark cycles. The dose-dependent effect of KidA on the clock period could be quantitatively recapitulated by a mathematical model in which KidA stabilizes the fold-switched form of KaiB, favoring rebinding to KaiC. Put together, our results show that the period and amplitude of the clock can be modulated by regulating the access of KaiB to the fold-switched form.

2.3 Introduction

Circadian rhythms are internally generated oscillations that allow organisms throughout the tree of life to anticipate the daily cycle in their environments. These systems typically include a core pacemaker along with a suite of additional factors responsible for transducing signals into and out of the oscillator. While much is now understood about the basic mechanisms that produce rhythms, a full picture of the extended clock network in any organism is missing. Cyanobacteria have emerged as a model system for studying circadian rhythms where genetic analysis is straightforward and biochemical mechanism is uniquely accessible.

The core circadian pacemaker can be reconstituted with a mixture of three proteins, KaiA, KaiB, and KaiC, and phosphorylation rhythms in this purified system show many of the properties of the intact clock [8, 15, 36]. The ability to add precisely defined components to this test-tube clock allows us to characterize how the core oscillator interacts with other components, making it a powerful tool to map out the circadian organization of the entire cell. This approach has been successfully used to extend the KaiABC oscillator to study the role of two signaling kinases, SasA and CikA, that regulate the phosphorylation status of a key output transcription factor RpaA [37]. However, our understanding of the full circadian regulatory network and its relationship to the purified oscillator is far from complete.

Biochemical analysis of the Kai oscillator has made it clear that some interactions are regulated to occur only at specific clock times. This presents a challenge for protein-protein interaction studies because some protein complexes may not form unless the oscillator can be trapped in a physiologically relevant state. A key difference between the daytime and nighttime forms of the oscillator complex is that KaiB fold-switches into an alternative secondary structure to interact with KaiC during the subjective night. KaiB mutants that are locked into this fold (fsKaiB) have been used to success- fully capture protein complexes for structural analysis [11, 38].

In this study, we sought to identify previously unknown components that interact with the Kai oscillator using an fsKaiB mutant as bait for coimmunoprecipitation from native cell lysate. This strategy has the potential to detect interactors that may have escaped previous screens, including hypothetical nighttime signaling pathways, a phase of the cycle where clock physiology is poorly understood. This approach led us to identify a previously uncharacterized protein, which we named KidA, as an interactor of the Kai oscillator. We show that deleting *kidA* or increasing the expression level of KidA leads to changes in the properties of the clock, including a dose-dependent shortening of the period. This shortening of the period is due to direct interaction of KidA with the Kai proteins and can be reconstituted

in vitro. We trace this interaction to the N-terminal PAS domains of KidA, which bind to fold-switched KaiB. The trends in period and amplitude emerge with little parameter tuning when we introduce terms representing KidA binding to and stabilizing fold-switched KaiB to a molecularly detailed mathematical model of the Kai oscillator. This suggests that this mechanism is sufficient to account for the observed behavior. Put together, our results both qualitatively and quantitatively show how regulating the switching of a protein fold can tune the oscillator and how the clock may couple to other systems within the cell.

2.4 Results

2.4.1 Identification of KidA via co-IP/MS of Fold-Switched KaiB.

To search for previously unknown clock interactors, we utilized a coimmunoprecipitation/mass spectrometry (co-IP/MS) approach using a *Synechococcus elongatus* strain expressing an epitope-tagged KaiB mutant that constitutively adopts a fold-switched secondary structure found in KaiB-KaiC complexes (Fig. 2.1A). We generated a ranked list of candidate interactors based on the integrated signal intensity in liquid chromatography with tandem mass spectrometry (LC-MS/MS) for all peptides derived from a given protein, excluding KaiB itself and proteins found in a negative control wildtype sample. The strongest signal came from the core clock protein KaiC, known to interact directly with KaiB. Other oscillator components and known clock interactors, KaiA, CikA, LdpA, and SasA ranked #5, #118, #179, and #182, respectively. Unexpectedly, the protein with the second highest intensity was a previously uncharacterized protein that corresponds to Synpcc7942_1859 (Fig. 2.1B and Supporting Information Tables 2.2 and 2.3). Domain prediction of this protein by Basic Local Alignment Search Tool (BLAST) identified C-terminal GGDEF and EAL domains, typically involved in bis-(3'-5')-cyclic dimeric guanosine monophosphate (c-di-GMP) production and hydrolysis. On this basis, we propose to name this gene *kidA* (*k*ai-*i*nteracting

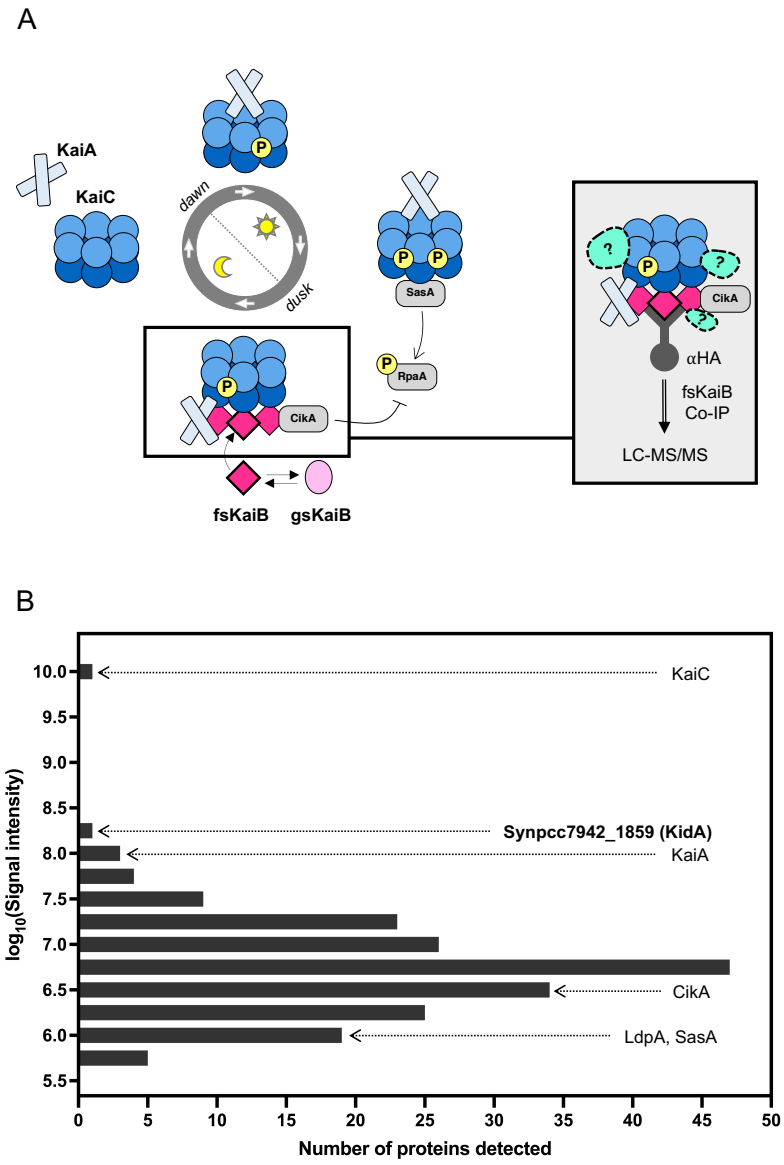

Figure 2.1: KidA is identified as a potential clock interactor from fsKaiB co-IP/MS. (A) Experimental scheme to identify potential interactors of the nighttime state of the cyanobacterial oscillator. (Left) the circadian rhythm manifests as an oscillation of protein complexes. Near dusk, fold-switched KaiB molecules bind to KaiC. (Right) Unknown interactors may be detected by co-precipitation with a fold-switched KaiB mutant (G88A;D90R). (B) Histogram of proteins that were detected in the fsKaiB-HA co-IP/MS with 19x or higher signal intensity compared with the negative control (WT strain). Bins containing Kai proteins, known Kai protein interactors, and a previously undescribed candidate (KidA) are marked on the histogram.

*d*iguanylate cyclase *A*). Alignment of the KidA sequence with enzymes with active GGDEF or EAL domains shows that KidA contains conserved residues needed for enzymatic activity (Fig. 2.2).

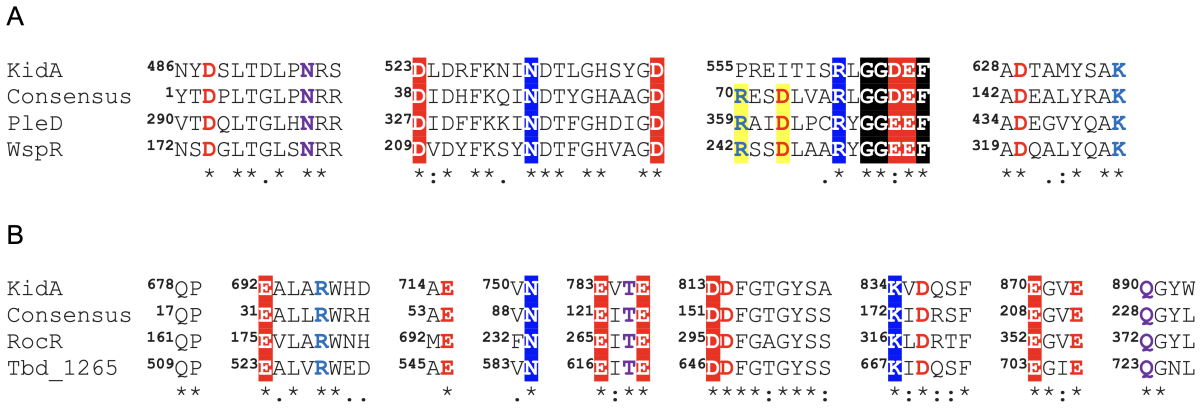

Figure 2.2: KidA is a putative diguanylate cyclase/phosphodiesterase. (A) Multiple sequence alignment of KidA protein sequence, the consensus sequence of the GGDEF domain, and two representative GGDEF domain-containing proteins PleD from Caulobacter vibrioides and WspR from Pseudomonas aeruginosa.(B) Multiple sequence alignment of KidA protein sequence, the consensus sequence of the EAL domain, and two representative EAL domain-containing proteins RocR from Pseudomonas aeruginosa and TBD1265 from Thiobacillus denitrificans. Alignments were created using Clustal Omega [39] and annotated using the same scheme in Figure 4 in Römling et al. [40]: active site residues required for the enzymatic activity are shown in white on a colored background, and other conserved residues near the active site residues are boldened. Yellow background indicates allosteric I site residues.

2.4.2 The Period of the Circadian Rhythm Varies with KidA Expression Level.

To determine the effect of KidA on the circadian rhythm, we monitored the *in vivo* clock rhythms of WT, Δ*kidA*, and inducible overexpression of KidA (KidA-OX) strains using a bioluminescent clock reporter assay (Fig. 2.3A–C and Fig. 2.4A). Induction of KidA led to a marked shortening of the free-running period compared with the wildtype; 10 μM IPTG (Isopropyl β-D-1 thiogalactopyranoside) induction shortened the free-running period by ∼ 3 h (Fig. 2.3A), while Δ*kidA* slightly lengthened the period by ∼2 h (Fig. 2.3B). Moreover,

the period- shortening effect of KidA-OX depended on the concentration of the inducer, up to ∼6 h with maximal induction (Fig. 2.3C). Leaky expression in the absence of inducer showed a smaller but detectable effect. While point mutations in *kaiC* can cause large period changes, the period-shortening effect we observe here is large compared with the effect of known period mutants outside of the *kai* genes themselves [41], e.g., *ldpA* mutants (1 h) [42], *cikA* mutants (2.5 h) [43], and *sasA* mutants (3 h) [44]. The short-period rhythms in the KidA-OX strain at low induction levels retain high amplitude. Above 40 µM IPTG, synchronized rhythms are not sustained after the first three cycles in constant light (Fig. 2.4B).

2.4.3 KidA Overexpression Alters the Relationship of Entrained Phase to Photoperiod.

Conceptually, circadian clocks can be divided into oscillator mechanisms that maintain self-sustaining rhythms and input mechanisms that use signals from the environment to adjust the phase of the oscillation. To determine whether KidA plays an input-specific role in the clock, we first investigated whether KidA affects the entrainment of the clock to different photoperiods. Previous work has shown that a reporter of kaiBC gene expression has a linear dependence of peak phase on day length, with a slope of about 0.5 (midday tracking), when entrained with 24 h cycles of varied photoperiods [36]. We performed a similar experiment using the KidA-OX strain, subjecting the cells to 8:16, 10:14, 12:12, or 16:8 light-dark entrainment cycles. We found that the phase of the *psbAI* reporter signalfrom the KidA-OX strain had a very different dependence on photoperiod (KidA-OX slope m = 0.35) compared with matched wildtype (WT) and Δ*kidA* strains (WT slope m = 0.89, Δ*kidA* slope m = 0.74) (Fig. 2.3D). A change in the slope of entrained phase vs. photoperiod is not expected solely from the shortened free-running period seen in KidA-OX and likely requires a change in the response of the clock to the day-night cycle [36].

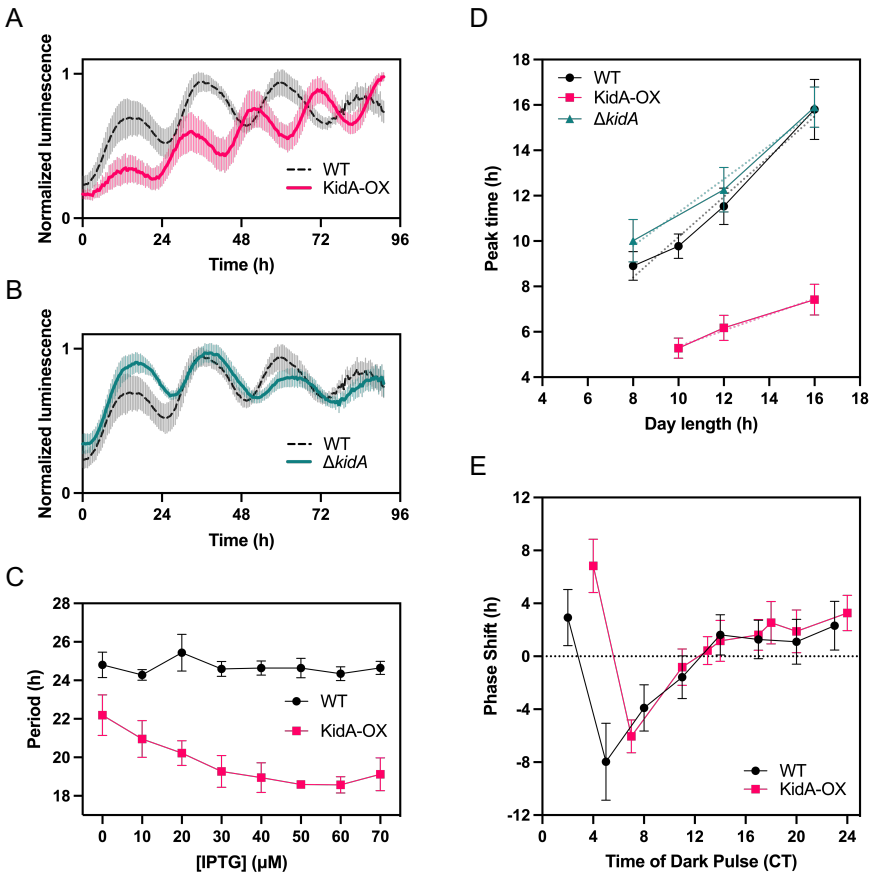

Figure 2.3: KidA overexpression (KidA-OX) mutants exhibit shorter in vivo clock rhythms and altered entrainment. (A and B) Bioluminescence (PpsbAI::luxAB, PpsbAI::luxCDE) time traces of WT, KidA-OX, and Δ*kidA* cultures induced with 10 µM IPTG. (A) WT vs. KidA-OX (B) WT vs. Δ*kidA*. Each trace was normalized by dividing by the maximum value. The solid and dotted lines show the mean normalized signal and the spread shows the SD. Average period obtained from fitting: WT = 23.5 ± 0.2 h, n = 8; KidA-OX = 20.1 ± 0.1 h, n = 7; Δ*kidA* = 25.3 ± 0.4 h, n = 8. Traces are aligned so that t = 0 occurs at a trough after three cycles in constant light. (C) The mean best-fit periods of the KidA-OX strain induced using different concentrations of IPTG and the WT strain characterized in the same conditions. Average period obtained from fitting at 50 µM IPTG: WT = 24.6 ± 0.6 h; KidA-OX = 18.6 ± 0.1 h. Error bars show the SD (n = 3–4). (D) Clock phases of WT, KidA-OX, and Δ*kidA* induced with 10 µM IPTG after entrainment to different photoperiods (10L:14D, 12L:12D, 16L:8D). The average time of the first peak of the bioluminescence signal after dawn following four LD cycles is plotted. Error bars show SD (n = 11–23 for each sample). Dotted lines show linear regression to the data: $m_{WT} = 0.89$ ($CI_{95\%} = [0.47, 1.31]$, $R^2 = 0.98$), $m_{KidA-OX} = 0.35$ ($CI_{95\%} = [-0.08, 0.78]$, $R^2 = 0.99$), $m_{\Delta kidA} = 0.74$ ($CI_{95\%} = [-0.54, 2.01]$, $R^2 = 0.98$). (E) Phase response curves of WT and KidA-OX induced with 10 µM IPTG. Entrained cultures were allowed to free-run in constant light and then were subjected to a 5 h dark pulse at various times. The mean difference between the first peak of the reporter after the dark pulse and the closest peak time in the control (phase shift) is plotted. Error bars show the SD (n = 3–20 for each sample). CT, circadian time.

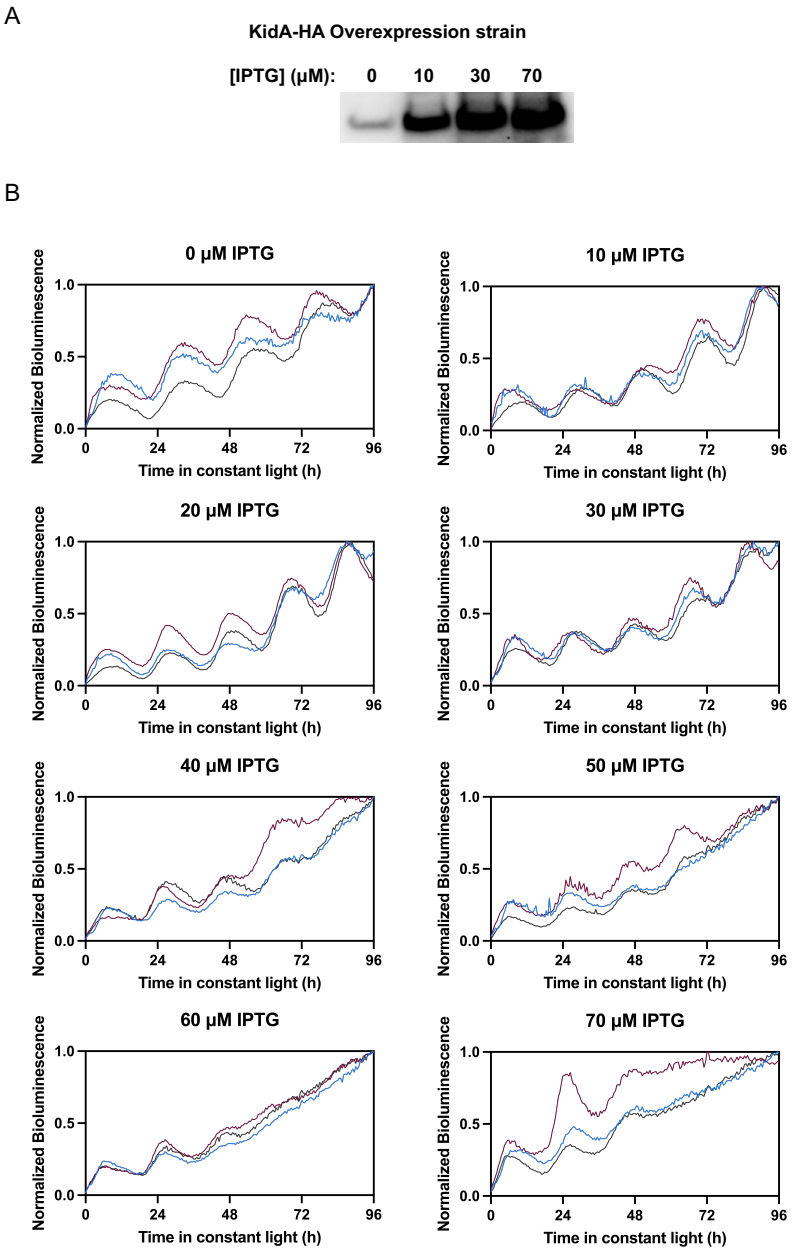

Figure 2.4: KidA overexpression strain has IPTG-dependent expression level of KidA protein, and high levels of IPTG induction cause arrhythmicity. (A) KidA protein expression levels of KidA overexpression strain induced without IPTG (leaky expression) or with varying concentrations of IPTG analyzed by Anti-HA Western blot. (B) Normalized bioluminescence traces of KidA-OX reporter strain induced with 0 to 70 μM IPTG.

A possible explanation for this effect could be that the KidA-OX strain is hypersensitive to dark pulses, and the phase is reset every night. We thus investigated whether the KidA-OX strain had an altered phase response curve for 5 h dark pulses, a condition that can produce strong resetting from out-of-phase dark pulses in WT cells [18]. We were additionally motivated to test this possibility because a known interactor of fsKaiB, CikA, is implicated in the dark pulse-induced resetting of the clock [43]. However, after correcting for the shortened period, the KidA-OX strain did not have a noticeable difference from the WT both in terms of the maximum phase advance and maximum phase delay, suggesting that the photoperiodic entrainment phenotype is not caused simply by increased sensitivity to a short dark pulse (Fig. 2.3E).

2.4.4 The N-Terminal Region of KidA Is Composed of Multiple PAS Domains, Which Are Responsible for the Period-Shortening Effect of KidA.

To understand the biochemical basis of the period-shortening phenotype of the KidA-OX strain, we first used structural prediction to further dissect KidA's domain architecture beyond the GGDEF and EAL domains predicted by BLAST in the C-terminal region. We used the Phyre2 algorithm to generate local three-dimensional folding predictions for the N-terminal region of the protein. Four tandem local structures that matched the canonical Per-Arnt-Sim (PAS) domain topology were predicted to form in the N-terminal region [45] (Fig. 2.5B). Based on these results, we propose that the full-length KidA protein architecture is composed of four PAS- like domains followed by a GGDEF domain and an EAL domain (Fig. 2.5A). We denote these predicted domains PAS-A, -B, -C, and -D, respectively.

Many PAS domains are known to bind to small-molecule ligands. We attempted to predict ligand-binding sites by aligning the KidA domain sequences with consensus sequences for PAS domain families whose structure and ligand-binding sites have been well charac-

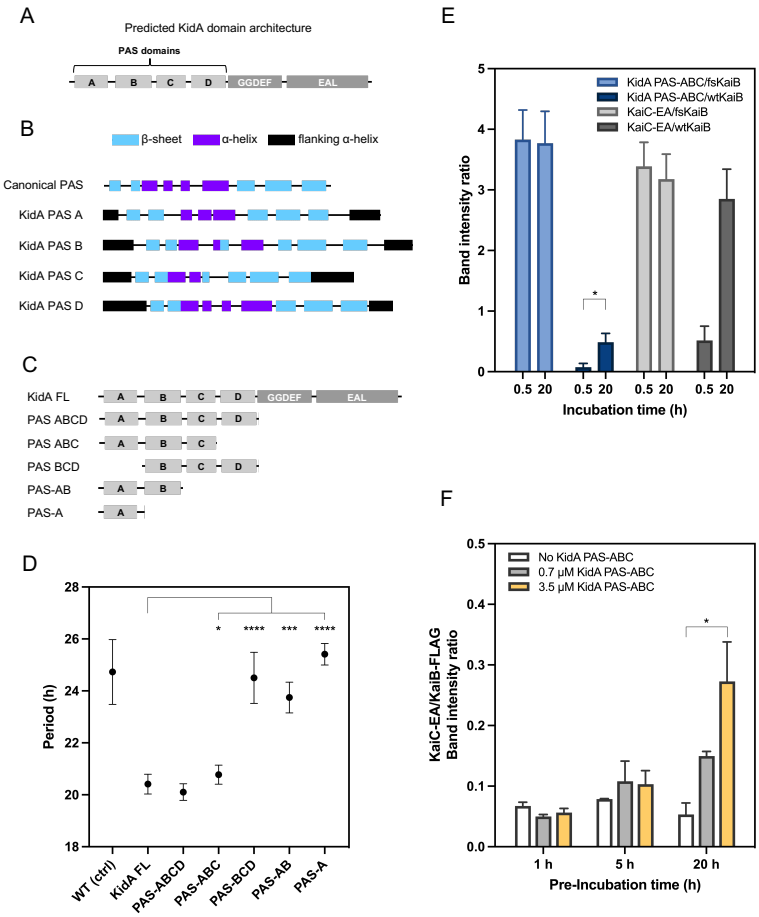

Figure 2.5: An N-terminal fragment of KidA is sufficient for the clock phenotype and binds to fold-switched KaiB. (A) Proposed KidA domain architecture derived from BLAST alignment and secondary structure prediction. (B) Phyre2 secondary structure prediction suggests four tandem domains with PAS-like folds. Canonical PAS architecture was modified from Möglich et al. (23). In the schematic, the first flanking alpha helix is the same as the last flanking alpha helix of the previous PAS domain. Predicted domain boundaries between the first and last β-sheets: PAS-A (22–114); PAS-B (145– 246); PAS-C (270–350); PAS-D (373–472). (C) Domain truncation mutants of KidA expressed *in vivo*. (D) Free-running clock periods of *S. elongatus* strains expressing KidA fragments described in (C). The average periods are plotted, and error bars show the SD (n = 4–16). The PAS-A construct expressed poorly compared with the other constructs. (E) *In vitro* co-IP of KidA PAS-ABC fragment (3.5 μM) using fsKaiB-FLAG or wtKaiB-FLAG (3.5 μM) as bait in a 30-min or 20-h coincubation; KaiC S431E;T432A (KaiC-EA) served as a positive control for KaiB interaction. Band intensities were determined by densitometry after background subtraction. Mean band intensity ratios are plotted, error bars show the SD (n = 3 for each condition). (F) *In vitro* co-IP of KaiC-EA using wtKaiB-FLAG (3.5 μM) as bait after preincubating wildtype KaiB-FLAG with varying amounts (0, 0.7, or 3.5 μM) of KidA PAS-ABC for varying lengths of time (1, 5, or 20 h). KaiC-EA was added 5 min prior to IP. Band intensities were determined by densitometry after background subtraction. Mean band intensity ratios are plotted, error bars show the SD (n = 2–3 for each condition). (D–F) All significance analyses were performed using Welch's t test. * = $P < 0.05$, ** = $P < 0.01$, *** = $P < 0.001$, **** = $P < 0.0001$.

terized [46]. This approach did not yield positive results for PAS-A, PAS-B, or PAS-C. However, the PAS-D sequence contains some of the conserved residues present in both the light-oxygen-voltage-sensing (LOV) domain's flavin mononucleotide (FMN)-binding region and the MmoS/NifL domain's flavin adenine dinucleotide (FAD)-binding region; this suggests that KidA PAS-D may interact with a flavin cofactor, though it lacks the cysteine involved in canonical LOV domain photochemistry (Fig. 2.6).

We next sought to identify a fragment necessary and sufficient for the period-shortening effect of KidA-OX. We created a series of domain truncation mutants of KidA and characterized the circadian rhythms of strains overexpressing these fragments. This analysis revealed that the first three PAS domains (KidA PAS-ABC) are sufficient to phenocopy full-length KidA's period-shortening effect. Constructs that lack either PAS-A or PAS-C did not shorten the period (Fig. 2.5D). Thus, we conclude that the GGDEF and EAL domains are not involved in the period phenotype, PAS-D is dispensable, and KidA engages the oscillator through the three N-terminal PAS domains.

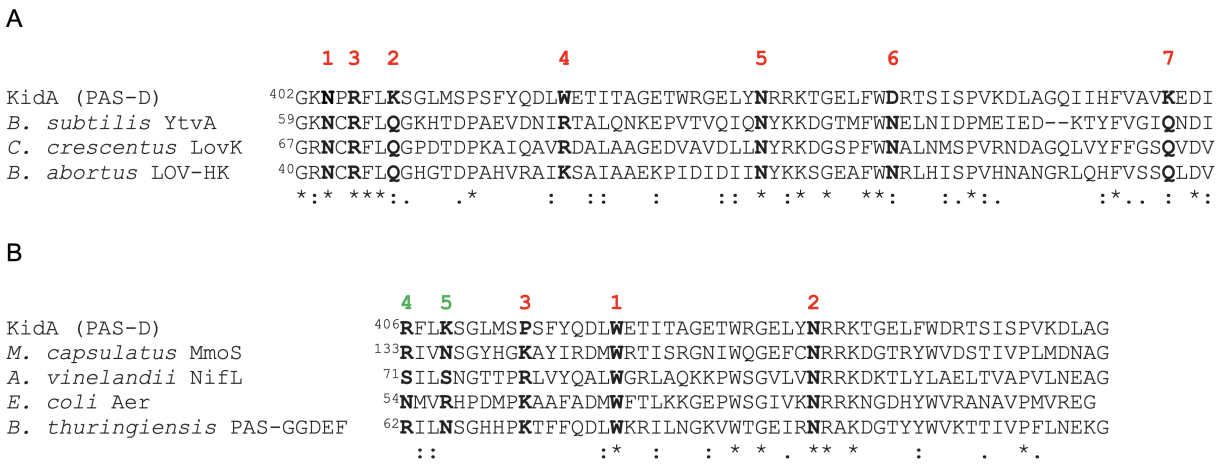

Figure 2.6: PAS-D alignment to LOV and MmoS/NifL domain sequences. Multiple sequence alignment of KidA protein sequence and the flavin-binding region of (A) the LOV domain sequences and (B) the MmoS and NifL domain sequences. Alignments were created using Clustal Omega [39] and annotated using the same scheme in Figure 6 and Figure 7 in a review by Henry and Crosson [46]. The numbered sites are highly conserved sites that coordinate the flavin mononucleotide (FMN) and the flavin adenine dinucleotide (FAD) ligands that are noted in [46] where the structures of the active sites are described in detail.

2.4.5 KidA Directly Binds Fold-Switched KaiB through PAS Domains In Vitro.

Because we initially identified KidA via pulldown with KaiB, we investigated whether the two purified proteins directly interact by using an *in vitro* co-IP approach. We used the KidA fragment spanning the first three PAS domains (KidA PAS-ABC) shown to be sufficient for the *in vivo* period-shortening effect (Fig. 2.5C and D). Coincubation of KidA PAS-ABC with wildtype KaiB (wtKaiB-FLAG) resulted in direct binding but with slow kinetics, reaching half-maximal binding after ∼12 h (Fig. 2.5E and Fig. 2.7). This behavior is similar to the kinetics observed for the binding of KaiC with KaiB, which is slow partially because of the fold-switching of KaiB (Fig. 2.5E) [11]. We thus hypothesized that KidA PAS-ABC might bind selectively to fold-switched KaiB. To test this, we performed the same co-IP experiment using a mutant KaiB that is locked in the fold-switched form (fsKaiB-FLAG) to pull down KidA PAS-ABC [47]. Much more KidA PAS-ABC was pulled down with fsKaiB-FLAG than with wtKaiB-FLAG, and protein complexes had fully formed after only a 30 min incubation (Fig. 2.5E). A KaiC phosphomimetic for the nighttime state (KaiC-EA) also rapidly formed complexes with fsKaiB, serving as a control for a known fsKaiB interactor (Fig. 2.5E). Thus, the KidA PAS-ABC region directly interacts with fold-switched KaiB. We interpret the slow kinetics of KidA PAS-ABC binding to wtKaiB as reflecting the slow conversion of the KaiB ground- state fold to the fold-switched form [11], which is then stabilized in complex with KidA. Consistent with this interpretation, KaiB that is preincubated with KidA PAS-ABC becomes competent to bind rapidly to KaiC-EA, and the amount of rapid binding increases with the preincubation time and the amount of KidA PAS-ABC (Fig. 2.5G). Furthermore, KidA PAS-ABC does not inhibit the assembly of KaiABC complexes when all Kai proteins are present (Fig. 2.8).

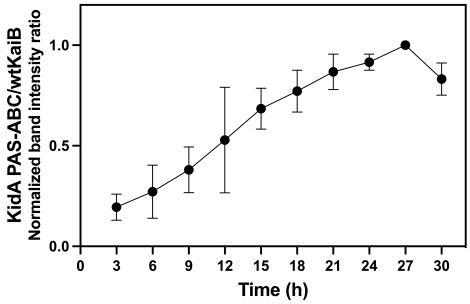

Figure 2.7: Kinetics of KidA PAS-ABC binding to KaiB. *In vitro* co-IP of KidA PAS-ABC using wtKaiB-FLAG as bait after co-incubation in 30 °C for different lengths of time. 3.5 µM KidA PAS-ABC and 3.5 µM KaiB-FLAG were used. Band intensities were determined by densitometry after background subtraction. Mean normalized band intensity ratios are plotted. Error bars show the standard deviation (N=3 for each timepoint).

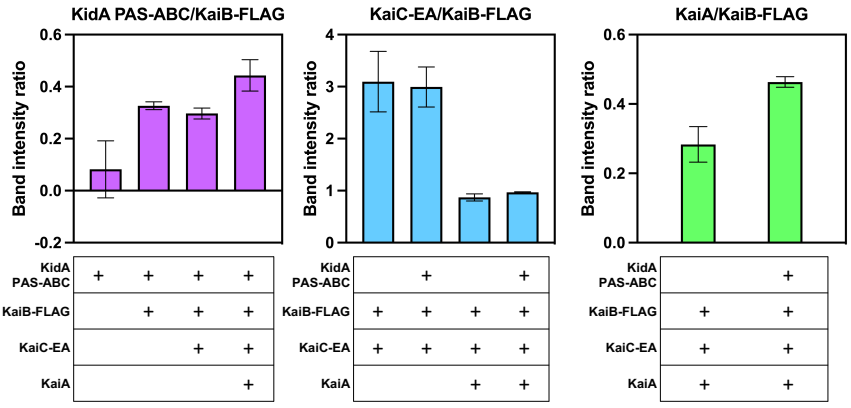

Figure 2.8: No obvious inhibition of Kai complex assembly caused by KidA PAS-ABC. *In vitro* co-IP of KaiB binding partners KidA PAS-ABC, KaiC-EA, and KaiA after 20 h co-incubation of different combinations. Band intensities were determined by densitometry after background subtraction. Mean band intensity ratios are plotted. Error bars show the standard deviation (N=3 for each condition).

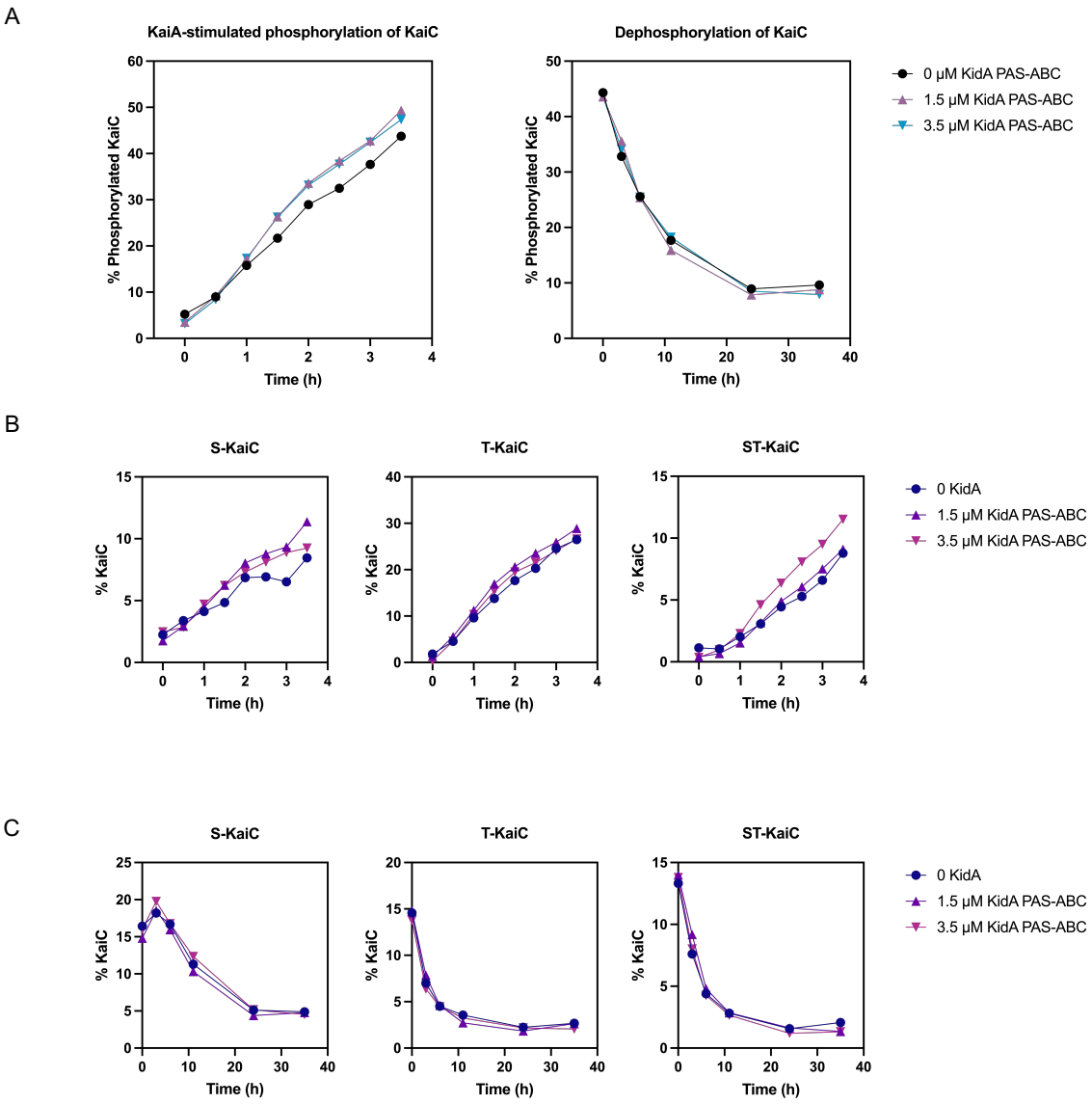

Figure 2.9: KidA PAS-ABC does not noticeably affect KaiA-stimulated phosphorylation and dephosphorylation of KaiC *in vitro*. (A) Left: The fraction of phosphorylated KaiC in KaiA-stimulated KaiC phosphorylation reactions containing 0, 1.5 μM, or 3.5 μM KidA PAS-ABC and 0.4 μM KaiA, starting from dephosphorylated KaiC at t = 0. Right: The fraction of phosphorylated KaiC in reactions containing 0, 1.5 μM, and 3.5 μM KidA PAS-ABC, starting from KaiC thawed from -80 °C storage at t = 0. (B) Fraction of each phosphoform in the KaiA-stimulated KaiC phosphorylation reactions containing 0, 1.5 μM, or 3.5 μM KidA PAS-ABC, analyzed by SDS-PAGE. (C) Fraction of each phosphoform in the KaiC dephosphorylation reactions, analyzed by SDS-PAGE.

2.4.6 Reconstitution of the Period-Shortening Effect of KidA In Vitro.

To investigate the mechanism of KidA's period-shortening effect, we first asked whether the phenotype results from KidA's direct interaction with the Kai proteins themselves rather than other factors *in vivo*. We added KidA PAS-ABC to the *in vitro* reconstituted Kai oscillator system composed of purified KaiA, KaiB, and KaiC, and monitored oscillations using a fluorescence polarization (FP) label on KaiB. The addition of KidA PAS-ABC shortened the period of the KaiABC oscillator (Fig. 2.10A), and the magnitude of period shortening was dependent on the concentration of KidA PAS-ABC (Fig. 2.10D, Left, black) in a manner quantitatively similar to the *in vivo* trend (Fig. 2.3A). Additionally, the amplitude of the FP rhythms decreased with increasing KidA PAS-ABC (Fig. 2.10D, Right, black).

The enzymatic rates of KaiC are important for setting the pace of phosphorylation and dephosphorylation, and thus contribute to the overall period of oscillation [48, 49]. However, we could not detect any influence of KidA on phosphorylation or dephosphorylation kinetics in partial reactions that lacked KaiB (Fig. 2.9). Thus, we turned to a mathematical model to ask whether binding interactions with KaiB alone are sufficient to change the oscillator period and amplitude.

2.4.7 KidA Binding to KaiB in the Fold-Switched Form Shortens the Period in a Mathematical Model.

Our data suggest a model in which KidA acts by binding and stabilizing the fsKaiB fold. To test whether this mechanism can account for our observations, we modified an existing mathematical model of the Kai oscillator to include a KidA-KaiB binding equilibrium. Specifically, we built on a model published by Paijmans et al. that accurately describes the phosphorylation dynamics and their dependence on the adenosine triphosphate:adenosine diphosphate ratio ([ATP]/[ADP]) [50]. The original model assumes an inexhaustible pool of KaiB that binds slowly to KaiC. Since we hypothesized that KidA shortens the period by

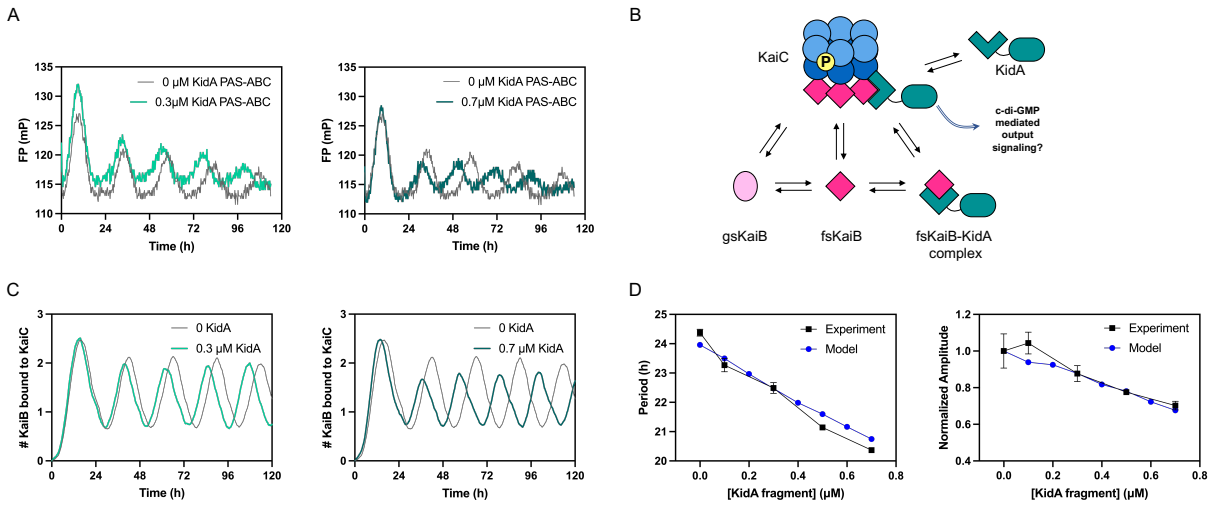

Figure 2.10: (A) *In vitro* reconstitution of the period-shortening effect of KidA. The KidA PAS-ABC fragment was added to a standard mixture of KaiA, KaiB, and KaiC. Oscillations were measured by fluorescence polarization of labeled KaiB (averaged traces shown from duplicate experiments). (B) Cartoon overview of a mathematical model based on the hypothesis that KidA stabilizes the fold-switched form of KaiB by direct binding. The Paijmans model was modified to explicitly describe the interconversion between the ground-state and fold-switched state of KaiB.The protein complexes and reaction arrows shown were added to allow KidA to bind fsKaiB (Supplementary Materials and Methods). (C) Time course of oscil- lations of KaiC-bound KaiB molecules per hexamer in the mathematical model. Model parameters were chosen to have period-dependence close to the experimental value. (D) Plots of the period and amplitude of the fluorescence polarization rhythm (as shown in Fig. 4A) as a function of [KidA] and the predictions from the model with the same parameter set (as shown in Fig. 4C). (Left) Period and (Right) amplitude normalized by dividing by the amplitude value at 0 μM KidA. Mean values are plotted, and the error bars show the SD (Experimental n = 2, Model n = 20).

increasing the concentration of free fold-switched KaiB, we modified the model to track an explicit pool of KaiB monomers that can slowly interconvert between ground-state and fold-switched forms. The fold-switched molecules can bind rapidly to KaiC. KidA is introduced to the model as a species that binds specifically to fsKaiB. The model contains 10 additional parameters beyond the original model (Table 2.4).

To characterize the KidA-dependent clock properties of the model, we used Markov chain Monte Carlo to explore parameters that supported circadian oscillations both with and

without KidA present. The majority of sampled parameter sets (77%) showed shortening of the period with the addition of KidA, though the median slope of period vs. KidA concentration was less negative than that observed experimentally (–0.74 h/µM vs. –5.6 h/µM, (Fig. 2.11A). Most parameter sets (76%) also showed reduced amplitude of the KaiB•KaiC complex rhythm with increasing KidA (Fig. 2.11B). In these analyses, only parameter sets that have close to a 24 h period without KidA were considered (Fig. 2.11C). The predominance of parameter sets leading to period shortening and reduced amplitude without having selected for these features suggests that the qualitative effects on period and amplitude are generic features of mechanisms in which a binding partner, such as KidA, stabilizes the fold-switched KaiB state.

Analysis of the relationship between the parameters describing KidA and quantitative changes in period and amplitude revealed a notable trend (Fig. 2.12A). The magnitude of the period and amplitude slopes are anticorrelated with both the dissociation constant (K_d) of the KidA-fsKaiB binding reaction and the off-rate ($kKidA_{off}$); tighter binding KidA exerts a stronger period-shortening effect (Fig. 2.12A–C). To ensure that our results were not idiosyncratic to the small number of parameter sets in the tails of the distributions in Fig. 2.11A–C, we harvested many additional parameter sets with period and amplitude slopes consistent with the experimentally observed dependence of the period on KidA concentration by including a restraint on the period slope during fitting (Fig. 2.11D–F). These parameter sets show similar correlations.

To understand this trend, we selected a parameter set that gave period and amplitude slopes close to the experimental values to study in detail (shown in Fig. 2.10C and D). We found that KidA primarily affects rebinding of KaiB to KaiC after dissociation of a KaiB•KaiC complex (Fig. 2.13A). Binding of KidA to fsKaiB increases the lifetime of fsKaiB•KidA complexes and in turn the likelihood that these complexes rebind to the N-terminal (CI) domain of KaiC before KaiB reverts to its ground-state fold. In this way, KidA

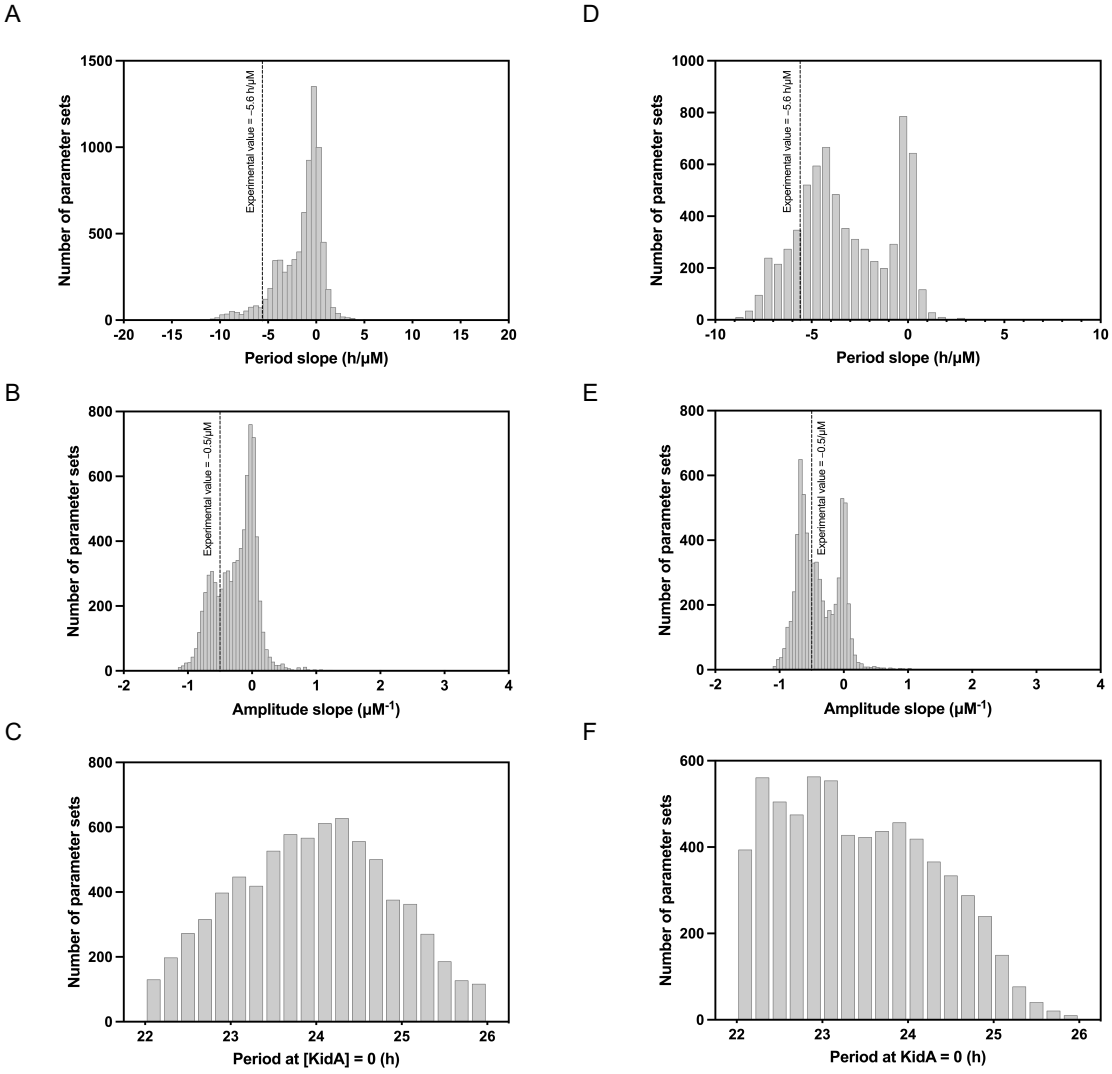

Figure 2.11: Dependence of the period and the amplitude on KidA concentration for sampled parameter sets. (A, D) Histogram of model slope of the period as a function of [KidA] using log likelihoods (A) L_1 and (D) L_2. The experimental slope is –5.6 h/μM. (B, E) Histogram of model slope of the normalized amplitude as a function of [KidA] using log likelihoods (B) L_1 and (E) L_2. The experimental slope is –0.5 /μM. (C, F) Histogram of model period without KidA present using log likelihoods (C) L_1 and (F) L_2.

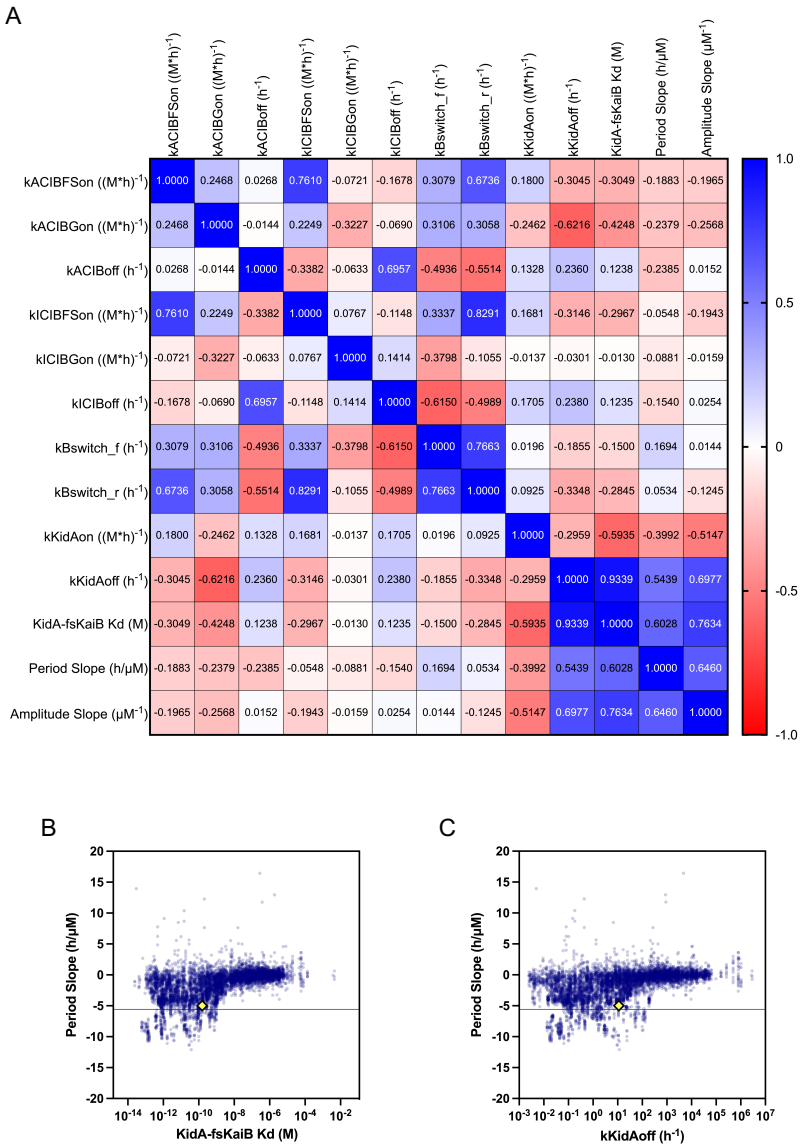

Figure 2.12: Correlation of model parameters with the slopes of the period and amplitude. (A) Spearman's correlation coefficient between pairs of parameters and the period and amplitude slopes. (B) KidA-fsKaiB dissociation constant (KidA-fsKaiB K_d) and the slope of the period as a function of [KidA] for all sampled parameter sets. (C) KidA-fsKaiB off-rate ($kKidA_off$) and the slope of the period as a function of [KidA] for all sampled parameter sets. Results shown are obtained with log likelihood L_1. (B-C) The parameter set used for Figures 2.10 C-D is marked with a yellow diamond. The horizontal line shows the experimental period slope value.

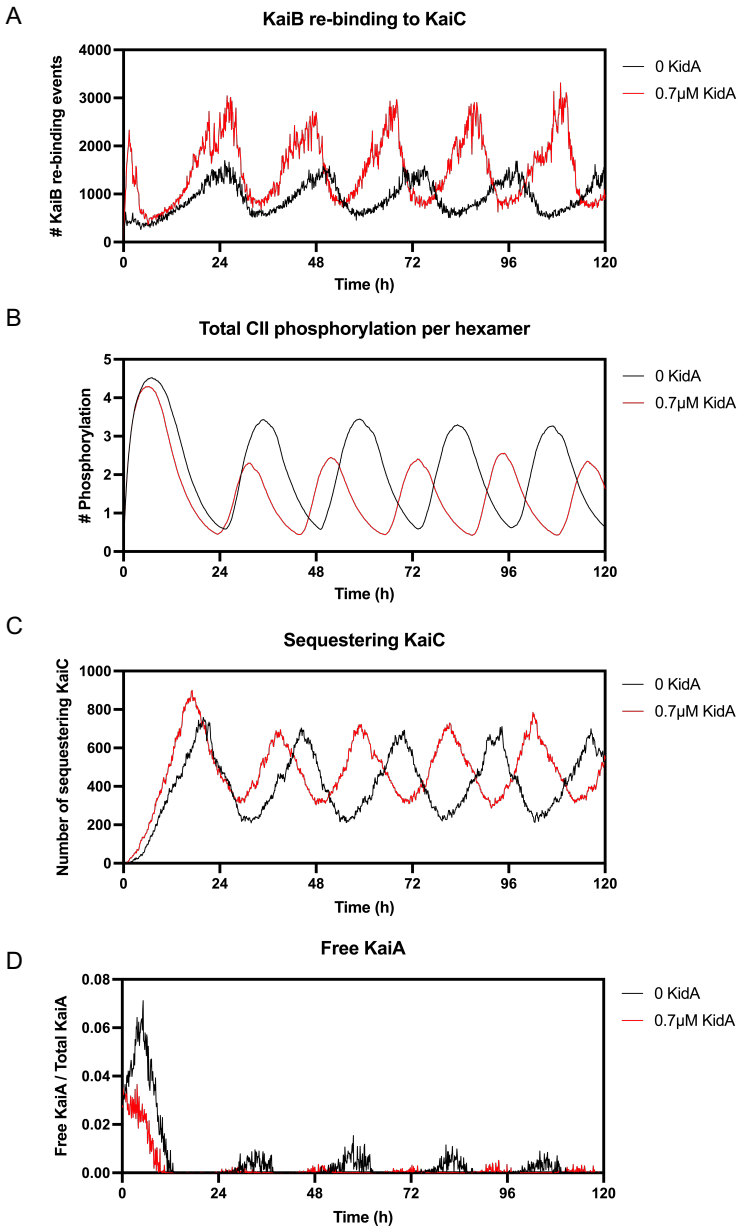

Figure 2.13: KidA promotes KaiB re-binding to KaiC, which alters the dynamics of phosphorylation in the model. (A) The number of fsKaiB re-binding events for various concentrations of KidA. Binding events in which fsKaiB molecules that have previously unbound from the CI domain but have not reverted to gsKaiB bind to CI are counted every 0.1 hours. (B) Phosphorylation per hexamer in the full oscillator reaction for indicated concentrations of KidA. Curves shown are the average numbers of subunits per KaiC hexamer that have at least one of S431 or T432 phosphorylated. (C) The copy numbers of sequestering KaiC for various concentrations of KidA. Sequestering KaiC hexamers are KaiC hexamers with the maximal amount (6) of KaiB bound to the CI domain. (D) The fraction of KaiA that is free in solution for various concentrations of KidA. Simulation parameters are the same as in Figures 2.10 C-D (Table 2.4).

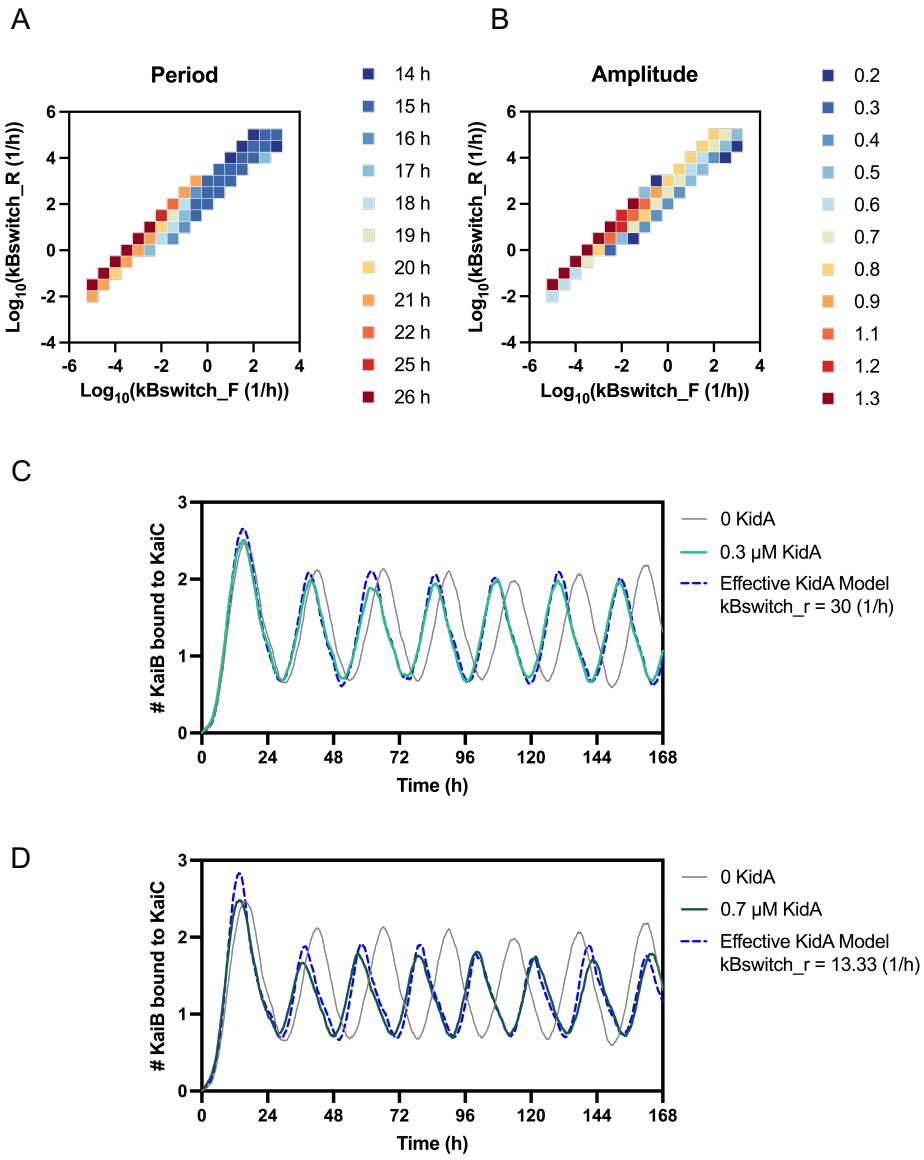

Figure 2.14: Shifting the equilibrium between the ground state and fold switched forms of KaiB alters the period and amplitude. (A-B) Period and amplitude of the oscillator as a function of KaiB fold switching rates in the effective KidA model (KidA is not explicitly present). Combinations of the fold switching rate that failed to produce oscillations were not plotted. That similar periods and amplitudes are obtained along the diagonal suggests that the ratio of the parameters on the axes (i.e., the equilibrium constant) is constrained but their absolute values are not. (C-D) For comparison, two representative time courses of KaiC-bound KaiB in the effective KidA model with kBswitch_r decreased from 43 h^{-1} to 30 h^{-1} (C) and with kBswitch_r decreased from 43 h^{-1} to 13.3 h^{-1} (D) are shown together with time courses of KaiC-bound KaiB from the full model with 0.3 µM KidA and 0.7 µM KidA, respectively.

increases the population of hexamers with a complete set of six KaiB monomers bound, which are the hexamers capable of sequestering KaiA on CI in the model (Fig. 2.13C). Increased KaiA sequestration (Fig. 2.13D) results in faster depletion of the KaiA pool available for catalyzing nucleotide exchange in the C-terminal (CII) domain and earlier dephosphorylation of KaiC hexamers, thus resulting in a shorter period. Moreover, the lower amount of free KaiA reduces the number of hexamers that enter the phosphorylation cycle and consequently the amplitude (Fig. 2.13B). Consistent with this picture, the effect of KidA on the oscillator can be largely recapitulated by an effective model that approximates the role of KidA by adjusting the equilibrium constant between the ground-state and fold-switched forms of KaiB (Fig. 2.14).

2.5 Materials and methods

2.5.1 fsKaiB-HA co-IP/MS.

The *S. elongatus* PCC 7942 strain expressing HA-tagged fsKaiB (KaiBG88A;D90R) from an inducible promoter (MRC1109) was grown in BG-11M media ([51]) with shaking at 175 rpm in a Percival incubator with constant light (intensity of approximately ∼100 µmol photons $m^{-2}s^{-1}$ using cool white fluorescent bulbs), where each 250 mL flask contained 100 mL culture volume. When a high density (OD750 =1) was achieved, the culture was subjected to a 12:12 LD cycle. After the first 12 h dark pulse, expression was induced with 500 µM IPTG. After 12 h in light following the IPTG induction, the light sample (L) was harvested. After 12 h in dark following the light sample harvest, the dark sample (D) was harvested. A negative control sample was obtained by collecting WT cells under identical conditions in L and D and pooling them. The cell pellets were lysed and subjected to anti-HA co-IP using magnetic beads (see Anti-HA Co-IP from Cyanobacterial Lysate in Supplementary Materials and Methods). The resulting eluate samples (fsKaiB L, fsKaiB D, and WT L+D) were analyzed at the Harvard Center for Mass Spectrometry (Cambridge, MA) (see LC-MS/MS Analysis of fsKaiB Co-IP Samples in Supplementary Materials and Methods).

2.5.2 Monitoring In Vivo Clock Rhythms Using Bioluminescence Reporters.

Bioluminescence reporter strains expressed both luxAB luciferase genes derived from *Vibrio harveyi* under a rhythmic promoter (PpsbAI) and *luxCDE* genes allowing endogenous production of substrate. The sample preparation and data collection were performed as previously described [36] with slight modifications (see *In vivo* Clock Rhythm Measurement in Supplementary Materials and Methods). All experiments in Fig. 2.3 were performed with 10 µM IPTG unless otherwise noted, and the periods and peak times were estimated by fitting the data to the equation Y = Offset+Slope*X+Amplitude*sin((2*pi*((X-PhaseShift)/

Period))) (see Circadian Rhythm Data Fitting in Supplementary Materials and Methods for details). One 12L:12D cycle was used to entrain cells in the experiments shown in Fig. 2.3 A–C before release to constant light. Cells used in the photoperiod experiment (Fig. 2.3D) were subjected to four cycles of entrainment with the given photoperiod (8L:16D, 10L:14D, 12L:12D, or 16L:8D) followed by constant light. For the phase response experiment (Fig. 2.3E), cells were entrained by two 12L:12D cycles and were released to constant light, during which a 5 h dark pulse was given at the specified time. The earliest dark pulse start time was 48 h after the entrainment cycles. The dark pulse start time for each condition was converted into circadian time by multiplying the time by (24/average fitted period).

2.5.3 Protein Expression and Purification.

KaiA, KaiB, KaiB-FLAG, KaiC, and KaiC-EA proteins were purified as described previously [52, 53]. The fsKaiB-FLAG protein (KaiB-1–99-Y7A-I87A-Y93A-FLAG) was a gift from Andy LiWang [47]. For KidA PAS-ABC purification, the KidA coding sequence for residues 1–359, preceded by the (PreScission Protease) PSP cleavage site (LFQ/GP) sequence and followed by the HA tag sequence, was cloned into the pRSET-B vector. The expression plasmid was used to transform BL-21 (DE 3) Escherichia coli cells. We used 5 mL overnight culture to grow 1 L culture in LB to optical density (OD600) between 0.5 and 0.6 by shaking at 37 ℃. Then 0.3 mM IPTG was added for 3 h induced expression at 30 ℃. The cells were pelleted by centrifugation for 10 min at 5,000 g, 4 ℃, snap-frozen in liquid nitrogen, and stored in –80 ℃. For purification, the cell pellets were lysed using an Emulsiflex-C3 homogenizer (Avestin) and centrifugated for 30 min at 30,000 g, 4 ℃. The supernatant containing the soluble protein was syringe-filtered using a 0.45 µm filter and was Ni-affinity purified by HisTrap HP column (GE) followed by cleavage by HRV3C protease (Pierce, Thermo Scientific). Next, the protein sample was subjected to anion exchange chromatography using a HiTrap Q column (GE) and eluted with a gradient from 20 mM Tris

pH 8,90 mM NaCl buffer to 20 mM Tris pH 8,1 M NaCl. The protein eluted in two separate peaks in the chromatograph during anion exchange. The composition of each fraction was analyzed by SDS-PAGE. Each peak contained a doublet with approximately the expected molecular weight for KidA PAS-ABC. The fractions corresponding to each peak were pooled separately; the late-eluting peak was used for all experiments in this study. The material was then buffer- exchanged into Kai reaction buffer (10% glycerol, 20 mM Tris-HCl pH 8, 150 mM NaCl, 5 mM $MgCl_2$, 0.5 mM EDTA pH 8, 1 mM ATP pH 8). The concentration was measured by Bradford assay.

2.5.4 In Vitro Co-IP and Fluorescence Polarization.

Purified proteins of interest were coincubated with KaiB-FLAG or fsKaiB-FLAG in 30 ℃. After the incubation, the reactions were snap-frozen in liquid nitrogen and kept in –80 ℃. The frozen reactions were thawed on ice and were promptly subjected to co-IP using anti-FLAG antibody-conjugated magnetic beads (Sigma-Aldrich, #M8823). The eluates from the co-IP were run in SDS-PAGE gel. The gel was stained using Sypro Ruby (Invitrogen), which was then imaged by ChemiDoc (Bio-Rad). The band intensity was used as a metric of the quantity of each protein that was pulled down by the anti-FLAG beads (see *In vitro* Co-IP Using FLAG-Tagged Proteins as Bait in Supplementary Materials and Methods for details). Fluorescence polarization measurements were performed by adding fluorescein-labeled KaiB to the purified KaiABC reaction as previously described [36, 54, 55] (see Fluorescence Polarization in Supplementary Materials and Methods for details).

2.5.5 Mathematical Modeling.

We expanded the model of Paijmans et al. [50] to include the proposed KaiB and KidA dynamics. In brief, KaiB is treated as a monomer and allowed to convert between its ground-state and fold-switched forms. KidA binds and unbinds KaiB only when it is in the

fold-switched form; KidA does not interfere with KaiB-CI or KaiB-KaiA binding. Detailed balance is enforced for all of the reactions added to the model. The model accounts for individual KaiC hexamers and their complexes, and its dynamics are simulated with the kinetic Monte Carlo procedure in [50]. The parameters of the original model were set at their values in Paijmans et al. [50]; parameters for the added reactions were manually set to reprise the KaiB populations in the original model and then sampled with a Markov chain Monte Carlo procedure similar to that in [56]. Further model details are given in the Supplementary Materials and Methods.

2.6 Discussion

In this study, we identified a previously unstudied protein that interacts with the Kai circadian oscillator using a co-IP/MS approach. KaiB, an essential component of the oscillator, is a metamorphic protein, and multiple interactions in the clock are gated by its transition between alternate folds. By using a mutant form of KaiB that is locked into its fold-switched state as bait, we attempted to stabilize complexes that might other- wise be difficult to detect. The top hit, which we named KidA, is predicted to contain multiple PAS-like domains and both GGDEF and EAL domains, involved in c-di-GMP synthesis and hydrolysis, respectively. Deletion or mild overexpression of KidA changes the free-running period of the clock; more severe overexpression causes arrhythmia. A fragment consisting of the first three PAS domains of KidA directly interacts with fold- switched KaiB and shortens the period of the KaiABC oscillator.

While mutations of KaiC are known to markedly change the period of the in vitro oscillator, typically causing a concomitant change in the KaiC ATPase cycle [57], most other manipulations, such as changing Kai protein or nucleotide concentrations produce only slight changes in the period [37]. Here, we find that large period changes can also be caused by introducing a specific binder for the fold-switched state of KaiB, suggesting that regulating

access to this fold plays an important role in timing.

KidA-OX in cells leads to an entrainment defect in which the clock does not appropriately set its phase relative to the photoperiod. It does not, however, show increased phase shifts in response to a brief pulse of darkness. This suggests that the regulation of KidA activity may be more complex in a LD cycle. The physiological functions of KidA are incompletely understood. One possibility is that KidA's role is to act as a sensor for the fold-switched form of KaiB that appears in the subjective night. Information about the clock state might then be relayed to downstream processes, perhaps through diguanylate cyclase activity. Cyclic-di-GMP is a small molecule known to be involved in a variety of cellular processes in prokaryotic organisms, including regulation of biofilm formation and lifestyle transitions [58]. Considering that many cyanobacteria engage in biofilm formation, the potential for KidA's role in biofilm, and, by extension, clock regulation of biofilms is especially interesting [59].

Alternatively, a physiological role of KidA could be to adjust the period or entrainment properties of the oscillator, as occurs with mild overexpression. In this scenario, the activity of full-length KidA may be low under standard culture conditions, but with the potential for unknown signals to stimulate KidA to interact strongly with the oscillator. PAS domains can sense signals by binding a variety of small-molecule ligands as well as through protein-protein interactions [46]. The presence of multiple PAS domains suggests the possibility that KidA could receive and integrate other signals besides the clock state [60], particularly since PAS-D, which is predicted by sequence to bind a flavin cofactor, is not required for the clock period phenotype. Notably, the kidA gene is adjacent to a heme oxygenase gene (Synpcc7942_1858), which suggests the possibility that KidA could bind heme, biliverdin (the product of the heme oxygenase reaction), or similar molecules.

Bacterial PAS domains frequently appear in tandem and are typically followed by enzymatic domains such as histidine kinase or diguanylate cyclase domains. The PAS domain

was first described in eukaryotic proteins that associate with clock proteins (the P in PAS domain stands for the *Drosophila* clock protein PERIOD), and PAS domain-mediated clock protein interactions have been found throughout eukaryotes [61]. Involvement of PAS domains in prokaryotic rhythms is only just becoming apparent [62]. The identification of KidA provides a clear example of how a bacterial protein containing PAS domains can interact with a circadian oscillator.

There are numerous examples of PAS domain-containing genes appearing co-operonic with or adjacent to *kai* gene homologs in bacterial genomes outside of cyanobacteria that have *kaiBC* genes but no *kaiA* [63]. This pattern of genomic organization suggests that the association of PAS domain-containing bacterial proteins with Kai proteins via PAS domains could be a generally conserved mechanism widespread in kai homologs. Further study of KidA promises to advance our understanding of how the core Kai oscillator might be linked to other cellular processes. Because it contains multiple PAS domains and enzymatic domains that can participate in c-di-GMP signaling, KidA may act as a bridge between environmental inputs, clock state, and second messenger signaling.

2.7 Supporting information

2.7.1 Supplementary Materials and Methods

Cyanobacterial strain construction

For overexpression strains, the gene of interest was integrated into the Neutral Site 1 (NS1) of the *S. elongatus* genome. The coding sequence of the gene of interest + C-terminal HA tag (TACCCATACGATGTTCCAGATTACGCT) was inserted into pAM2991 plasmid downstream of the IPTG-inducible pTrc promoter and upstream of the spectinomycin resistance gene cassette, which are flanked by the NS1 sequences [64]. Strains constructed this way include the KaiBG88A;D90R-HA (fsKaiB-HA) strain used in the co-IP/MS experiment,

KidA-OX, and KidA domain truncation mutant overexpression strains. Wild type *S. elongatus* was used as the background for fsKaiB-HA. WT/pAM2195 reporter strain (MRC1005), which carries PpsbAI :: luxAB, PpsbAI :: luxCDE at NS 2.1, was used as the background for KidA-OX and KidA domain truncation mutant overexpression strains [65, 66]. For the KidA knockout strain ($\Delta kidA$), two ∼500 bp long stretches of *S. elongatus* genome sequence directly upstream and downstream of kidA coding sequence were inserted into the pMR0089 plasmid to flank the gentamicin resistance cassette. By homologous recombination, the native KidA gene in WT/pAM2195 strain was replaced with the gentamicin resistance gene. After propagation on selective media, all mutant alleles were verified by PCR to have fully segregated. The plasmids and strains used in this study are outlined in Table 2.1.

Anti-HA co-IP from cyanobacterial lysate

Cyanobacterial cells were harvested at OD750 = 0.7–1 by centrifugation at 25 °C at maximum speed and were stored in -80 °C after being snap-frozen in liquid nitrogen. Cells from ∼45 ml of culture were used per co-IP experiment. Cells were thawed, pelleted, and resuspended in 250 µl of lysis buffer composed of 50 mM HEPES (pH 7.5), 1 mM EDTA, 1 mM DTT, 0.2% Triton X-100, 50mM NaCl, protease inhibitor, and phosphatase inhibitor. After a 20-minute incubation at 4 °C with gentle agitation, ∼100 µl of 0.1 mm glass beads were added, followed by bead beating (10 reps of 30 seconds vortexing and 30 seconds to 1 minute cooling on ice). The lysed mixture was clarified by centrifugation for 3 minutes at 10000 g. The resulting supernatant was transferred to a new tube and further centrifugated for 1 hour at 9000 g at 4 °C. 50 µl of the supernatant from this second spin was saved as input, and the rest was mixed with Anti-HA magnetic beads (MBL Catalog # M132-11) that were isolated from 50 µl resuspended slurry and equilibrated with the same lysis buffer. The mixture was incubated at 4 °C for 30 minutes with gentle agitation. The beads were pelleted by magnet and the supernatant was removed. After washing with the lysis buffer three times,

the samples were eluted by incubating the beads in 60 µl of 0.1 M Glycine (pH 2) for 10 minutes at room temperature. The beads were removed from the eluate by magnet, and the eluate was neutralized by the addition of ∼12 µl of 1 M Tris (pH 8).

LC-MS/MS analysis of fsKaiB co-IP samples

The eluate samples from the co-IP were submitted to the Harvard Center for Mass Spectrometry (Cambridge, MA) for LC-MS/MS analysis. The samples were first treated using 20mM TCEP/50mM TEAB (Sigma) (1/10 vol/vol ratio, 37 °C incubation for 1 hour, cooled to room temperature for 10 minutes, followed by vortex and spin). Next, 40 mM iodoacetamide (Sigma)/50mM TEAB was added to the sample (1/10 vol/vol ratio, 1 hour incubation at room temperature under tin foil), followed by a 16-hour, 37 °C incubation with Trypsin (Promega) in thermo mixer. The digested samples were vortexed and transferred to an HPLC and was dried to 30 µl to shoot 14/30 µl on Mass Spec. LC-MS/MS was performed on a Orbitrap Elite Hybrid Ion Trap-Orbitrap Mass Spectrometer (Thermo Fischer, San Jose, CA) equipped with WATERS Acquity nano pump nanoLC (WATERS Corp. Milford, MA). Peptides were separated onto a 100 µm inner diameter microcapillary trapping column packed first with approximately 5 cm of C18 Reprosil resin (5 µm, 100 Å, Dr. Maisch GmbH, Germany) followed by WATERS analytical column. Separation was achieved through applying a gradient from 5–27% ACN in 0.1% formic acid over 90 min at 200 nl min^{-1}. Electrospray ionization was enabled through applying a voltage of 1.8 kV using a home-made electrode junction at the end of the microcapillary column. The Elite Orbitrap Velos was operated in data-dependent mode for the mass spectrometry methods. The mass spectrometry survey scan was performed in the Orbitrap in the range of 395–1,800 m/z at a resolution of 6 × 104, followed by the selection of the thirty most intense ions (TOP30) for CID-MS2 fragmentation in the Ion trap using a precursor isolation width window of 2 m/z, AGC setting of 10,000, and a maximum ion accumulation of 200 ms. Singly charged

ion species were not subjected to CID fragmentation.

For the analysis, raw data were submitted in Proteome Discoverer 2.3 software (Thermo Scientific). Assignment of MS/MS spectra was performed using the Sequest HT algorithm by searching the data against a protein sequence database including all entries from the center's Uniprot_Synechococcus ElongatusPCC7942.fasta database as well as other known contaminants such as human keratins and common lab contaminants. Sequest HT searches were performed using a 20-ppm precursor ion tolerance and requiring each peptides N-/C termini to adhere with Trypsin protease specificity, while allowing up to two missed cleavages. A MS2 spectra assignment false discovery rate (FDR) of 1% on both protein and peptide level was achieved by applying the target-decoy database search. Filtering was performed using a Percolator (64bit version) [67]. Peptide N termini and lysine residues (+229.162932 Da) was set as static modifications while methionine oxidation (+15.99492 Da) was set as variable modification.

Anti-HA Western blot

For the experiment shown in Figure 2.4A, 75 ml of KidA-OX strain was grown in 30 °C shaker under constant light to the OD750 of ~ 0.6, which was divided into four 5 ml cultures in glass tubes. At this point, 0, 10, 30, or 70 µM IPTG was added to each culture, which was induced for 20.5 hours in 30 °C with shaking. 4 ml of culture was pelleted and flash frozen in liquid nitrogen. The pellets were resuspended in lysis buffer (8 M Urea, 20 mM HEPES pH 8, 1 mM $MgCl_2$) and lysed using bead beating as described above. Same amounts of lysate, adjusted based on the total protein levels measured by Bradford assay, were subjected to an SDS-PAGE electrophoresis using a 4-20% Criterion TGX gel (Bio-Rad). Proteins separated in the gel were transferred to PVDF membrane via wet transfer. The membrane was blotted using Anti-HA antibody (Biolegend Catalog # 901501) followed by HRP-conjugated secondary antibodies. The membranes were processed with SuperSignal West Femto kit (Thermo

Scientific) and visualized using ChemiDoc (Bio-Rad).

In vivo clock rhythm measurement

A black 96-well plate (Costar) was prepared by filling each well with 250 µl of a BG11M + 0.9% Gelzan (Sigma) pad mixture in off-the-boil liquid state, which then solidified at room temperature. For experiments involving IPTG induction, 10 µl of IPTG solution was added on top of the media pad. The concentration of the IPTG solution was chosen so that the equilibrium concentration in the pad matched the target concentration. E.g., a 0.25 mM IPTG solution was used for 10 µM IPTG induction, which was chosen as the default condition for characterizing clock phenotypes of KidA overexpression strain (condition used for Figures 2.3 A, B, D, and E). At least 3 hours after IPTG addition, 30 µl of cells at OD750 of 0.1–0.3 were added on top of the media pad. The plate was sealed with a transparent film (UniSeal, GE HealthCare Life Sciences) with holes punched by a 26G$\frac{1}{2}$ needle (BD, Franklin Lakes, NJ, Cataloog # 305111) above each well. The plate was placed under a red LED array described in [36] that was programmed to turn on and off accordingly during the entrainment or dark pulse applications, and to stay on for constant light. Every 30 minutes after the initiation of the LED light program, bioluminescence from each well was measured using a TopCount plate reader (PerkinElmer).

Circadian rhythm data fitting and phase response curve analysis

All experimental circadian rhythm data were fit to the following equation:

$$Y = Offset + Slope \cdot X + Amplitude \cdot sin\left(\frac{2\pi(X - PhaseShift)}{Period}\right)$$

Oscillatory traces from individual samples were fit separately, and the best-fit values for each parameter were averaged across replicates. GraphPad Prism was used for data shown in

Figure 2.5D, 2.10A, and 2.10D, and a custom-written Matlab code optimized for generating initial guesses for the parameters was used for analyses in Figures 2.3C, 2.3D, and 2.3E. A time-window greater than 48 h was used to fit each data set. We excluded the initial transient in the data when cultures are rapidly growing (typically the first 12 h). For KidA-OX in Figure 2.3C, only data up to 60 hours in constant light were used to fit the period, because of the arrhythmicity outside of this window in >30 µM IPTG conditions (Figure 2.4). To produce the phase response curves in Figure 2.3E, we first aligned the data for each strain and each condition by shifting the time axis to place the trough of the constant light reporter rhythm prior to the dark pulse at CT = 0. We then rescaled the time axis by a factor 24 h / (FRP), where FRP is the free-running period for strain, estimated by the fitting procedure described above.

Tertiary structure prediction by Phyre2

The Phyre2 algorithm [45] was used to predict local structures in KidA's N-terminal region for domain prediction reported in Figure 2.5B. The N-terminal region was divided into two parts, a domain predicted to be a PAS domain due to high sequence homology (residues 360 to 485, corresponding to PAS-D) and the rest (residues 1 to 359). The outputted 3D structure files from the two submissions were visualized by VMD [68] and for each of the four local tertiary structures, the secondary structure information of each residue was mapped. Intensive mode was used for residues 1 to 359, which resulted in 351 residues (98%) modelled at >90% accuracy. Normal mode was used for residues 360 to 485, which resulted in 99.9% confidence in the model.

In vitro co-IP using FLAG-tagged proteins as bait

Each co-IP sample (20 µl) was prepared in Kai reaction buffer (10% glycerol, 20 mM Tris-HCl pH 8, 150 mM NaCl, 5 mM $MgCl_2$, 0.5 mM EDTA pH 8, 1 mM ATP pH 8) and

snap-frozen in liquid nitrogen at the end of desired length of co-incubation. (See below for details of sample preparation for each experiment.) To isolate the bait protein and its interactors, Anti-FLAG M2 Magnetic beads (Sigma-Aldrich) were used. 10 µl of resuspended bead slurry was used for each co-IP reaction. Beads were washed with Kai reaction buffer by two cycles of pelleting on magnet, buffer removal, and resuspension, and then were resuspended with 10 µl of the reaction sample for binding reaction. After incubating for 10 minutes at 22 °C while shaking at 950 rpm, beads were pelleted on magnet. The supernatant was removed, and the beads were washed twice using Kai reaction buffer. Proteins bound to the beads were then eluted by incubation in 10 µl of 0.75 mg/ml 3x FLAG peptide (Sigma-Aldrich) solution for 40 minutes at 22 °C with 950 rpm shaking. The final supernatant after pelleting the beads was transferred into a fresh tube and centrifugated for 1 minute for complete exclusion of the beads. 7.5 µl of the supernatant was saved and stored in −20 °C. The co-IP samples were visualized by performing SDS-PAGE electrophoresis using precast 4-20% Criterion TGX gel (Bio-Rad), staining the gel using Sypro Ruby (Invitrogen), and imaging the gel using ChemiDoc (Bio-Rad). The band intensity was quantified using ImageJ software by manually defining the rectangular area of each band, along with the background intensity from the neighboring area that was deducted from the band intensity.

Sample preparation for co-IP:

For all co-incubation of purified proteins in this study, samples were incubated in 30 °C. For the experiment shown in Figure 2.5E and Figure 2.7, 3.5 µM of wtKaiB-FLAG or fsKaiB-FLAG (KaiB-1-99-Y7A- I87A-Y93A-FLAG) was mixed with 3.5 µM of KidA PAS-ABC or KaiC-EA in Kai reaction buffer. The mixture was incubated for 30 minutes or 20 hours. For the experiment in Figure 2.5F, 3.5 µM wtKaiB-FLAG was pre-incubated with 0, 0.7, or 3.5 µM of KidA PAS-ABC for 1, 5, or 20 hours. For the experiment in Figure 2.6, the following concentrations were used for each protein: 3.5 µM KaiB-FLAG, 3.5 µM KaiC-EA, 1.5 µM

KaiA, and 3.5 µM KidA PAS-ABC. At the end of intended duration of co-incubation, the samples were snap-frozen in liquid nitrogen and stored at -20 °C. After the samples were thawed, they were immediately subjected to the co-IP procedure, except for the experiment in Figure 2.10F where 3.5 µM KaiC-EA was added to the thawed reaction and incubated at 30 °C for 5 minutes prior to co-IP.

Fluorescence Polarization

Clock reactions were prepared by mixing Kai proteins at their standard concentrations (1.5 µM KaiA, 3.5 µM KaiB, 3.5 µM KaiC) along with 0.2 µM FITC-labeled KaiB^{K25C} in the clock reaction buffer containing 1 mM ATP, similar to the procedure used previously [36]. KidA PAS-ABC was added to the reaction at specified concentrations. 30 µl of the reaction mixture was added to a black 384-well plate, which was sealed with non-fluorescent film (Thermo Scientific, #232698). The plate was loaded into a plate reader (Tecan), which was used to measure fluorescence polarization with 485 nm excitation (20 nm bandpass) and 535 nm emission (25 nm bandpass) using a 510nm dichroic filter. Measurements were taken every 15 min. Reaction buffer-only wells were used as blank.

KaiA-induced KaiC phosphorylation and KaiC auto-dephosphorylation

For KaiA-induced KaiC phosphorylation with or without KidA PAS-ABC, KaiC was first dephosphorylated by incubation at 30 °C for 27 hours. The master mix for each reaction was prepared as follows: 0.4 µM KaiA + 3.5 µM KaiC (negative control), 0.4 µM KaiA + 3.5 µM KaiC + 1.5 µM KidA PAS-ABC (low KidA condition), 0.4 µM KaiA + 3.5 µM KaiC + 3.5 µM KidA PAS-ABC (high KidA condition) in the Kai reaction buffer. KaiA was added last. The master mix reaction was divided into 20 µl aliquots, which were incubated in 30°C. One aliquot of each reaction condition was quenched every 30 minutes by adding 3x SDS-PAGE loading buffer to the sample and was stored in −20 °C. The samples for t

= 0 were harvested by having the 3X SDS-PAGE loading buffer pre-loaded in the tubes before aliquoting. KaiC auto-dephosphorylation sampling was done in a similar manner, except the KaiC aliquot that was taken out from the −80 °C was used immediately after thawing and no KaiA was added. For both experiments, KaiC phosphoform composition at each timepoint was resolved by SDS-PAGE analysis using 10% acrylamide gel (37.5:1 acrylamide:bis-acrylamide), run for 4.5 hours under 30 mA constant current at 12 °C. The gel was stained by SimplyBlue SafeStain (Invitrogen) and imaged using Odyssey imager (LI-COR) or ChemiDoc (Bio-Rad).

Modeling Background

Here, we provide a brief description of the original model of Paijmans et al. [50], which we henceforth term the Paijmans model.

The fundamental unit in the Paijmans model is a KaiC hexamer, and exchange of subunits between hexamers is not considered. The CI domain has a nucleotide binding site that can hydrolyze ATP, a KaiB binding site, and (via associated KaiB) an inhibitory KaiA binding site; the CII domain of each subunit has a nucleotide binding site that can transfer phosphoryl groups to and from S431 and T432 and hydrolyze ATP, and there is a single shared KaiA binding site that acts on all the CII domains in a hexamer. ATP and ADP are assumed to be in excess, such that the nucleotide binding sites are always occupied. CII domains exchange nucleotides only when KaiA is bound to the shared site, with rates that are proportional to the solution concentration of the alternate nucleotide form; CI domains exchange ADP for ATP at a constant rate and become occupied by ADP only through hydrolysis. In the original Paijmans model, the solution concentration of fsKaiB is assumed to be constant, such that binding of KaiB to the CI domain occurs with kinetics that are first-order in the concentration of available CI sites.

In analogy to the Monod-Wyman-Changeux model of cooperativity, a KaiC hexamer can

exist in two states, termed active and inactive. The free energy of the inactive state decreases relative to that of the active state proportionally to the number of phosphorylated serines in the CII domain, ADPs bound in the CI domain, KaiB molecules bound to the CI domain, and KaiA dimers bound to the CI domain. When in the inactive state, the CI domain has a higher affinity for KaiB, and with six KaiB monomers bound, the CI domain can sequester up to six KaiA dimers.

Enumerating all the possible combinations of states of each of the sites for a KaiC hexamer results in an intractably large number of ordinary differential equations, and instead trajectories of the model are generated by kinetic Monte Carlo simulations, which sample only a small fraction of the combinations. Parameters are selected such that the model is thermodynamically consistent: detailed balance (microscopic reversibility) is enforced for all reactions that do not involve ATP hydrolysis.

Modeling KidA

To test the hypothesis that KidA shortens the period of the oscillator by selectively binding to and stabilizing fsKaiB, we modified the Paijmans model to treat KaiB explicitly as follows.

KaiB fold switching is modeled on the monomer level. The KaiB tetramer is not considered. Individual KaiB monomers interconvert between ground state (gs) and fold switched (fs) forms:

$$KaiB_{gs} \underset{kBswitch_r}{\overset{kBswitch_f}{\rightleftharpoons}} KaiB_{fs}$$

KidA only binds fsKaiB, and any KaiB in complex with KidA cannot convert to the ground state until after dissociation:

$$KidA + KaiB_{fs} \underset{kKidA_{off}}{\overset{kKidA_{on}}{\rightleftharpoons}} KidA \cdot KaiB_{fs}$$

Each of the KaiB species can bind to the CI domain with second-order kinetics. fsKaiB and KaiB·KidA complexes bind to CI at the same rate. KaiB in complex with CI is assumed to always be in the fold-switched state, but if not also bound to KidA, KaiB can dissociate from CI directly to the ground state (and the reverse reaction consisting of simultaneous gsKaiB binding and transition to the fold-switched form is included for detailed balance). Different rates are used for active and inactive CI (denoted by $i \in \{A, I\}$ below):

$$CI_i + KaiB_{fs} \underset{k\mathrm{CI}_i B_{fs,off}}{\overset{k\mathrm{CI}_i B_{fs,on}}{\rightleftharpoons}} CI_i \cdot KaiB$$

$$CI_i + KidA \cdot KaiB_{fs} \underset{k\mathrm{CI}_i B_{fs,off}}{\overset{k\mathrm{CI}_i B_{fs,on}}{\rightleftharpoons}} CI_i \cdot KidA \cdot KaiB$$

$$CI_i + KaiB_{gs} \underset{k\mathrm{CI}_i B_{gs,off}}{\overset{k\mathrm{CI}_i B_{gs,on}}{\rightleftharpoons}} CI_i \cdot KaiB$$

$$KidA + CI_i \cdot KaiB \underset{kKidA_{off}}{\overset{kKidA_{on}}{\rightleftharpoons}} CI_i \cdot KidA \cdot KaiB$$

KidA does not interfere with KaiA binding to CI·KaiB complexes, so the reactions of the original model are sufficient to treat KaiA binding.

As in the original Paijmans model, detailed balance is enforced for each reversible reaction. This allows for the constraints

$$k\mathrm{CI}_i B_{g,off} = \frac{k\mathrm{CI}_i BG_{on}\ k\mathrm{CI}_i B_{fs,off}\ kBswitch_r}{kBswitch_f\ k\mathrm{CI}_i B_{fs,on}}$$

where $i \in \{A, I\}$, with i representing the same state in all rate constants within an equation (i.e., there are two such constraint equations in total, one for the active state rate constants and one for the inactive state rate constants).

Parameter exploration

We used Markov Chain Monte Carlo (MCMC) sampling to explore the values of the parameters that we added to extend the model while keeping the parameters of the original Paijmans model at their published values. Specifically, we employed the Goodman-Weare affine invariant sampling scheme, in which an ensemble of parameter sets is simulated in parallel and used to guide the directions of MC moves [69]. During sampling, we represented the parameter values by their natural logarithms; this guaranteed that the rate constants remained positive.

We used an ensemble size of 50 and walk moves with the move size parameter set to 1. For each parameter set, we performed two simulations. Both simulations were 430 hours long with 1.2 µM KaiA dimers, 1.2 µM KaiC hexamers, and 4.8 µM KaiB monomers. One simulation was performed with 0 µM KidA, and the other was performed with 0.7 µM KidA. Initial ensemble members were generated by drawing their parameter values uniformly from ranges of 2×10^{-4} centered on the natural logarithms of the initial values listed in Table 2.4. To set the initial values of the KaiB binding rates, we determined the concentration of fsKaiB for the isolated fold switching equilibrium (i.e., $[fsKaiB]_{\text{iso}} = [\text{KaiB}]_0 \,/\, (1 + \text{kBswitch}_\text{r}/\text{kBswitch}_\text{f})$) and then set $kICIB_{fs,on}$ and $kACIB_{fs,on}$ such that $kICIB_{fs,on}\,[fsKaiB]_{\text{iso}}$ and $kACIB_{fs,on}\,[fsKaiB]_{\text{iso}}$ were equal to the corresponding first-order rates in the original Paijmans model. The initial KaiB unbinding rates were set to be the same as those in the original Paijmans model. Other parameters were chosen in an ad hoc fashion to reproduce experimental observations qualitatively. Two independent MCMC sampling runs for 200 sweeps over the ensemble were performed with different constraints; the acceptance rate was 40% in both cases.

For both sampling runs, proposed parameter sets that produced nonoscillatory trajectories were rejected. Parameter sets that supported oscillations at both 0 µM KidA and 0.7 µM KidA were subject to the following additional biases. To favor trajectories with periods close to 24 hours in the absence of KidA, the squared difference between the period of a

trajectory and 24 hours was subtracted from the log likelihood. To ensure that KaiB binds faster to inactive KaiC than it does to active KaiC, if any KaiB binding rate to active KaiC is greater than the corresponding binding rate to inactive KaiC, the squared difference between logarithms of the two binding rates was subtracted from the log likelihood. Similarly, to ensure that fsKaiB binds to KaiC faster than gsKaiB does, if the difference between the natural logarithm of any fsKaiB binding rate and the natural logarithm of the corresponding gsKaiB binding rate is less than nine (i.e., 10^4 fold), the squared difference between nine and the aforementioned difference between the log rates is subtracted from the log likelihood. These contributions to the log likelihood are

$$L_0 = \left(-\left(T_0 - 24\right)^2 - \mathbf{1}\{\ln\left(k\mathrm{CI}_A B_{fs,on}\right) - \ln\left(k\mathrm{CI}_A B_{gs,on}\right) < 9\}\left(9 - \ln\left(k\mathrm{CI}_A B_{fs,on}\right) + \ln\left(k\mathrm{CI}_A B_{gs,on}\right)\right)^{\mathbf{2}}\right.$$

$$\left. -\mathbf{1}\{\ln\left(k\mathrm{CI}_I B_{fs,on}\right) - \ln\left(k\mathrm{CI}_I B_{gs,on}\right) < 9\}\left(9 - \ln\left(k\mathrm{CI}_I B_{fs,on}\right) + \ln\left(k\mathrm{CI}_I B_{gs,on}\right)\right)^{\mathbf{2}}\right.$$

$$\left. -\mathbf{1}\{\ln\left(k\mathrm{CI}_A B_{fs,on}\right) > \ln\left(k\mathrm{CI}_I B_{fs,on}\right)\}\left(\ln\left(k\mathrm{CI}_A B_{fs,on}\right) - \ln\left(k\mathrm{CI}_I B_{fs,on}\right)\right)^{\mathbf{2}}\right.$$

In the equation above, T_0 is the period at 0 µM KidA and $\mathbf{1}\{\cdot\}$ is an indicator function equal to one if the condition is satisfied and zero otherwise. The biases on the binding rates to active and inactive KaiC are imposed to preserve the roles of those species in the original Paijmans model. The biases on the binding rates of gsKaiB and fsKaiB are imposed so that the effect of KidA on KaiB binding to KaiC is not overwhelmed by the baseline level of KaiB binding: as the gsKaiB binding rate increases, the increased solution concentration of fsKaiB has less impact. Additionally, if the gsKaiB binding rates are greater than the fsKaiB binding rates, the roles of gsKaiB and fsKaiB invert, making the model inconsistent with the established behavior of KaiB.

In the first sampling run, to encourage the sampling of biochemically reasonable values of the affinity of KidA for fsKaiB, a penalty equal to the square of the difference between –7.4 and the natural logarithm of the K_d in units of $\mu\mathrm{m}^{-3}$ of the KidA-fsKaiB binding interaction was subtracted from the log likelihood whenever this quantity was less than –7.4 (corresponding to K_d values smaller than 10^{-11} M). A similar penalty was also subtracted from the log likelihood when the natural logarithm of the K_d in units of $\mu\mathrm{m}^{-3}$ was greater

than 6.4 (corresponding to K_d values greater than $10^{-5}M$). The total log likelihood for oscillatory trajectories was then

$$L_1 = L_0 - \mathbf{1}\{\ln(kKidA_{off}) - \ln(kKidA_{on}) < -7.4\}\,(\ln(kKidA_{off}) - \ln(kKidA_{on}) + 7.4)^{\mathbf{2}}$$

$$- \mathbf{1}\{\ln(kKidA_{off}) - \ln(kKidA_{on}) > 6.4\}\,(\ln(kKidA_{off}) - \ln(kKidA_{on}) - 6.4)^{\mathbf{2}}$$

In the second sampling run, the constraints on the K_d of the KidA-KaiB binding interaction were replaced with a penalty subtracted from the log likelihood equal to the squared difference between the period with 0.7 µM KidA and 20 hours (to constrain the slope to be –5.7 hours / µM KidA), giving a total log likelihood of

$$L_2 = L_0 - (T_{0.7} - 20)^2$$

where $T_{0.7}$ is the period in hours at 0.7 µM KidA.

We show the distributions of period and amplitude sensitivities to [KidA], as represented by the slopes in Figure 2.10D, in Figure 2.11. To estimate the periods, we computed the autocorrelation function of the average number of KaiB bound per KaiC hexamer and then averaged the times between peaks in the autocorrelation function. To determine peak times, the autocorrelation function was interpolated using quadratic splines near each peak. We estimated the amplitudes as the average peak prominence, normalized to 1 for 0 µM KidA. Because the period and amplitude as functions of KidA concentration were generally well fit by lines, we estimated the slopes for Figures 2.11 and 2.12 from only the periods and amplitudes of the oscillator with 0 µM KidA and 0.7 µM KidA. The parameter set used to generate Figure 2.10 was selected from the MCMC results obtained with log likelihood L_1 to have period and amplitude slopes closest to the experimentally observed ones, while maintaining a near-24-hour period in the absence of KidA. The parameter values used to generate Figure 2.10 are listed in Table 2.4.

To determine which parameters contributed the most to the period slope, the nonparametric Spearman correlation coefficient was computed pairwise between all parameters, the period and amplitude slopes, and the dissociation constant of the KidA-fsKaiB binding interaction (KidA-fsKaiB K_d, calculated as $kKidA_{off}/kKidA_{on}$). The resulting correlation matrix for the simulation with log likelihood L_1, which permits larger variation in the period and amplitude slopes, is shown in Figure 2.12A. The two parameters that were most strongly correlated with the period slope are plotted in Figures 2.12B and 2.12C.

In Figure 2.14, we explore the hypothesis that the effect of KidA can be approximated by shifting the equilibrium between the ground state and fold switched forms of KaiB. To do so, we performed simulations in a model without KidA, where the interconversion of the gsKaiB and fsKaiB folds was directly altered by changing the fold switching rate constants ($kBswitch_f$ and $kBswitch_r$), which we refer to as the effective KidA model. The simulations were run for 400 hours with a 5 µL volume reaction, 1.2 µM KaiA dimers, 1.2 µM KaiC hexamers, 4.8 µM KaiB monomers, and 0 µM KidA. The fold switching rates constants were varied uniformly on a base 10 logarithmic scale from –5 to 5 in increments of 0.5; the values of other parameters were the same as those listed in Table 2.4.

2.7.2 Supplementary Information Tables

Table 2.1: Strains information

Strain name	**Plasmid used**	**Background strain**	**Antibiotic Resistance**	**First residue**	**Last residue**
fsKaiB-HA (MRC1109)	MR0114	WT Syn7942	Spec	N/A	N/A
Δ*kidA* (MRC1180)	MR0213	WT/pAM2195	Cm, Gent	N/A	N/A
KidA FL (MRC1185)	MR0214	WT/pAM2195	Cm, Spec	1M	917S
KidA PAS-ABCD (MRC1204)	MR0222	WT/pAM2195	Cm, Spec	1M	485A
KidA PAS-ABC (MRC1205)	MR0223	WT/pAM2195	Cm, Spec	1M	359L
KidA PAS-BCD (MRC1200)	MR0220	WT/pAM2195	Cm, Spec	131L	485A
KidA PAS-A (MRC1207)	MR0224	WT/pAM2195	Cm, Spec	1M	130Q

Table 2.2: List of proteins detected in co-IP/MS experiment performed using fsKaiB as bait in light (L) condition

Rank	**Accession**	**Description**	**Area**
1	Q79PF4	Circadian clock protein kinase KaiC OS=Synechococcus elongatus (strain PCC 7942) GN=kaiC PE=1 SV=1	6.78E+09
2	Q79PF5	Circadian clock protein KaiB OS=Synechococcus elongatus (strain PCC 7942) GN=kaiB PE=1 SV=1	1.96E+09
3	Q31M30	Diguanylate cyclase/phosphodiesterase with PAS/PAC sensor(S) OS=Synechococcus elongatus (strain PCC 7942) GN=Synpcc7942_1859 PE=4 SV=1	1.78E+08
4	Q79PF6	Circadian clock protein KaiA OS=Synechococcus elongatus (strain PCC 7942) GN=kaiA PE=1 SV=1	8.52E+07
5	Q31NT0	Arsenite-activated ATPase (ArsA) OS=Synechococcus elongatus (strain PCC 7942) GN=Synpcc7942_1259 PE=4 SV=1	6.68E+07
6	Q31Q47	RNA-binding region RNP-1 OS=Synechococcus elongatus (strain PCC 7942) GN=Synpcc7942_0790 PE=4 SV=1	5.55E+07
7	Q31KS4	ATP synthase subunit beta OS=Synechococcus elongatus (strain PCC 7942) GN=atpD PE=3 SV=1	3.39E+07
8	Q31LF9	Probable phosphoketolase OS=Synechococcus elongatus (strain PCC 7942) GN=Synpcc7942_2080 PE=3 SV=1	2.44E+07

Table 2.2, continued			
Rank	**Accession**	**Description**	**Area**
9	Q31PZ1	Twitching motility protein OS=Synechococcus elongatus (strain PCC 7942) GN=Synpcc7942_0847 PE=4 SV=1	2.41E+07
10	Q31KP0	Twitching motility protein OS=Synechococcus elongatus (strain PCC 7942) GN=Synpcc7942_2349 PE=4 SV=1	2.29E+07
11	Q31KE3	Methionine aminopeptidase OS=Synechococcus elongatus (strain PCC 7942) GN=map PE=3 SV=1	2.26E+07
12	Q31K60	Uncharacterized protein OS=Synechococcus elongatus (strain PCC 7942) GN=Synpcc7942_2529 PE=4 SV=1	1.97E+07
13	Q31PH5	CheA signal transduction histidine kinase OS=Synechococcus elongatus (strain PCC 7942) GN=Synpcc7942_1014 PE=4 SV=1	1.95E+07
14	Q31MB3	Uncharacterized protein OS=Synechococcus elongatus (strain PCC 7942) GN=Synpcc7942_1776 PE=4 SV=1	1.93E+07
15	Q93AK0	Cell division protein Ftn2 OS=Synechococcus elongatus (strain PCC 7942) GN=Synpcc7942_1943 PE=4 SV=1	1.92E+07
16	Q54775	CTP synthase OS=Synechococcus elongatus (strain PCC 7942) GN=pyrG PE=3 SV=1	1.70E+07
17	Q31QF2	60 kDa chaperonin OS=Synechococcus elongatus (strain PCC 7942) GN=groL PE=3 SV=1	1.69E+07
18	Q31N20	Histidinol dehydrogenase OS=Synechococcus elongatus (strain PCC 7942) GN=hisD PE=3 SV=1	1.67E+07
19	Q9Z3G5	PBS lyase HEAT-like repeat OS=Synechococcus elongatus (strain PCC 7942) GN=nblB PE=4 SV=1	1.46E+07
20	Q8GAA4	Uncharacterized protein OS=Synechococcus elongatus (strain PCC 7942) GN=sek0026 PE=4 SV=1	1.39E+07
21	Q31PX1	Uncharacterized protein OS=Synechococcus elongatus (strain PCC 7942) GN=Synpcc7942_0868 PE=4 SV=1	1.27E+07
22	P11004	Photosystem II CP43 reaction center protein OS=Synechococcus elongatus (strain PCC 7942) GN=psbC PE=3 SV=3	1.25E+07

Table 2.2, continued			
Rank	**Accession**	**Description**	**Area**
23	Q31K58	Elongation factor Ts OS=Synechococcus elongatus (strain PCC 7942) GN=tsf PE=3 SV=1	1.25E+07
24	Q31KE8	Phosphate import ATP-binding protein PstB OS=Synechococcus elongatus (strain PCC 7942) GN=pstB PE=3 SV=1	1.18E+07
25	P22880	10 kDa chaperonin OS=Synechococcus elongatus (strain PCC 7942) GN=groS PE=3 SV=2	1.13E+07
26	Q31RF6	ATP synthase subunit a OS=Synechococcus elongatus (strain PCC 7942) GN=atpB PE=3 SV=2	1.12E+07
27	Q31LR4	Uncharacterized protein OS=Synechococcus elongatus (strain PCC 7942) GN=Synpcc7942_1975 PE=4 SV=1	1.11E+07
28	Q8GJN0	Light-independent protochlorophyllide reductase subunit B OS=Synechococcus elongatus (strain PCC 7942) GN=chlB PE=3 SV=2	1.05E+07
29	Q31NI8	HAD-superfamily hydrolase subfamily IA, variant 3 OS=Synechococcus elongatus (strain PCC 7942) GN=Synpcc7942_1351 PE=4 SV=1	1.01E+07
30	Q31RH4	Uncharacterized protein OS=Synechococcus elongatus (strain PCC 7942) GN=Synpcc7942_0313 PE=4 SV=1	1.00E+07
31	Q31RX9	Rhodanese-like OS=Synechococcus elongatus (strain PCC 7942) GN=Synpcc7942_0158 PE=4 SV=1	8.99E+06
32	Q31PA8	Uncharacterized protein OS=Synechococcus elongatus (strain PCC 7942) GN=Synpcc7942_1081 PE=4 SV=1	8.77E+06
33	Q31P08	NAD(P)H-quinone oxidoreductase subunit K OS=Synechococcus elongatus (strain PCC 7942) GN=ndhK PE=3 SV=1	8.62E+06
34	Q8KPQ7	Guanylate kinase OS=Synechococcus elongatus (strain PCC 7942) GN=gmk PE=3 SV=2	8.43E+06
35	Q31MD1	Probable dual-specificity RNA methyltransferase RlmN OS=Synechococcus elongatus (strain PCC 7942) GN=rlmN PE=3 SV=1	8.39E+06

Table 2.2, continued			
Rank	**Accession**	**Description**	**Area**
36	Q54766	Acetyl-coenzyme A carboxylase carboxyl transferase subunit alpha OS=Synechococcus elongatus (strain PCC 7942) GN=accA PE=3 SV=1	8.24E+06
37	Q31NA4	2-succinyl-5-enolpyruvyl-6-hydroxy-3-cyclohexene-1-carboxylate synthase OS=Synechococcus elongatus (strain PCC 7942) GN=menD PE=3 SV=1	8.24E+06
38	Q31PX7	Uncharacterized protein OS=Synechococcus elongatus (strain PCC 7942) GN=Synpcc7942_0862 PE=4 SV=1	7.27E+06
39	Q31MP2	Uncharacterized protein OS=Synechococcus elongatus (strain PCC 7942) GN=Synpcc7942_1647 PE=4 SV=1	7.25E+06
40	Q31LF8	Probable glycosyl transferase OS=Synechococcus elongatus (strain PCC 7942) GN=Synpcc7942_2081 PE=4 SV=1	7.24E+06
41	Q31N30	tRNA-specific 2-thiouridylase MnmA OS=Synechococcus elongatus (strain PCC 7942) GN=mnmA PE=3 SV=1	7.23E+06
42	P21577	6-phosphogluconate dehydrogenase, decarboxylating OS=Synechococcus elongatus (strain PCC 7942) GN=gnd PE=1 SV=4	7.18E+06
43	Q31KH4	Lysine–tRNA ligase OS=Synechococcus elongatus (strain PCC 7942) GN=lysS PE=3 SV=1	7.08E+06
44	Q54734	SqdB OS=Synechococcus elongatus (strain PCC 7942) GN=sqdB PE=4 SV=1	6.91E+06
45	Q31KY2	Uncharacterized protein OS=Synechococcus elongatus (strain PCC 7942) GN=Synpcc7942_2257 PE=4 SV=1	6.85E+06
46	Q31Q29	HAD-superfamily hydrolase subfamily IIB OS=Synechococcus elongatus (strain PCC 7942) GN=Synpcc7942_0808 PE=4 SV=1	6.76E+06
47	Q31M14	Uncharacterized protein OS=Synechococcus elongatus (strain PCC 7942) GN=Synpcc7942_1875 PE=4 SV=1	6.70E+06
48	Q8VPV7	CO2 hydration protein OS=Synechococcus elongatus (strain PCC 7942) GN=chpY PE=4 SV=1	6.61E+06

Table 2.2, continued			
Rank	**Accession**	**Description**	**Area**
49	Q31KY3	Uncharacterized protein OS=Synechococcus elongatus (strain PCC 7942) GN=Synpcc7942_2256 PE=4 SV=1	6.48E+06
50	Q31QQ2	PDZ/DHR/GLGF OS=Synechococcus elongatus (strain PCC 7942) GN=Synpcc7942_0585 PE=4 SV=1	6.21E+06
51	Q31RD2	Ribosome-binding factor A OS=Synechococcus elongatus (strain PCC 7942) GN=rbfA PE=3 SV=1	6.12E+06
52	Q935Z3	Trigger factor OS=Synechococcus elongatus (strain PCC 7942) GN=tig PE=3 SV=1	6.10E+06
53	Q31NJ4	NADH dehydrogenase subunit 6 OS=Synechococcus elongatus (strain PCC 7942) GN=Synpcc7942_1345 PE=3 SV=1	6.09E+06
54	P52023	DNA polymerase III subunit beta OS=Synechococcus elongatus (strain PCC 7942) GN=dnaN PE=3 SV=1	6.08E+06
55	Q31NF8	ATPase OS=Synechococcus elongatus (strain PCC 7942) GN=Synpcc7942_1381 PE=4 SV=1	5.94E+06
56	Q31LE9	Homoserine dehydrogenase OS=Synechococcus elongatus (strain PCC 7942) GN=Synpcc7942_2090 PE=3 SV=1	5.91E+06
57	Q31RI3	Uncharacterized protein OS=Synechococcus elongatus (strain PCC 7942) GN=Synpcc7942_0304 PE=4 SV=1	5.87E+06
58	Q31MS2	Inner membrane protein-like OS=Synechococcus elongatus (strain PCC 7942) GN=Synpcc7942_1617 PE=3 SV=1	5.84E+06
59	Q31N89	ATPase OS=Synechococcus elongatus (strain PCC 7942) GN=Synpcc7942_1450 PE=4 SV=1	5.76E+06
60	O05347	MalK-like protein OS=Synechococcus elongatus (strain PCC 7942) GN=cynD PE=4 SV=2	5.74E+06
61	Q935Y2	Ribosomal protein S12 methylthiotransferase RimO OS=Synechococcus elongatus (strain PCC 7942) GN=rimO PE=3 SV=1	5.70E+06
62	Q31M19	Secretion protein HlyD OS=Synechococcus elongatus (strain PCC 7942) GN=Synpcc7942_1870 PE=3 SV=1	5.58E+06

Table 2.2, continued			
Rank	**Accession**	**Description**	**Area**
63	Q31S00	Ferrochelatase OS=Synechococcus elongatus (strain PCC 7942) GN=hemH PE=3 SV=1	5.45E+06
64	Q31QN3	Ribulose-phosphate 3-epimerase OS=Synechococcus elongatus (strain PCC 7942) GN=Synpcc7942_0604 PE=3 SV=1	5.27E+06
65	P50020	Chaperone protein dnaK1 OS=Synechococcus elongatus (strain PCC 7942) GN=dnaK1 PE=3 SV=2	5.26E+06
66	Q31PP8	ATPase OS=Synechococcus elongatus (strain PCC 7942) GN=Synpcc7942_0941 PE=4 SV=1	5.23E+06
67	Q31LG9	Twitching motility protein OS=Synechococcus elongatus (strain PCC 7942) GN=Synpcc7942_2070 PE=4 SV=1	5.22E+06
68	Q31S36	Type 2 NADH dehydrogenase OS=Synechococcus elongatus (strain PCC 7942) GN=Synpcc7942_0101 PE=4 SV=1	5.18E+06
69	Q31NL4	Replicative DNA helicase OS=Synechococcus elongatus (strain PCC 7942) GN=Synpcc7942_1325 PE=3 SV=1	5.17E+06
70	Q31L91	ATPase OS=Synechococcus elongatus (strain PCC 7942) GN=Synpcc7942_2148 PE=4 SV=1	5.16E+06
71	Q31PV4	Elongation factor G OS=Synechococcus elongatus (strain PCC 7942) GN=fusA PE=3 SV=1	5.04E+06
72	Q31QI3	Photosystem I assembly protein Ycf4 OS=Synechococcus elongatus (strain PCC 7942) GN=ycf4 PE=3 SV=1	4.96E+06
73	Q31QL1	Dihydroxy-acid dehydratase OS=Synechococcus elongatus (strain PCC 7942) GN=ilvD PE=3 SV=1	4.92E+06
74	Q31P87	Uncharacterized protein OS=Synechococcus elongatus (strain PCC 7942) GN=Synpcc7942_1102 PE=4 SV=1	4.87E+06
75	Q31SB1	Uncharacterized protein OS=Synechococcus elongatus (strain PCC 7942) GN=Synpcc7942_0026 PE=4 SV=1	4.63E+06
76	Q31KR9	Uncharacterized protein OS=Synechococcus elongatus (strain PCC 7942) GN=Synpcc7942_2320 PE=4 SV=1	4.59E+06

Table 2.2, continued			
Rank	**Accession**	**Description**	**Area**
77	Q31K23	Peptidyl-prolyl cis-trans isomerase OS=Synechococcus elongatus (strain PCC 7942) GN=Synpcc7942_2566 PE=4 SV=1	4.44E+06
78	Q31PV7	Peptidase S16, lon-like OS=Synechococcus elongatus (strain PCC 7942) GN=Synpcc7942_0882 PE=4 SV=1	4.43E+06
79	Q31LY0	Uncharacterized protein OS=Synechococcus elongatus (strain PCC 7942) GN=Synpcc7942_1909 PE=4 SV=1	4.41E+06
80	Q31RE1	Laccase domain protein OS=Synechococcus elongatus (strain PCC 7942) GN=Synpcc7942_0346 PE=3 SV=1	4.37E+06
81	Q8KUT3	ANL58 OS=Synechococcus elongatus (strain PCC 7942) GN=Synpcc7942_B2655 PE=4 SV=2	4.33E+06
82	Q31NN4	ATPase OS=Synechococcus elongatus (strain PCC 7942) GN=Synpcc7942_1305 PE=3 SV=1	4.21E+06
83	Q31RS6	Cobyric acid synthase OS=Synechococcus elongatus (strain PCC 7942) GN=cobQ PE=3 SV=1	4.20E+06
84	Q9KHI5	Circadian input kinase OS=Synechococcus elongatus (strain PCC 7942) GN=cikA PE=1 SV=1	4.19E+06
85	Q31NI3	Response regulator receiver domain protein (CheY-like) OS=Synechococcus elongatus (strain PCC 7942) GN=Synpcc7942_1356 PE=4 SV=1	4.06E+06
86	Q31QA3	Uncharacterized protein OS=Synechococcus elongatus (strain PCC 7942) GN=Synpcc7942_0734 PE=4 SV=1	3.99E+06
87	P14788	Sulfate/thiosulfate import ATP-binding protein CysA OS=Synechococcus elongatus (strain PCC 7942) GN=cysA PE=2 SV=1	3.94E+06
88	Q31NF3	Cob(I)yrinic acid a,c-diamide adenosyltransferase OS=Synechococcus elongatus (strain PCC 7942) GN=Synpcc7942_1386 PE=4 SV=1	3.93E+06

Table 2.2, continued			
Rank	**Accession**	**Description**	**Area**
89	Q31Q03	Holliday junction ATP-dependent DNA helicase RuvB OS=Synechococcus elongatus (strain PCC 7942) GN=ruvB PE=3 SV=1	3.88E+06
90	Q31LC0	RNA methyltransferase TrmH, group 3 OS=Synechococcus elongatus (strain PCC 7942) GN=Synpcc7942_2119 PE=3 SV=1	3.82E+06
91	Q8GMQ9	Putative glutathione peroxidase OS=Synechococcus elongatus (strain PCC 7942) GN=sel0033 PE=4 SV=1	3.67E+06
92	Q31QZ9	Dihydroorotase OS=Synechococcus elongatus (strain PCC 7942) GN=Synpcc7942_0488 PE=3 SV=1	3.55E+06
93	Q31LU5	Pyruvate dehydrogenase E1 component subunit alpha OS=Synechococcus elongatus (strain PCC 7942) GN=pdhA PE=4 SV=1	3.54E+06
94	Q31LY5	Hemolysin secretion protein-like OS=Synechococcus elongatus (strain PCC 7942) GN=Synpcc7942_1904 PE=4 SV=1	3.50E+06
95	O07345	Magnesium-chelatase subunit ChlD OS=Synechococcus elongatus (strain PCC 7942) GN=chlD PE=3 SV=2	3.46E+06
96	Q31NH7	Uncharacterized protein OS=Synechococcus elongatus (strain PCC 7942) GN=Synpcc7942_1362 PE=4 SV=1	3.43E+06
97	Q31RH2	Adenylosuccinate lyase OS=Synechococcus elongatus (strain PCC 7942) GN=Synpcc7942_0315 PE=3 SV=1	3.35E+06
98	Q31QS3	ATPase OS=Synechococcus elongatus (strain PCC 7942) GN=Synpcc7942_0564 PE=4 SV=1	3.33E+06
99	Q31KG6	tRNA uridine 5-carboxymethylaminomethyl modification enzyme MnmG OS=Synechococcus elongatus (strain PCC 7942) GN=mnmG PE=3 SV=1	3.29E+06
100	Q31LN3	Uncharacterized protein OS=Synechococcus elongatus (strain PCC 7942) GN=Synpcc7942_2006 PE=4 SV=1	3.23E+06
101	Q8GJM5	Putative uncharacterized protein SEN0014 OS=Synechococcus elongatus (strain PCC 7942) GN=SEN0014 PE=4 SV=1	3.17E+06

Table 2.2, continued			
Rank	**Accession**	**Description**	**Area**
102	Q31K73	Uncharacterized protein OS=Synechococcus elongatus (strain PCC 7942) GN=Synpcc7942_2516 PE=4 SV=1	3.04E+06
103	Q31NE8	Mg chelatase-related protein OS=Synechococcus elongatus (strain PCC 7942) GN=Synpcc7942_1391 PE=4 SV=1	2.98E+06
104	Q31Q32	Uncharacterized protein OS=Synechococcus elongatus (strain PCC 7942) GN=Synpcc7942_0805 PE=4 SV=1	2.92E+06
105	Q8GMT4	Preprotein translocase, SecG subunit OS=Synechococcus elongatus (strain PCC 7942) GN=secG PE=4 SV=1	2.89E+06
106	Q31R08	Elongation factor 4 OS=Synechococcus elongatus (strain PCC 7942) GN=lepA PE=3 SV=1	2.82E+06
107	Q31LN9	Penicillin-binding protein 1A OS=Synechococcus elongatus (strain PCC 7942) GN=Synpcc7942_2000 PE=4 SV=1	2.67E+06
108	Q935X4	ChlA OS=Synechococcus elongatus (strain PCC 7942) GN=SEA0022 PE=4 SV=1	2.60E+06
109	Q31PZ6	NADPH-glutathione reductase OS=Synechococcus elongatus (strain PCC 7942) GN=Synpcc7942_0842 PE=3 SV=1	2.58E+06
110	Q31L26	Adenylate kinase OS=Synechococcus elongatus (strain PCC 7942) GN=adk PE=3 SV=1	2.47E+06
111	Q56002	Serine acetyltransferase OS=Synechococcus elongatus (strain PCC 7942) GN=cysE PE=3 SV=1	2.47E+06
112	Q31NI0	Coenzyme F420 hydrogenase OS=Synechococcus elongatus (strain PCC 7942) GN=Synpcc7942_1359 PE=4 SV=1	2.38E+06
113	Q8RQ68	Multi-sensor signal transduction histidine kinase OS=Synechococcus elongatus (strain PCC 7942) GN=nblS PE=4 SV=1	2.30E+06
114	Q31PS7	DNA polymerase III, tau subunit OS=Synechococcus elongatus (strain PCC 7942) GN=Synpcc7942_0912 PE=4 SV=1	2.27E+06
115	P37279	Probable copper-transporting ATPase PacS OS=Synechococcus elongatus (strain PCC 7942) GN=pacS PE=3 SV=2	2.17E+06

Table 2.2, continued			
Rank	**Accession**	**Description**	**Area**
116	P50590	Nucleoside diphosphate kinase OS=Synechococcus elongatus (strain PCC 7942) GN=ndk PE=3 SV=2	2.04E+06
117	P11005	Photosystem II D2 protein OS=Synechococcus elongatus (strain PCC 7942) GN=psbD1 PE=3 SV=2	2.03E+06
118	Q31KU4	Uncharacterized protein OS=Synechococcus elongatus (strain PCC 7942) GN=Synpcc7942_2295 PE=4 SV=1	2.02E+06
119	Q31M79	Flavoprotein OS=Synechococcus elongatus (strain PCC 7942) GN=Synpcc7942_1810 PE=4 SV=1	1.98E+06
120	Q31KI0	Adenylosuccinate synthetase OS=Synechococcus elongatus (strain PCC 7942) GN=purA PE=3 SV=1	1.97E+06
121	Q31RV9	ATPase OS=Synechococcus elongatus (strain PCC 7942) GN=Synpcc7942_0178 PE=4 SV=1	1.95E+06
122	Q31KN9	Translation factor SUA5 OS=Synechococcus elongatus (strain PCC 7942) GN=Synpcc7942_2350 PE=4 SV=1	1.92E+06
123	Q31M41	Aspartate-semialdehyde dehydrogenase OS=Synechococcus elongatus (strain PCC 7942) GN=asd PE=3 SV=1	1.92E+06
124	Q31S19	Aspartyl/glutamyl-tRNA(Asn/Gln) amidotransferase subunit B OS=Synechococcus elongatus (strain PCC 7942) GN=gatB PE=3 SV=1	1.89E+06
125	Q31KE1	GTPase HflX OS=Synechococcus elongatus (strain PCC 7942) GN=hflX PE=3 SV=1	1.76E+06
126	Q31QJ5	Bacterioferritin comigratory protein OS=Synechococcus elongatus (strain PCC 7942) GN=Synpcc7942_0642 PE=4 SV=1	1.73E+06
127	Q31MA7	L-threonine synthase OS=Synechococcus elongatus (strain PCC 7942) GN=Synpcc7942_1782 PE=4 SV=1	1.53E+06
128	Q31RX7	GTPase Era OS=Synechococcus elongatus (strain PCC 7942) GN=era PE=3 SV=1	1.52E+06
129	Q31LE3	Diguanylate cyclase with GAF sensor OS=Synechococcus elongatus (strain PCC 7942) GN=Synpcc7942_2096 PE=4 SV=1	1.50E+06

Table 2.2, continued			
Rank	**Accession**	**Description**	**Area**
130	Q55041	Phosphoribosylformylglycinamidine synthase subunit PurL OS=Synechococcus elongatus (strain PCC 7942) GN=purL PE=3 SV=3	1.49E+06
131	Q31MB0	DNA repair protein RecN OS=Synechococcus elongatus (strain PCC 7942) GN=Synpcc7942_1779 PE=3 SV=1	1.47E+06
132	Q31Q56	Phosphoenolpyruvate synthase OS=Synechococcus elongatus (strain PCC 7942) GN=Synpcc7942_0781 PE=3 SV=1	1.43E+06
133	Q31RJ4	Uncharacterized protein OS=Synechococcus elongatus (strain PCC 7942) GN=Synpcc7942_0293 PE=4 SV=1	1.40E+06
134	Q31P89	Chromosomal replication initiator protein DnaA OS=Synechococcus elongatus (strain PCC 7942) GN=dnaA PE=3 SV=1	1.38E+06
135	Q31LJ1	Photosystem I P700 chlorophyll a apoprotein A2 OS=Synechococcus elongatus (strain PCC 7942) GN=psaB PE=3 SV=1	1.37E+06
136	Q54769	GTP cyclohydrolase 1 OS=Synechococcus elongatus (strain PCC 7942) GN=folE PE=3 SV=2	1.33E+06
137	Q31QF4	Potassium channel protein OS=Synechococcus elongatus (strain PCC 7942) GN=Synpcc7942_0683 PE=4 SV=1	1.27E+06
138	Q31JZ3	Probable oxidoreductase OS=Synechococcus elongatus (strain PCC 7942) GN=Synpcc7942_2596 PE=4 SV=1	1.24E+06
139	Q8GLI4	Light dependent period OS=Synechococcus elongatus (strain PCC 7942) GN=ldpA PE=1 SV=1	1.22E+06
140	Q31RE4	Photosystem II lipoprotein Psb27 OS=Synechococcus elongatus (strain PCC 7942) GN=psb27 PE=3 SV=1	1.20E+06
141	Q06904	Adaptive-response sensory-kinase SasA OS=Synechococcus elongatus (strain PCC 7942) GN=sasA PE=1 SV=2	1.18E+06
142	Q31R39	Zinc metalloprotease OS=Synechococcus elongatus (strain PCC 7942) GN=Synpcc7942_0448 PE=3 SV=1	1.13E+06

Table 2.2, continued			
Rank	**Accession**	**Description**	**Area**
143	Q31PN2	Cob(I)yrinic acid a,c-diamide adenosyltransferase OS=Synechococcus elongatus (strain PCC 7942) GN=Synpcc7942_0957 PE=4 SV=1	1.06E+06
144	Q31RJ9	Bifunctional protein GlmU OS=Synechococcus elongatus (strain PCC 7942) GN=glmU PE=3 SV=1	1.05E+06
145	Q31Q25	Heat shock protein DnaJ-like OS=Synechococcus elongatus (strain PCC 7942) GN=Synpcc7942_0812 PE=4 SV=1	1.05E+06
146	Q31PY0	CheA signal transduction histidine kinase OS=Synechococcus elongatus (strain PCC 7942) GN=Synpcc7942_0859 PE=4 SV=1	1.02E+06
147	Q31LJ0	Photosystem I P700 chlorophyll a apoprotein A1 OS=Synechococcus elongatus (strain PCC 7942) GN=psaA PE=3 SV=1	1.01E+06
148	Q31MX7	ADP-ribosylglycohydrolase-like OS=Synechococcus elongatus (strain PCC 7942) GN=Synpcc7942_1562 PE=4 SV=1	9.99E+05
149	Q31RX1	Uncharacterized protein OS=Synechococcus elongatus (strain PCC 7942) GN=Synpcc7942_0166 PE=4 SV=1	9.72E+05
150	Q31KD8	Putative type IV pilus assembly protein PilO OS=Synechococcus elongatus (strain PCC 7942) GN=Synpcc7942_2451 PE=4 SV=1	9.21E+05
151	Q31MT1	Mannose-1-phosphate guanylyltransferase (GDP) OS=Synechococcus elongatus (strain PCC 7942) GN=Synpcc7942_1608 PE=3 SV=1	8.90E+05
152	P38045	Nitrate transport ATP-binding protein NrtC OS=Synechococcus elongatus (strain PCC 7942) GN=nrtC PE=3 SV=1	8.77E+05
153	Q31LA7	Phosphoglucosamine mutase OS=Synechococcus elongatus (strain PCC 7942) GN=glmM PE=3 SV=1	7.93E+05
154	Q31NE2	Uncharacterized protein OS=Synechococcus elongatus (strain PCC 7942) GN=Synpcc7942_1397 PE=4 SV=1	6.74E+05
155	Q31KC6	S-adenosylmethionine synthase OS=Synechococcus elongatus (strain PCC 7942) GN=metK PE=3 SV=1	6.51E+05

Table 2.2, continued			
Rank	**Accession**	**Description**	**Area**
156	Q31RW6	Cysteine synthase OS=Synechococcus elongatus (strain PCC 7942) GN=Synpcc7942_0171 PE=4 SV=1	6.30E+05
157	Q31LG1	Phosphoglycerate mutase OS=Synechococcus elongatus (strain PCC 7942) GN=Synpcc7942_2078 PE=4 SV=1	5.60E+05
158	Q31QC5	C-terminal processing peptidase-2. Serine peptidase. MEROPS family S41A OS=Synechococcus elongatus (strain PCC 7942) GN=Synpcc7942_0712 PE=3 SV=1	5.42E+05

Table 2.3: List of proteins detected in co-IP/MS experiment performed using fsKaiB as bait in dark (D) condition

Rank	**Accession**	**Description**	**Area**
1	Q79PF4	Circadian clock protein kinase KaiC OS=Synechococcus elongatus (strain PCC 7942) GN=kaiC PE=1 SV=1	4.13E+09
2	Q79PF5	Circadian clock protein KaiB OS=Synechococcus elongatus (strain PCC 7942) GN=kaiB PE=1 SV=1	2.83E+08
3	Q31Q47	RNA-binding region RNP-1 OS=Synechococcus elongatus (strain PCC 7942) GN=Synpcc7942_0790 PE=4 SV=1	7.74E+07
4	Q31MB3	Uncharacterized protein OS=Synechococcus elongatus (strain PCC 7942) GN=Synpcc7942_1776 PE=4 SV=1	5.93E+07
5	Q31K58	Elongation factor Ts OS=Synechococcus elongatus (strain PCC 7942) GN=tsf PE=3 SV=1	5.43E+07
6	Q31K73	Uncharacterized protein OS=Synechococcus elongatus (strain PCC 7942) GN=Synpcc7942_2516 PE=4 SV=1	5.12E+07
7	Q31MS5	50S ribosomal protein L34 OS=Synechococcus elongatus (strain PCC 7942) GN=rpmH PE=3 SV=1	2.74E+07
8	P22880	10 kDa chaperonin OS=Synechococcus elongatus (strain PCC 7942) GN=groS PE=3 SV=2	2.59E+07

Table 2.3, continued			
Rank	**Accession**	**Description**	**Area**
9	Q31P07	NAD(P)H-quinone oxidoreductase subunit J OS=Synechococcus elongatus (strain PCC 7942) GN=ndhJ PE=3 SV=1	2.37E+07
10	Q935Z3	Trigger factor OS=Synechococcus elongatus (strain PCC 7942) GN=tig PE=3 SV=1	2.17E+07
11	P29801	NAD(P)H-quinone oxidoreductase subunit 2 OS=Synechococcus elongatus (strain PCC 7942) GN=ndhB PE=3 SV=1	2.14E+07
12	Q8KPQ7	Guanylate kinase OS=Synechococcus elongatus (strain PCC 7942) GN=gmk PE=3 SV=2	2.03E+07
13	Q31P08	NAD(P)H-quinone oxidoreductase subunit K OS=Synechococcus elongatus (strain PCC 7942) GN=ndhK PE=3 SV=1	1.82E+07
14	Q31RD2	Ribosome-binding factor A OS=Synechococcus elongatus (strain PCC 7942) GN=rbfA PE=3 SV=1	1.71E+07
15	Q31PT9	Uncharacterized protein OS=Synechococcus elongatus (strain PCC 7942) GN=Synpcc7942_0900 PE=4 SV=1	1.64E+07
16	Q31LP8	Large-conductance mechanosensitive channel OS=Synechococcus elongatus (strain PCC 7942) GN=mscL PE=3 SV=1	1.63E+07
17	Q79PF6	Circadian clock protein KaiA OS=Synechococcus elongatus (strain PCC 7942) GN=kaiA PE=1 SV=1	1.60E+07
18	Q31N52	30S ribosomal protein S4 OS=Synechococcus elongatus (strain PCC 7942) GN=rpsD PE=3 SV=1	1.60E+07
19	Q8GJL5	CBS OS=Synechococcus elongatus (strain PCC 7942) GN=SEM0025 PE=4 SV=1	1.44E+07
20	Q31KS4	ATP synthase subunit beta OS=Synechococcus elongatus (strain PCC 7942) GN=atpD PE=3 SV=1	1.44E+07
21	Q31QF2	60 kDa chaperonin OS=Synechococcus elongatus (strain PCC 7942) GN=groL PE=3 SV=1	1.43E+07
22	P21577	6-phosphogluconate dehydrogenase, decarboxylating OS=Synechococcus elongatus (strain PCC 7942) GN=gnd PE=1 SV=4	1.41E+07

Table 2.3, continued			
Rank	**Accession**	**Description**	**Area**
23	Q31MB6	Uncharacterized protein OS=Synechococcus elongatus (strain PCC 7942) GN=Synpcc7942_1773 PE=4 SV=1	1.22E+07
24	P16891	Uroporphyrinogen decarboxylase OS=Synechococcus elongatus (strain PCC 7942) GN=hemE PE=3 SV=2	1.20E+07
25	Q31N54	Uncharacterized protein OS=Synechococcus elongatus (strain PCC 7942) GN=Synpcc7942_1485 PE=4 SV=1	1.15E+07
26	Q31KY2	Uncharacterized protein OS=Synechococcus elongatus (strain PCC 7942) GN=Synpcc7942_2257 PE=4 SV=1	1.00E+07
27	Q31LC1	Uncharacterized protein OS=Synechococcus elongatus (strain PCC 7942) GN=Synpcc7942_2118 PE=4 SV=1	9.78E+06
28	Q31Q75	Uncharacterized protein OS=Synechococcus elongatus (strain PCC 7942) GN=Synpcc7942_0762 PE=4 SV=1	9.75E+06
29	Q31SD0	Uncharacterized protein OS=Synechococcus elongatus (strain PCC 7942) GN=Synpcc7942_0007 PE=4 SV=1	9.58E+06
30	Q31RI3	Uncharacterized protein OS=Synechococcus elongatus (strain PCC 7942) GN=Synpcc7942_0304 PE=4 SV=1	9.40E+06
31	Q31S36	Type 2 NADH dehydrogenase OS=Synechococcus elongatus (strain PCC 7942) GN=Synpcc7942_0101 PE=4 SV=1	9.16E+06
32	Q31NR2	50S ribosomal protein L20 OS=Synechococcus elongatus (strain PCC 7942) GN=rplT PE=3 SV=1	8.69E+06
33	Q31M43	Ribonuclease J OS=Synechococcus elongatus (strain PCC 7942) GN=rnj PE=3 SV=1	8.63E+06
34	Q31LC0	RNA methyltransferase TrmH, group 3 OS=Synechococcus elongatus (strain PCC 7942) GN=Synpcc7942_2119 PE=3 SV=1	7.94E+06
35	Q31S48	Carboxymethylenebutenolidase OS=Synechococcus elongatus (strain PCC 7942) GN=Synpcc7942_0089 PE=4 SV=1	7.53E+06
36	Q31RX9	Rhodanese-like OS=Synechococcus elongatus (strain PCC 7942) GN=Synpcc7942_0158 PE=4 SV=1	7.27E+06

Table 2.3, continued			
Rank	**Accession**	**Description**	**Area**
37	Q31L05	NAD(P)H-quinone oxidoreductase subunit N OS=Synechococcus elongatus (strain PCC 7942) GN=ndhN PE=3 SV=1	6.77E+06
38	Q31LY1	Uncharacterized protein OS=Synechococcus elongatus (strain PCC 7942) GN=Synpcc7942_1908 PE=4 SV=1	6.68E+06
39	Q31N63	Uncharacterized protein OS=Synechococcus elongatus (strain PCC 7942) GN=Synpcc7942_1476 PE=4 SV=1	6.66E+06
40	Q31MF5	Ferredoxin-thioredoxin reductase, catalytic chain OS=Synechococcus elongatus (strain PCC 7942) GN=Synpcc7942_1734 PE=3 SV=1	6.60E+06
41	Q31LR4	Uncharacterized protein OS=Synechococcus elongatus (strain PCC 7942) GN=Synpcc7942_1975 PE=4 SV=1	6.58E+06
42	Q31M30	Diguanylate cyclase/phosphodiesterase with PAS/PAC sensor(S) OS=Synechococcus elongatus (strain PCC 7942) GN=Synpcc7942_1859 PE=4 SV=1	5.71E+06
43	Q31RH4	Uncharacterized protein OS=Synechococcus elongatus (strain PCC 7942) GN=Synpcc7942_0313 PE=4 SV=1	5.60E+06
44	Q31MP1	Putative ferric uptake regulator, FUR family OS=Synechococcus elongatus (strain PCC 7942) GN=Synpcc7942_1648 PE=3 SV=1	5.41E+06
45	Q31PV4	Elongation factor G OS=Synechococcus elongatus (strain PCC 7942) GN=fusA PE=3 SV=1	5.40E+06
46	Q31K82	Uncharacterized protein OS=Synechococcus elongatus (strain PCC 7942) GN=Synpcc7942_2507 PE=4 SV=1	5.15E+06
47	Q31Q17	Uncharacterized protein OS=Synechococcus elongatus (strain PCC 7942) GN=Synpcc7942_0820 PE=4 SV=1	5.15E+06
48	P52023	DNA polymerase III subunit beta OS=Synechococcus elongatus (strain PCC 7942) GN=dnaN PE=3 SV=1	4.87E+06
49	O07345	Magnesium-chelatase subunit ChlD OS=Synechococcus elongatus (strain PCC 7942) GN=chlD PE=3 SV=2	4.81E+06

Table 2.3, continued			
Rank	**Accession**	**Description**	**Area**
50	Q31MN3	Catalase-peroxidase OS=Synechococcus elongatus (strain PCC 7942) GN=katG PE=1 SV=1	4.49E+06
51	Q31QQ2	PDZ/DHR/GLGF OS=Synechococcus elongatus (strain PCC 7942) GN=Synpcc7942_0585 PE=4 SV=1	4.48E+06
52	Q31NW5	ABC-transporter membrane fusion protein OS=Synechococcus elongatus (strain PCC 7942) GN=Synpcc7942_1224 PE=4 SV=1	4.24E+06
53	Q31K60	Uncharacterized protein OS=Synechococcus elongatus (strain PCC 7942) GN=Synpcc7942_2529 PE=4 SV=1	4.19E+06
54	Q93AK0	Cell division protein Ftn2 OS=Synechococcus elongatus (strain PCC 7942) GN=Synpcc7942_1943 PE=4 SV=1	4.13E+06
55	Q31PH5	CheA signal transduction histidine kinase OS=Synechococcus elongatus (strain PCC 7942) GN=Synpcc7942_1014 PE=4 SV=1	3.92E+06
56	Q31QZ9	Dihydroorotase OS=Synechococcus elongatus (strain PCC 7942) GN=Synpcc7942_0488 PE=3 SV=1	3.85E+06
57	Q31M83	Bacterioferritin comigratory protein OS=Synechococcus elongatus (strain PCC 7942) GN=Synpcc7942_1806 PE=4 SV=1	3.82E+06
58	Q31RA7	Uncharacterized protein OS=Synechococcus elongatus (strain PCC 7942) GN=Synpcc7942_0380 PE=4 SV=1	3.72E+06
59	Q8GAA4	Uncharacterized protein OS=Synechococcus elongatus (strain PCC 7942) GN=sek0026 PE=4 SV=1	3.72E+06
60	Q31S19	Aspartyl/glutamyl-tRNA(Asn/Gln) amidotransferase subunit B OS=Synechococcus elongatus (strain PCC 7942) GN=gatB PE=3 SV=1	3.61E+06
61	Q31RH2	Adenylosuccinate lyase OS=Synechococcus elongatus (strain PCC 7942) GN=Synpcc7942_0315 PE=3 SV=1	3.50E+06
62	Q31LY0	Uncharacterized protein OS=Synechococcus elongatus (strain PCC 7942) GN=Synpcc7942_1909 PE=4 SV=1	3.40E+06
63	Q31NC9	2-isopropylmalate synthase OS=Synechococcus elongatus (strain PCC 7942) GN=leuA PE=3 SV=1	3.38E+06

Table 2.3, continued			
Rank	**Accession**	**Description**	**Area**
64	Q31S12	Imidazoleglycerol-phosphate dehydratase OS=Synechococcus elongatus (strain PCC 7942) GN=hisB PE=3 SV=1	3.12E+06
65	P11004	Photosystem II CP43 reaction center protein OS=Synechococcus elongatus (strain PCC 7942) GN=psbC PE=3 SV=3	3.00E+06
66	P50020	Chaperone protein dnaK1 OS=Synechococcus elongatus (strain PCC 7942) GN=dnaK1 PE=3 SV=2	2.99E+06
67	Q31L26	Adenylate kinase OS=Synechococcus elongatus (strain PCC 7942) GN=adk PE=3 SV=1	2.97E+06
68	Q31LQ7	NAD(P)H-quinone oxidoreductase subunit M OS=Synechococcus elongatus (strain PCC 7942) GN=ndhM PE=3 SV=1	2.96E+06
69	P53533	Chaperone protein ClpB 1 OS=Synechococcus elongatus (strain PCC 7942) GN=clpB1 PE=2 SV=3	2.88E+06
70	Q31PH4	Methyl-accepting chemotaxis sensory transducer OS=Synechococcus elongatus (strain PCC 7942) GN=Synpcc7942_1015 PE=4 SV=1	2.85E+06
71	Q31LT9	Uncharacterized protein OS=Synechococcus elongatus (strain PCC 7942) GN=Synpcc7942_1950 PE=4 SV=1	2.73E+06
72	Q31NH5	Uncharacterized protein OS=Synechococcus elongatus (strain PCC 7942) GN=Synpcc7942_1364 PE=4 SV=1	2.70E+06
73	Q31LN3	Uncharacterized protein OS=Synechococcus elongatus (strain PCC 7942) GN=Synpcc7942_2006 PE=4 SV=1	2.64E+06
74	Q31N41	Uncharacterized protein OS=Synechococcus elongatus (strain PCC 7942) GN=Synpcc7942_1498 PE=4 SV=1	2.47E+06
75	Q31M14	Uncharacterized protein OS=Synechococcus elongatus (strain PCC 7942) GN=Synpcc7942_1875 PE=4 SV=1	2.37E+06
76	Q31MF2	Iron-regulated ABC transporter permease protein SufD OS=Synechococcus elongatus (strain PCC 7942) GN=Synpcc7942_1737 PE=4 SV=1	2.25E+06

Table 2.3, continued			
Rank	**Accession**	**Description**	**Area**
77	Q935X2	Phospho-2-dehydro-3-deoxyheptonate aldolase OS=Synechococcus elongatus (strain PCC 7942) GN=SEB0024 PE=3 SV=2	2.21E+06
78	Q31QN3	Ribulose-phosphate 3-epimerase OS=Synechococcus elongatus (strain PCC 7942) GN=Synpcc7942_0604 PE=3 SV=1	2.13E+06
79	Q31LU5	Pyruvate dehydrogenase E1 component subunit alpha OS=Synechococcus elongatus (strain PCC 7942) GN=pdhA PE=4 SV=1	1.94E+06
80	Q31S38	Uncharacterized protein OS=Synechococcus elongatus (strain PCC 7942) GN=Synpcc7942_0099 PE=4 SV=1	1.59E+06
81	Q31R39	Zinc metalloprotease OS=Synechococcus elongatus (strain PCC 7942) GN=Synpcc7942_0448 PE=3 SV=1	1.40E+06
82	Q31MS7	Pyridine nucleotide transhydrogenase alpha subunit OS=Synechococcus elongatus (strain PCC 7942) GN=Synpcc7942_1612 PE=4 SV=1	1.29E+06
83	O68523	Response regulator NblR OS=Synechococcus elongatus (strain PCC 7942) GN=nblR PE=4 SV=1	1.22E+06

Table 2.4: Model parameters introduced in the modified model. The binding rate constants have units of µm^3 * (molecule^2 * hour)$^{-1}$, and all other rate constants have units of (molecule * hour)$^{-1}$. Rate constants converted to units of (hour)$^{-1}$ and (µM * hour)$^{-1}$ are given in parentheses.

Name	**Description**	**Initial values**	**Values used for Figure 2.10**
$kACI_AB_{fs,on}$	Rate of fsKaiB binding to active KaiC hexamers	5.4×10^2 (3.3×10^5)	1.4×10^2 (8.6×10^4)
$kACI_AB_{gs,on}$	Rate of ground state KaiB binding to active KaiC hexamers	1.7×10^{-4} (1.0×10^{-1})	4.5×10^{-5} (2.8×10^{-2})
$kACI_AB_{fs,off}$	Rate of KaiB unbinding from active KaiC hexamers as fsKaiB	3.7 (3.7)	1.3×10^2 (1.3×10^2)
$kACI_IB_{fs,on}$	Rate of fsKaiB binding to inactive KaiC hexamers	4.0×10^3 (2.4×10^6)	2.4×10^3 (1.5×10^6)
$kACI_IB_{gs,on}$	Rate of ground state KaiB binding to inactive KaiC hexamers	1.4×10^{-1} (84)	3.8×10^{-1} (2.2×10^2)
$kACI_IB_{fs,off}$	Rate of KaiB unbinding from inactive KaiC hexamers as fsKaiB	9.2×10^{-3} (9.2×10^{-3})	5.0×10^{-2} (5.0×10^{-2})
$kBswitch_f$	Rate of KaiB activation (fold switching)	1.9×10^{-1} (1.9×10^{-1})	1.7×10^{-2} (1.7×10^{-2})
$kBswitch_r$	Rate of KaiB inactivation (reversion to ground state)	2.2×10^3 (2.2×10^3)	4.3×10^1 (4.3×10^1)
$kKidA_{on}$	Rate of KidA binding to fsKaiB	22 (1.3×10^4)	1.2×10^2 (7.2×10^4)
$kKidA_{off}$	Rate of KidA unbinding from KaiB	7.8 (7.8)	1.1×10^1 (1.1×10^1)

2.8 Acknowledgments

We thank Carrie Partch and Andy LiWang for useful discussions, and the LiWang lab for the gift of the fsKaiB mutant protein. We thank Rust lab members for their suggestions on the manuscript. We thank Bogdan Budnik and Renee Robinson at the Harvard Center for Mass Spectrometry for their analysis of samples. This work was supported by an HHMI Simons Faculty Scholar award and NIH Grant R01 GM107369 to M.J.R. and NSF Award MCB-1953402 to A.R.D.

CHAPTER 3

THE EFFECT OF RHYTHMIC FEEDING OF GLUCOSE ON THE PANCREATIC BETA CELLS

3.1 Abstract

Pancreatic beta cells perform an important function in the regulation of blood glucose through the secretion of insulin. Beta cells that are exposed to elevated levels of glucose experience impairment in their function and survival. This effect, referred to as glucotoxicity, is linked to Type 2 Diabetes and therefore warrants further investigation. Like many other systems in different parts of the human body, pancreatic beta cell functions involve clock-controlled, rhythmically expressed genes. While the importance of clock regulation and rhythmic gene expression in beta cells was well elucidated in previous studies using genetic manipulations, the effect of a rhythmic metabolic input is still not fully understood. Thus, we aimed to investigate the effect of cycling glucose levels on the beta cell phenotype. Many recent *in vivo* studies suggest that limiting food consumption to a restricted duration of day (termed time-restricted feeding) improves the animal's (or human's) metabolic health. We hypothesize that a similar effect might be present at the cellular level and could manifest in a cell culture system. In this preliminary study, we investigated glucotoxicity in the beta-TC-6 cell line. We observed a deleterious effect of constant exposure to high glucose on beta-TC-6 cell growth. We also tested the effect of alternating high- and low-glucose every 12 hours, analogous to the time-restricted feeding scheme. Our preliminary result suggests that growing beta-TC-6 cells in cycling levels of glucose leads to better cell growth compared to constant glucose. These results suggest that rhythmic glucose input could be beneficial for the beta cell function and that beta-TC-6 cell line is a useful, easy-to-use alternative to primary beta cells for investigating questions related to glucotoxicity. We expect that our *in vitro* approach can contribute to the unveiling of the direct link between the glucose

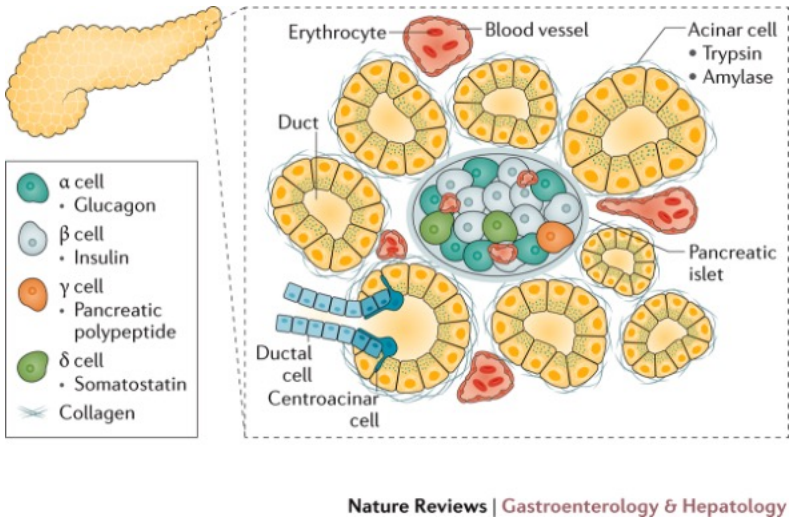

Figure 3.1: The composition and context of the pancreatic islet within the pancreas. Reproduced from [72].

input and the cellular responses, without confounding factors such as animal behavior or tissue-scale mechanisms.

3.2 Introduction

In healthy mammals, blood glucose homeostasis is tightly regulated by the actions of islets of Langerhans in the pancreas. These pancreatic islets are composed of different cell types, which include β cells that secrete insulin, along with α cells (produce glucagon), γ cells (produce pancreatic polypeptide), δ cells (produce somatostatin), and ϵ cells (produce ghrelin) [70, 71] (Figure 3.1).

Understanding the processes in pancreatic beta cells is particularly important, as beta cell defects often underlie metabolic disorders. The essential function performed by beta cells is the secretion of insulin, a hormone that activates signaling pathways that lead to suppression of glucose production in the liver and promotion of glucose uptake in various tissue types [73, 74]. Intracellular glucose initiates the secretion of insulin by beta cells through the glucose-stimulated insulin secretion (GSIS) pathway [71]. This glucose-insulin feedback allows for tight regulation of the blood glucose level in a narrow range. Through

this mechanism, plasma glucose returns to its basal level within a couple of hours after meal intake. The failure of beta cells to secrete adequate levels of insulin leads to Type 2 diabetes [75, 76, 77].

In addition to serving as the acute stimulus for the insulin secretion pathway in beta cells, glucose also has long term effect on beta cell function and survival, facilitating expression of important genes that are involved in the insulin secretion pathway, including the insulin gene itself [78]. Hypoglycemia is thus particularly deleterious for beta cells, in addition to causing problems to other cell types and tissues due to the resulting reduction of available energy.

While a physiological level of glucose is crucial for both beta cell function and survival, a supraphysiological level of glucose is known to be toxic to beta cells, an effect termed glucotoxicity. Previous reports show that primary beta cells and pancreatic islets suffer higher cell death and defects from both hypoglycemia and hyperglycemia [79, 80, 81, 82]. An example of such experimental data, reported by Efanova et al. [79], is shown in Figure 3.2. In the studies cited above, the cultures were grown in constant, high glucose for 18 hours [82], 40 hours [79], 1 week [81], or a range of time from 18 hours to 1 week in [80]. These results suggest that glucotoxicity can occur from a relatively short duration of high-glucose treatment, as opposed to the previously considered notion that months or years of hyperglycemia is needed to elicit glucotoxicity [78].

While using a constant amount of glucose for an extended period of time is useful for establishing the glucotoxic phenotype of beta cells, effects resulting from the realistic, daily fluctuations of glucose levels are missed in such studies. In the context of a live animal's pancreas, intracellular glucose levels are expected to fluctuate, aligned with the behavioral rhythm; typically, glucose levels would be elevated during the day with food consumption and stay low during the night while the animal is inactive.

In this study, we sought to investigate the effect of dynamic glucose input on beta cells

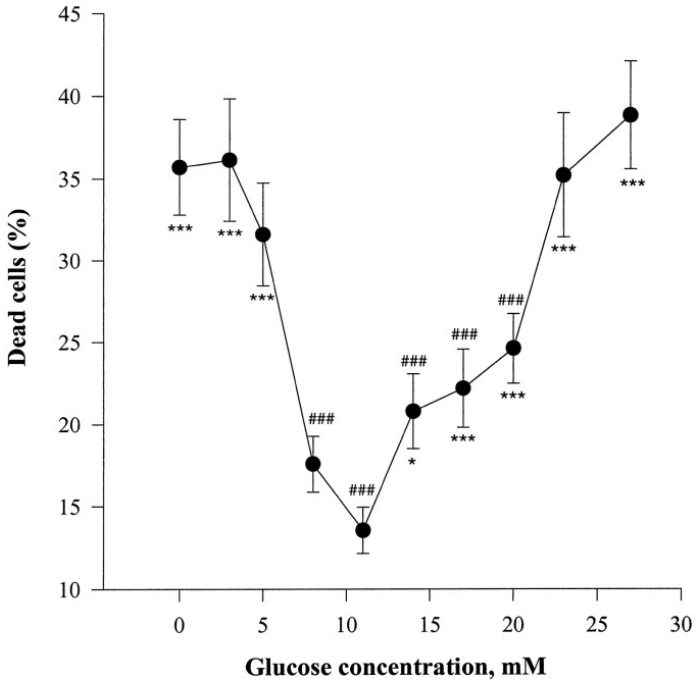

Figure 3.2: Cell death of primary rodent beta cells is higher in both hypoglycemic and hyperglycemic conditions. Reproduced from [79]. Figure caption from the original article: *Percentage of dead cells detected by staining with the DNA binding dye HO 342 using fluorescence microscopy. The percentages of dead cells were assessed in the single cell preparations on glass coverslips after a culture period of 40 h and subsequent staining with the DNA binding dye HO 342. Dead cells were detected by their fragmented nuclei. In each condition, a minimum of 1000 cells from 3 different isolations was counted. Percentages of dead cells are expressed as mean ±S.E. Statistical significance of differences was calculated by unpaired t test. ***, $p < 0.0001$ and *, $p < 0.05$ relative to 11 mM glucose; ###, $p < 0.0001$ relative to 0 mM glucose.*

using an immortalized beta cell line. We could speculate that beta cell function likely has evolved to accommodate the rise-and-fall of blood glucose throughout the day caused by natural behavior of most mammals, such that constant exposure to high glucose could present a challenge to the beta cell systems. Thus, we hypothesize that beta cell glucotoxicity could be alleviated when cells are exposed to high glucose in a cycling manner as opposed to continuous exposure. Recent reports of health benefits observed using time-restricted feeding [29] are conceptually consistent with our hypothesis. We expect that *in vitro* studies equivalent to the *in vivo* time-restricted feeding studies could potentially elucidate important cellular and molecular details underlying the benefits of restricting meal intake or glucose

input to a limited window of time each day. Another motivation for this study stems from the recent studies that demonstrated that the cell-autonomous circadian clock in beta cells plays an important regulatory role. The expression of many components of beta cell functions are affected by clock components CLOCK and BMAL1, and clock disruptions in beta cells lead to Type 2 diabetes in mice [83, 84]. Whether rhythmic glucose input will have any effect on the beta cell clock and the rhythmicity of beta cell components is an interesting question.

We chose to use beta-TC-6 cell line in this study, because among the different beta cell lines, beta-TC-6 cells preserve key functionalities of beta cells including glucose-stimulated insulin secretion [85, 86, 87]. A high concentration of glucose was shown to induce a glucotoxic effect in beta-TC-6 cells in Venieratos et al. [88], which suggests beta-TC-6 is a reasonable system to use for studying the above mentioned hypotheses regarding glucotoxicity.

3.3 Preliminary results

3.3.1 Beta-TC-6 cells exposed to constantly high or constantly low concentrations of glucose experience growth impairment

First, we characterized the effect of various glucose concentrations on beta cell proliferation using a live-cell imaging approach. Beta-TC-6 cells seeded on a 24-well microplate were grown in various concentrations of glucose ranging from 0 to 100 mM in serum-less DMEM media containing 0.25% BSA, which was the condition used in a previous study that observed increase in apoptosis of beta-TC-6 cells at a high glucose concentration [88]. The real-time growth of the beta-TC-6 cells was monitored by live-cell imaging using Incucyte (Sartorius). Raw confluence time-course data from t = 0 to t = 48 h obtained from different fields of view were normalized by the initial (t = 0) value, converting the data to unit-less confluence fold change. Next, the slope of the confluence fold change values plotted against time was

estimated by linear regression and was used as a proxy for cell growth rate (Figure 3.3).

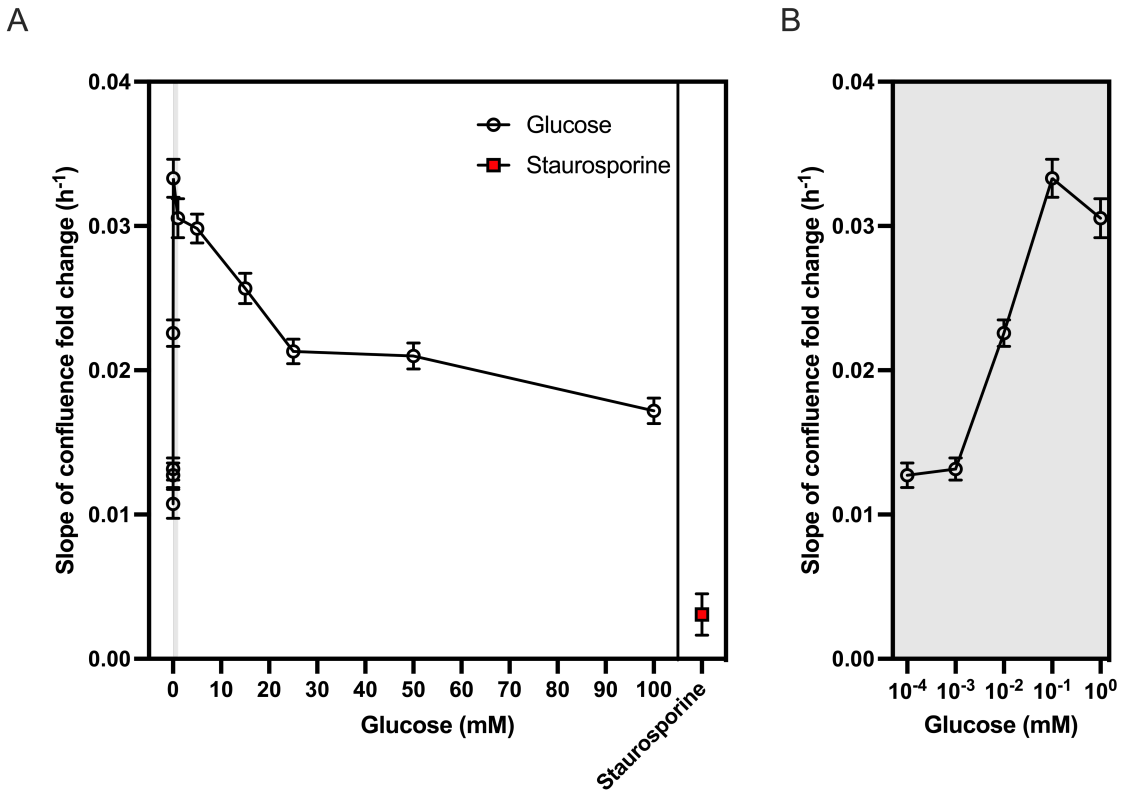

Figure 3.3: Beta-TC-6 cells growth is impaired during constant exposure to too-low or too-high concentrations of glucose. The total osmolarity change in different glucose concentrations was controlled to be the same by balancing with D-mannitol. (A) Mean slope values of the confluence trajectories during the exposure to a given glucose concentration normalized by t=0 value. Error bars show the SEM (n=29-48). Staurosporine (apoptosis inducer) was used as a positive control. (B) The data for glucose concentrations from 0.1 µM to 1 mM, marked by the gray shade in (A), were re-plotted in logarithmic x-axis for better visibility.

Consistent with previous reports [88, 85], around 1 mM glucose best supported the beta-TC-6 cell growth. Glucose concentrations higher than the optimal concentration resulted in a reduction of the average slope of confluence fold change, indicating glucotoxicity. Zero glucose, as well as the apoptosis inducer Staurosporine, seriously impaired growth as expected (Figure 3.3).

In this experiment, the media was balanced by D-mannitol, which is expected to only contribute to the osmolarity without affecting the metabolism [89], so that all cells are

subject to the same level of total osmolarity regardless of the final glucose concentration. The preservation of glucose concentration-dependent toxicity (Figure 3.3) with the addition of osmolarity control rules out the possibility that the beta-cell glucotoxicity is simply caused by hyperosmolarity.

In addition to monitoring confluence, we tracked the dynamics of cell death in select wells of the same plate by adding a cytotoxicity dye that fluorescently labels cells with disrupted membrane integrity. Data from the dye-added samples were analyzed by dividing the total area with above-threshold green signal from a field of view by its confluence at each time point (Figure 3.4). Staurosporine-containing wells showed rapid increase in the confluence-normalized fluorescent area, as expected from an apoptosis-inducer. Similarly, zero glucose condition resulted in accumulation of dead cells over time. Cells grown in 1 mM glucose had the smallest increase in cell death, while higher glucose concentrations led to more cell death. The result indicates that higher cell death contributes to the overall slower proliferation of beta-TC-6 cells in high levels of glucose (Figure 3.3).

3.3.2 Local effect of cycling high glucose and optimal glucose on beta-TC-6 cell growth

Next, we investigated the effect of cycling high dose (15, 50, and 100 mM) and low, optimal dose (1 mM) of glucose as opposed to subjecting cells to a constant glucose level. Media in each well of beta-TC-6 cells was replaced every 12 hours to yield either high-low-high-low (HLHL) or low-high-low-high (LHLH) sequence of glucose exposure for 48 hours, along with the low-low-low-low (LLLL) and high-high-high-high (HHHH) conditions for comparison, in which the media were replaced every 12 hours with the fresh media containing the same amount of glucose (Figure 3.5A). All conditions were balanced by mannitol for osmolarity control. Cell growth was monitored by Incucyte live-cell imaging throughout the experiment (Figure 3.5B, examples of raw data are shown in Figure 3.8). In each time window, cells

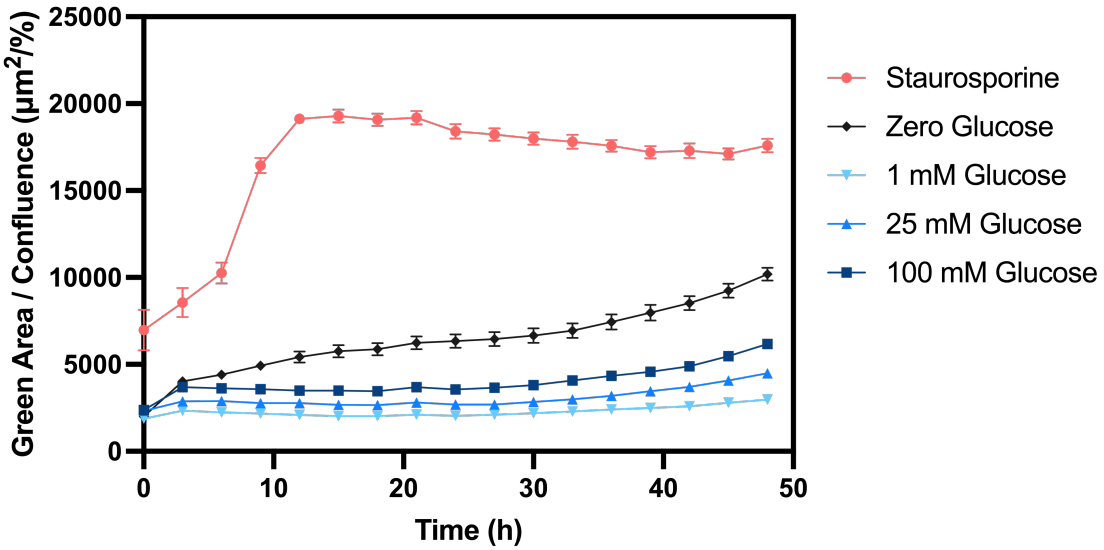

Figure 3.4: More beta-TC-6 cell death occurs when grown in high concentrations of glucose. The total osmolarity change in different glucose concentrations was controlled to be the same by balancing with D-mannitol. Mean values of total area (μm^2) of fluorescence from the added cytotoxicity dye divided by confluence (%) are plotted. Error bars show the SEM (n=15-23). Some error bars are not visible because they are smaller than the symbol size. Staurosporine was used as a positive control.

that were being subject to a low concentration of glucose at the moment had better growth than cells in the high-glucose phase. The result suggests that at any given time, the current glucose concentration likely determines the growth rate of beta-TC-6 cells.

After two cycles of growing cells in alternating or constant levels of glucose (a 48-hour schedule), cells in all wells were released to the optimal 1 mM glucose condition (Figure 3.5A) in order to test whether there is any lasting effect of previous different glucose feeding. It does not appear that there is a significant, systematic memory effect (Figure 3.9). However, in the first 12-hour window of the constant 1 mM glucose phase (Figure 3.9, left), cells that were switched from the high glucose to low glucose appear to grow better than cells that were already in low glucose. Interestingly, even the cells that were subject to HHHH 100 mM, the most glucotoxic condition tested, recover normal growth after being released into the optimal glucose condition.

A

	0	12	24	36	48	60	72
	12h	12h	12h	12h	12h	12h	
HHHH	15, 50, 100	15, 50, 100	15, 50, 100	15, 50, 100	1		
HLHL	15, 50, 100	1	15, 50, 100	1	1		
LHLH	1	15, 50, 100	1	15, 50, 100	1		
LLLL	1	1	1	1	1		
Zero Glu	0				1		

B

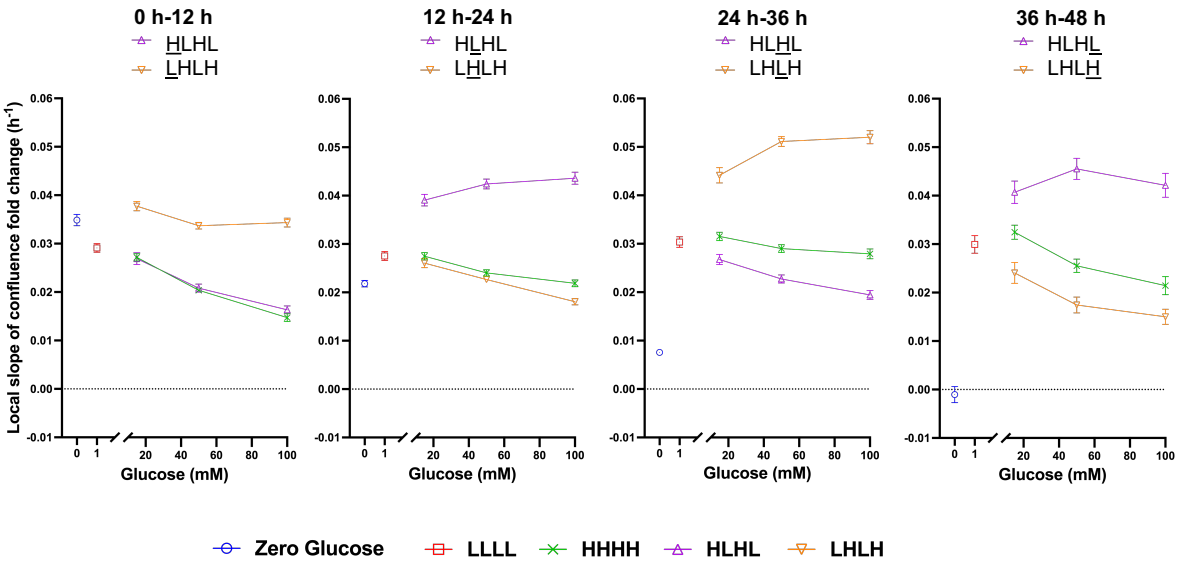

Figure 3.5: Instantaneous beta-TC-6 cell growth is most affected by the present glucose concentration in cycling glucose condition. (A) Experimental design for the cycling glucose experiment. (B) Mean local slope values of the confluence trajectories within each 12-hour window normalized by the first time point of the window. Error bars show the SEM (n=20-45). Some error bars are not visible because they are smaller than the symbol size.

3.3.3 Overall effect of cycling high glucose and optimal glucose on beta-TC-6 cell growth

We compared each glucose condition's sum of four 12-hour window local slopes throughout the 48-hour experiment to assess the cumulative effect of each cycling or constant glucose condition (Figure 3.6). Beta-TC-6 cells had the best overall growth in cycling conditions (HLHL and LHLH) compared to the constantly high condition (HHHH), and interestingly, even compared to LLLL condition. This result suggests that cycling glucose could be beneficial for beta cell survival.

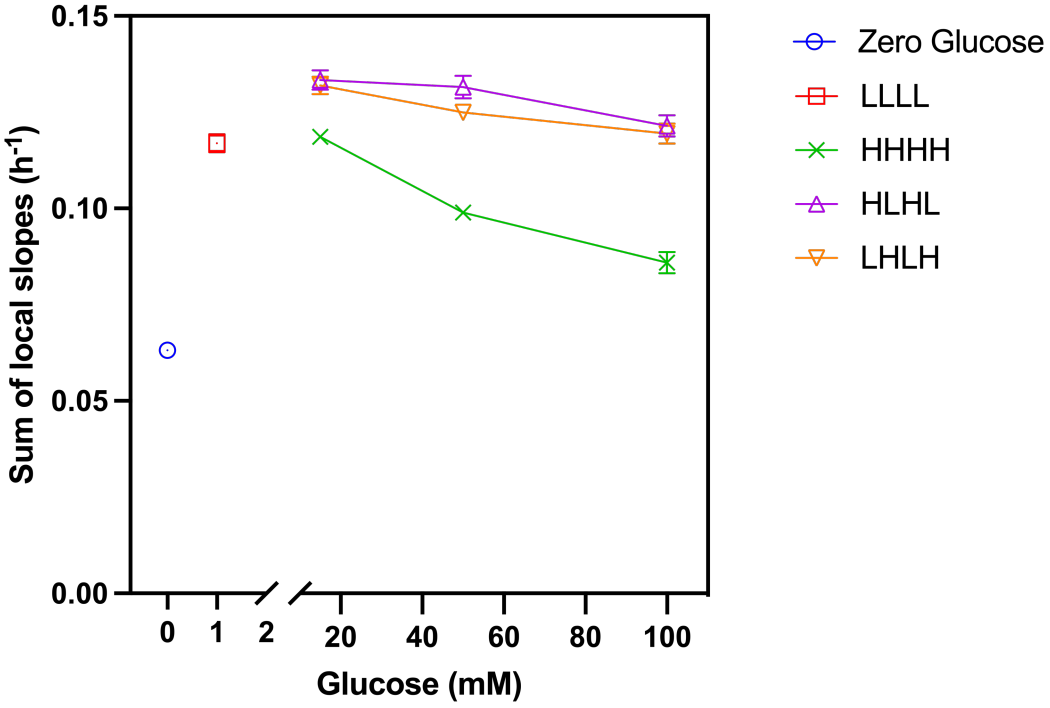

Figure 3.6: Beta-TC-6 cells grew better in cycling glucose conditions compared to constant glucose conditions. The averaged sums of four 12-hour window local slopes from individual fields of view are plotted. Error bars show the SEM (n=20-45). Some error bars are not visible because they are smaller than the symbol size.

3.3.4 The effect of balancing with mannose

In addition to D-mannitol, we also performed an experiment using mannose to balance glucose to get information on how glucose-specific the glucotoxicity effect is. A similar relative growth impairment was observed with higher-than-optimal concentrations of glucose as in the mannitol-balanced experiment (Figure 3.7). Interestingly, lower-than-optimal concentrations of glucose, which suffered severe growth impairment in mannitol-balanced experiment, supported cell growth comparable to optimal glucose concentration. This result suggests that mannose can partially replace glucose and relieve the stress caused by hypoglycemia. The molar concentrations of mannose in these conditions with no or low glucose are the same as the molar concentrations of glucose that elicits toxicity (around 30 mM), but no cell growth impairment is observed.

3.4 Materials and methods

3.4.1 Cell culture

A vial of β-TC-6 cells at passage 11 was provided by Joseph Bass lab (Northwestern University) as a gift. The cells were continuously grown in complete media containing 84% No-glucose DMEM (Gibco, 11966-025), 15% Heat Inactivated Fetal Bovine Serum (Gibco, 10438-026), 1% Penicillin Streptomycin (Gibco, 15140-122), and 1 mM Glucose (Gibco, A2494001). Media was replaced every 3-4 days, and cells were passaged when confluence was over 50-80%. All experiments shown here were performed with cells that were at up to passage 39.

3.4.2 Preparation of the beta-TC-6 cells in microplates

Beta-TC-6 cells were diluted to either 100000 cells/ml (800 µl per well) or 200000 cells/ml (100 µl per well) to seed a 24-well plate (Falcon, 353047) or a 96-well plate (Falcon, 353072),

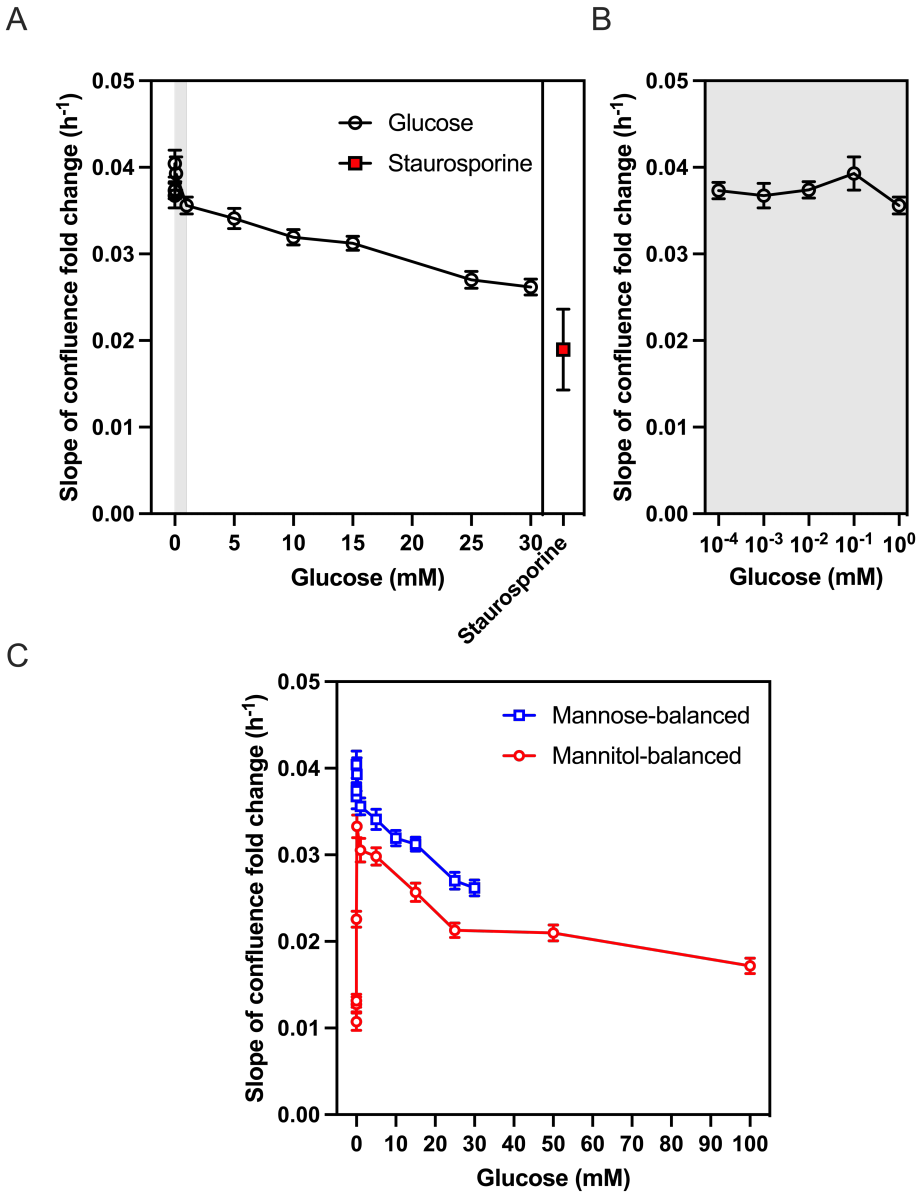

Figure 3.7: Mannose rescues beta-TC-6 cell growth impairment in hypoglycemic condition. Cells were grown in different concentrations of glucose balanced by mannose, so that the total concentration of added sugar molecules, as well as the resulting osmolarity change, is constant in all conditions. (A) Mean slope values of the confluence trajectories during the exposure to a given glucose concentration normalized by t=0 value. Error bars show the SEM (n=27-32). Staurosporine was used as a positive control. (B) The data for glucose concentrations from 0.1 µM to 1 mM, marked by the gray shade in (A), were re-plotted in logarithmic x-axis for better visibility. (C) Plot in (A) overlaid with the plot shown in Figure 3.3, which show slope values from the mannitol-balanced glucose experiments.

respectively. Cells were grown in the microplate for 2-4 days before beginning the glucotoxicity experiments using the complete medium containing 15% FBS.

3.4.3 Glucotoxicity experiment

Preparation of mannitol

Mannitol was used as an osmolarity control in glucotoxicity experiments unless otherwise stated. To match the molar concentration of glucose solution, 1110.15 mM of D-mannitol stock solution was prepared by dissolving mannitol (Sigma-Aldrich, M4125) in water, which was facilitated by incubation at 37 °C and vortexing, followed by filter-sterilization. Mannitol and glucose stock solutions, both at 1110.15 mM, were mixed in different ratios. 100% glucose was used for the highest concentration of glucose tested in this chapter (100 mM), and 100% mannitol was used for 0 glucose condition. For other concentrations of glucose, the stocks were mixed to yield the target final glucose concentration. (For instance, the mixture for 50 mM glucose condition was prepared to contain 50% glucose and 50% mannitol.)

Preparation of mannose

For some experiments, mannose was used to balance glucose added to the media. D-(+)-Mannose (Sigma, M6020) was dissolved in sterile water to the stock concentration of 277.5 mM. To match the mannose stock concentration, glucose was diluted to 277.5 mM. Two stock solutions were mixed in different ratios in the same way glucose + mannitol solutions were prepared. Glucose concentrations of up to 30 mM were tested, because higher than 30 mM glucose will require higher than 10% dilution of media in each well.

Setting up the glucotoxicity experiment

Using Venieratos et al. [88] as reference, glucotoxicity experiments were performed in serum-less media where 15% FBS was replaced with 0.25% Bovine Serum Albumin (GoldBio, A-421). Before the glucose treatment, the cells seeded on the microplate were washed with DMEM to ensure removal of serum. DMEM was then replaced with BSA-supplmented DMEM (909.9 µl when using a 24-well plate). Corresponding glucose + mannitol solution was gently added (90.9 µl for the 24-well plate) on top of the media of each well. The plate was gently shaken for mixing.

Media was exchanged in the middle of Incucyte imaging for some experiments using pre-warmed media at 37 °C. Media exchange was done one-well-at-a-time using a 1000 µl pipette for a 24-well plate. The withdrawal of media was conducted by slightly tilting the plate towards the pipette and placing the pipette tip at the bottom edge of the well to avoid touching areas that would be imaged. New media was added slowly from a pipette tip touching the wall of the well to ensure a gentle flow such that cell loss due to detachment was minimized.

For cell death monitoring, Incucyte Cytotox Green Dye (Sartorius, 4633) was used. For the experiment shown in Figures 3.3 and 3.4 performed using a 24-well plate, 1 µl of the 100 µM dye solution was added to one well each of Staurosporine, Zero Glucose, 1 mM Glucose, 25 mM Glucose, and 100 mM Glucose conditions, on top of the media.

3.4.4 Time-course imaging of cells using Incucyte

IncuCyte S3 (Sartorius/Essen BioScience) system in the University of Chicago's Cellular Screening Center was used to monitor growth of beta-TC-6 cells in the microplates. Phase contrast images were taken every 2-3 hours from multiple fields of view per well using a 10x objective. Green fluorescence images (Excitation: 441–481 nm; Emission: 503–544 nm) were also obtained for some experiments that involve cell death monitoring in addition to

confluence monitoring. When imaging cells on a 24-well plate, 25 images from different fields of view (a 5 x 5 grid) were obtained per well.

3.4.5 Analysis of Incucyte data

Image data extraction using Incucyte Base Software

IncuCyte Base Software 2021A was used to analyze the raw images. The default parameters were used except for the following changes:

Phase Segmentation Adjustment: 0.2

Phase Minimum Area filter: 160 μm^2

Green Minimum Area filter: 100 μm^2

Green Mean Intensity filter: 40

Because beta-TC-6 cells grow on top of one another, it was difficult to estimate the number of cells manually or utilizing the cell counting function of the Incucyte software. Therefore, the confluence (%) was used as a proxy for the degree of cell proliferation in an image. Similarly, the area (μm^2) of green fluorescent objects detected was used in subsequent analysis.

Data normalization and linear regression using a custom Matlab code

Raw data for each image extracted from Incucyte software were analyzed using Matlab. First, images that either have very low or very high confluence in the beginning of the experiment were excluded from analysis. The cut-offs were chosen so that only extreme outliers were rejected. Next, the time-course confluence trajectory of each image was normalized by its initial value. Finally, the normalized data were fit by linear regression and the resulting slope values were used as a proxy for the degree of proliferation during the time window of the data used for fitting.

3.5 Discussion

This study was mainly motivated by the following questions: does rhythmic glucose feeding improve beta cell proliferation *in vitro* as observed in *in vivo* studies? How does rhythmic glucose feeding affect the pancreatic circadian clock?

Our preliminary results only explored the first question. For our first attempts, we decided to test beta-TC-6 cells, which can be continuously cultured and therefore easier to handle. There is always a concern when using an immortalized cell line that the cellular mechanisms might be significantly altered compared to when using primary cells. However, the glucotoxic effects from both low and high concentrations of glucose previously observed in primary cells were reproduced in our experiments using beta-TC-6 cells (Figure 3.3). Our results show that the glucotoxic effect does not stem from changes in osmolarity, as the effect was present in experiments in which the total osmolarity in every condition was made equal by adding mannitol. Toxicity from glucose deficiency can be partially rescued by mannose, but such "over-dose" of mannose did not lead to any impairment in beta-TC-6 cell proliferation (Figure 3.7). Although preliminary, this result suggests that the observed beta cell toxicity could be specifically heightened by glucose over-dose, rather than being a general outcome of all sugars.

The cycling of glucose in the media appears to allow beta cells to proliferate better compared to the constant glucose conditions (Figure 3.6). In general, beta-TC-6 cell growth at a given time seems to be affected the most by the current glucose level (Figure 3.5). When two cultures are both in the same low, optimal concentration of glucose, the cells that recently transitioned from a higher concentration appear to have a slight growth advantage (Figures 3.5 and 3.9). Furthermore, it can be inferred that a larger fall of the glucose concentration (i.e. returning to 1 mM glucose from 50 mM or 100 mM rather than from 15 mM) gives more growth boost, considering the positive slopes of the HLHL and LHLH curves in their respective "L" windows in Figures 3.5 and 3.9.

Because many animals likely restrict their feeding activity to a particular time window of the day, it is possible that the pancreatic beta cells were evolved to expect, accommodate, or even depend on the rhythmic glucose levels. If so, the reported metabolic health benefits of the time-restricted feeding approach [29] could be partially explained by the improved glucose rhythms, which in turn would help with the beta cell survival and function. It is also plausible that the pancreatic beta cell clock, which is an important regulator of the beta cell function [83, 84], has evolved to interface with the daily rhythms of glucose. Future studies in which the clock rhythms are monitored from cells while subjecting them to controlled glucose rhythms will be able to generate insight on whether and how the beta cell clock and the glucose rhythms are linked.

It is also curious why beta cell glucotoxicity was not "eliminated" by evolution, considering that it gives vulnerability to animals that experience hyperglycemia by causing metabolic diseases. One hypothesis is that glucotoxicity provides the ability to selectively kill off mutant beta cells that mis-sense the glucose level to be significantly higher than the actual value, if such mutants arise in the system [90]. Similarly, the possibility of the circadian mismatch serving as a marker for a problematic cell can be speculated.

3.6 Supporting information

3.6.1 Supplementary figures

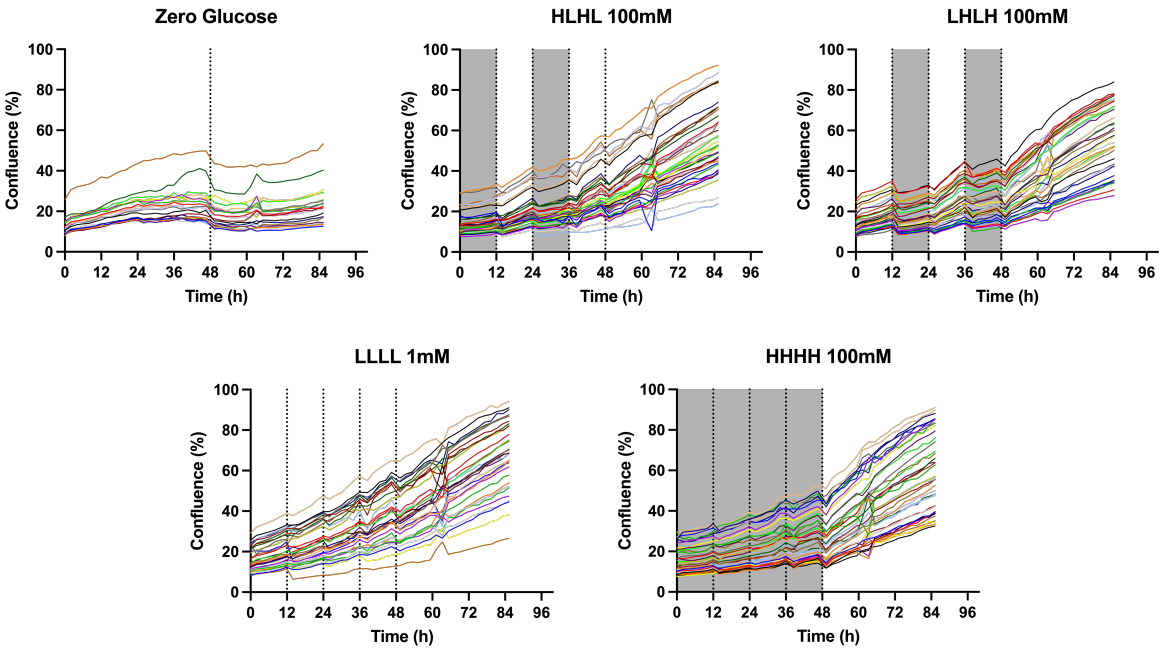

Figure 3.8: Example raw trajectories of beta-TC-6 in cycling or constant glucose. Data shown here were processed to generate Figure 3.6. Shaded regions indicate duration cells were exposed to high glucose. Vertical dotted lines indicate media exchange events. Unshaded regions indicate low, optimal glucose (1 mM) except for the Zero Glucose plot in which the glucose concentration changes from zero to 1 mM at t = 48 h.

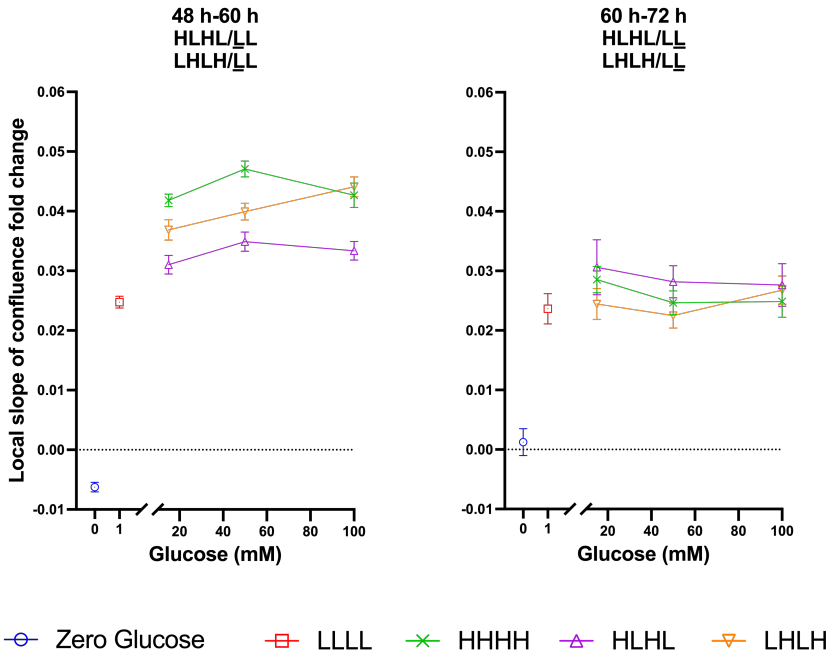

Figure 3.9: Beta-TC-6 cell growth in optimal glucose concentration after the termination of 48-hour cycling or non-cycling glucose feeding. Mean local slope values of the confluence trajectories within each 12-hour window normalized by the first time point of the window. Error bars show the SEM (n=20-45).

3.7 Conclusions and future directions

In this chapter, I report preliminary data on how different concentrations of glucose and the rhythmicity of glucose exposure on beta-TC-6 cells. In summary, I first show the reverse-V-shaped dependence of cell growth on the glucose concentration in constant glucose condition (Figure 3.3), reminiscent of the V-shaped correlation of the degree of beta cell death reported previously [79]. Next, I show that the overall glucotoxicity experienced by the cells can be alleviated by alternating high glucose and low glucose every 12 hours rather than subjecting cells to a constant level of glucose, especially constant high glucose (Figure 3.7). Based on our results, we propose that beta-TC-6 cell culture system can be used as an alternative to animal-derived primary cell or islet systems to explore questions related to beta cell glucotoxicity and Type 2 Diabetes pathology.

While still preliminary, these results resonate with the expectation that imposing circa-

dian rhythmicity on glucose input can be beneficial for beta cells, given the importance of the circadian clock in their normal function [84]. Many important questions still remain. For instance, it is unclear whether the 24-hour period glucose rhythmicity was particularly effective, because alternating glucose in different time intervals was not tested yet. It is also curious whether the result will depend on the synchronized clock phase of the cells; it is possible that the alignment of the glucose input rhythm and the beta cells' internal circadian rhythm is an important factor in the beta cell proliferation. In the preliminary experiments reported in this chapter, the beta-TC-6 cells were not entrained in any intentional way, and the question above was not explored.

Further, elucidating the mechanism behind the glucose concentration-dependent beta cell growth will greatly enhance our understanding. Experiments such as RNA sequencing to detect gene expression changes in different glucose conditions could allow us to identify specific pathways that ultimately lead to the differences in the beta cell proliferation.

CHAPTER 4

CONCLUDING REMARKS

My dissertation research was aimed at expanding our knowledge on the interplay between circadian clocks and the cellular systems they regulate. In chapter 2, I report our discovery and investigation of KidA, a cyanobacterial clock interactor that was previously uncharacterized. We found that KidA shortens the period of the cyanobacterial clock both *in vivo* and *in vitro* in a dose-dependent manner. Direct binding of KidA to KaiB appears to underlie this effect, which occurs through its predicted N-terminal PAS domains. KidA specifically binds to fold-switched form of KaiB, a property which we show is sufficient to give rise to period tuning using a computational modeling approach.

Our findings shed light on the interface between KidA and the circadian clock. However, there still are remaining questions about KidA, which has the potential to have different roles in regulating the physiology. KidA's roles in other cellular systems, potentially involving a relay of the clock state information, still remain unknown. Containing multiple PAS domains, which play versatile roles as sensor domains in a variety of proteins across all kingdoms of life, or PAS-like domains, KidA could be able to respond to different environmental signals as well as the clock state. Through the diguanylate cyclase or the phosphodiesterase activities, KidA could also participate in cyclic-di-GMP mediated signaling. In particular, there is a possibility that KidA could be involved in biofilm formation, which is regulated by cyclic-di-GMP in many other species. Some preliminary observations of the KidA overexpression culture that suggests potential biofilm-like structure formation are attached in Appendix A. In Appendix B, additional supplementary information and data that were not included in Chapter 2 or the published article [35] are shown.

In chapter 3, I explored the hypothesis that rhythmic feeding of glucose over a 24-hour period could improve pancreatic beta cell survival. This question was inspired by the reports that time-restricted feeding appears to provide health benefits to animals [29]. The effect

of subjecting cells to rhythmic glucose *in vitro*, which is analogous to the time-restricted feeding *in vivo*, was studied using beta-TC-6 cell line. Our preliminary result suggests that cycling glucose, as opposed to maintaining constant glucose, could be beneficial for the beta-TC-6 cell proliferation as expected. We show that the glucotoxicity from high glucose can be mitigated by alternating high glucose and low glucose. Beta cell health is of importance because it plays an essential function in maintaining glucose homeostasis and its failure is linked to Type 2 Diabetes. Future studies that unveil the interplay of the beta cell circadian clock, the rhythmicity glucose input, and the pathogenesis of beta cell failure will contribute valuable and insightful information.

APPENDIX A

UNPUBLISHED FOLLOW UP RESULTS FOR KIDA

Unpublished preliminary data on KidA are attached in this appendix. In the first section, I report unexpected differences observed between the KidA overexpression strain and the WT strain in the way the cells settle at the bottom of a container, which suggests potential involvement of KidA in a biofilm-like phenotype. In the second section, I attach results of a fluorescence polarization experiment that was performed with the objective to characterize the binding of KidA and KaiB. The intended information could not be inferred from the experiment, but these results might inform further investigation on additional unknown factors of KidA interaction with the Kai proteins. In the third section, preliminary results from KidA-KaiC co-IP/Western blot are shown, which suggests potential rhythmic *in vivo* interaction of KidA with Kai proteins throughout the day.

A.1 Settled culture appearance of the KidA-overexpression strain

A.1.1 The unique appearance of settled culture of KidA-overexpression strain in a glass tube

5 ml cultures of KidA-overexpression strain (KidA-OX/2195) and the wild type reporter strain (WT/2195) were grown in glass tubes in a Percival incubator under constant light with shaking to a high density ($OD_{750} > 1$) as a part of routine culture maintenance. Different amounts of IPTG were added to KidA-OX cultures to the final concentration of 0, 1 mM, and 5 mM. Afterwards, the cultures were left on a lab bench undisturbed. Interestingly, the KidA-OX cells gradually developed a different appearance compared to the wildtype in the way they settled at the bottom of the glass tubes. The bottom view of the glass tubes containing the settled cultures was taken with an iPhone (Figure A.1). Most of the WT cells occupied a small circular area at the center, which appears as a dark-colored, large dot as

a result. On the contrary, KidA-OX cells formed an apparent circular "void" in the center, which was more distinct in IPTG-induced conditions compared to the 0 IPTG condition.

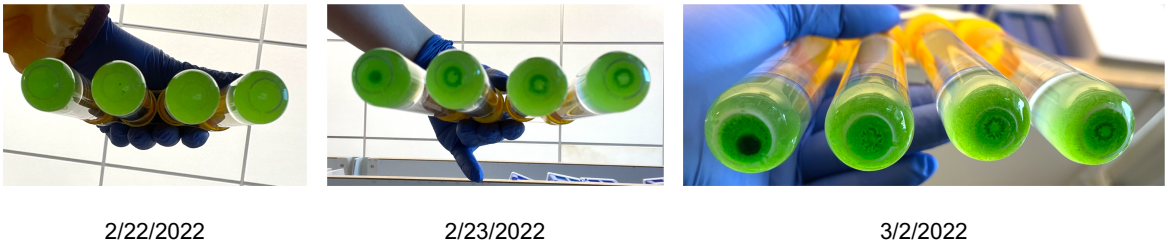

Figure A.1: Appearance of KidA-OX culture settlement at the bottom of the glass tube. In each photograph, WT reporter strain, KidA-OX strain without added IPTG, KidA-OX strain induced with 1 mM IPTG, and KidA-OX strain induced with 5 mM IPTG are shown from left to right.

Incidentally, the stationary KidA culture that settled down at the bottom sometimes developed a blobby structure that can float in the media after gentle agitation. Examples of such occurrences are shown in Figure A.3. However, the exact condition that deterministically leads to the blob formation remains unknown. So far, there were incidents of this structure forming with or without IPTG.

A.1.2 The unique appearance of settled culture of KidA-overexpression strain in a 24-well microplate

The above observation is expected to be influenced by the rounded bottoms of the glass tubes. To test the effect of a flat bottom container, a similar experiment was done using a flat bottom well microplate. KidA-OX/2195 (KidA overexpression strain in the luciferase reporter background) and WT/2195 (WT luciferase reporter strain) cultures were grown in BG-11 to a high OD ($OD_{750} > 1$) and transferred to different wells in a TC-treated polystyrene 24-well plate (Falcon, 353047), 2 mL per well. 1 mM IPTG was added to some wells, leaving the rest of the wells without IPTG. With the lid on, the plate was left on the

bench for 17 days and was checked for visible difference in appearance. There was a distinct appearance of the KidA-OX settlement compared to the WT but of a different nature than in the rounded bottoms of the glass tubes (Figure A.2). WT cells showed similar settling pattern as in the glass tube experiment, forming a dense circular area in the middle. KidA-OX cells, on the other hand, spread out filling up the bottom surface of the well surface and did so only when induced with IPTG. Uninduced KidA-OX cells settled in a similar manner as the WT.

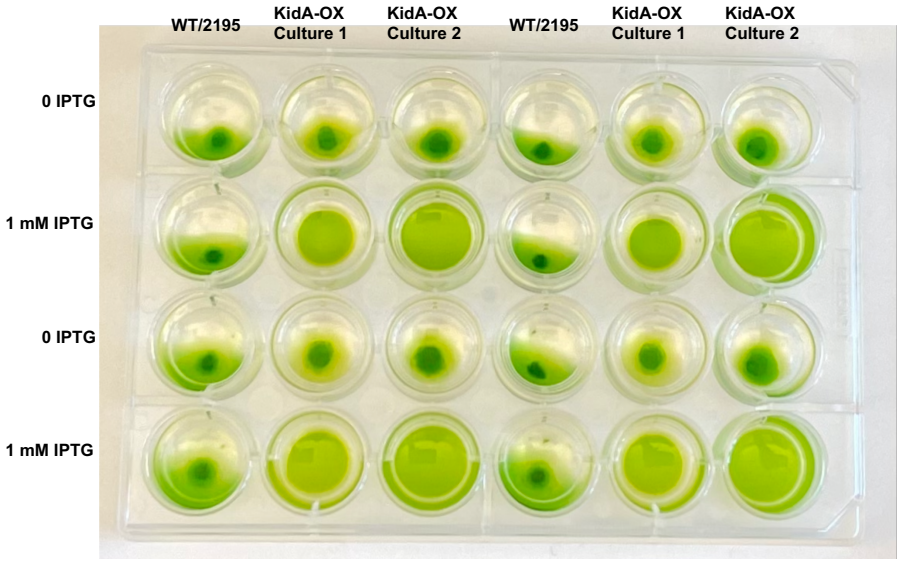

Figure A.2: Appearance of KidA-OX culture settlement at the bottom of the flat bottom wells in a microplate.

Figure A.3: Incidents of KidA-OX culture developing a blobby structure

A.1.3 Discussion and future directions

In typical lab growth conditions, involving shaking in the incubator, the KidA-OX cultures showed no apparent difference in their appearance compared to the wild type. However, it appears that KidA-OX cultures have distinct physiology in stationary condition given the reported observations (Figure A.1, A.2, A.3). Considering that KidA has the potential to regulate the cyclic-di-GMP level through its diguanylate cyclase or phosphodiesterase domain, we hypothesize that the phenotypes we observed are likely related to biofilms, the regulation of which is mediated by cyclic-di-GMP in many organisms [91]. It is unclear if the KidA-OX strain could be forming a canonical biofilm. In fact, while cyanobacterial species often form biofilms in their natural habitat, the S. elongatus PCC 7942 lab strain exhibit planktonic lifestyle under standard lab condition due to a self-suppression mechanism [92]. Further research is needed to understand the formation of these biofilm-like structures by KidA-OX cells and other kinds of physiological processes that KidA might be involved in.

The assays used in Figures A.1 and A.2 need to be improved, as little to no optimization was done so far. The wait time for the fully suspended cells to settle and develop phenotype and the range of the inducer (IPTG) concentrations still require optimization. A better way to collect data over time (photographs or videos) ideally including automation would be useful, as well as an approach that yields quantitative measurements of how much of the biofilm-like material was produced.

Many remaining questions can be studied using optimized versions of the above assays or using different methods. For example, which KidA domains are involved in the production of the biofilm-like structure? (Is the activity dependent on the GGDEF and/or the EAL domain as we hypothesized?) What do these structures consist of? (Do the components overlap with what composes extracellular matrices of other biofilm-forming bacteria?) Given that KidA interacts with the Kai proteins, is there any clock-dependence in the phenomenon? Does KidA-overexpression result in a fitness advantage or disadvantage in stationary conditions,

potentially via mechanism that involves this phenotype?

A.2 Fluorescence polarization of KidA+KaiB reaction

A.2.1 Results

To characterize the slow binding reaction of KidA and KaiB, we performed a fluorescence polarization assay using various concentrations of purified KidA PAS-ABC and ∼200 nM FITC-labeled KaiB. We expected that the FP values at saturation would monotonically increase with the increasing KidA PAS-ABC concentrations. However, an unexpected result was obtained in which ∼ 0.1 µM KidA PAS-ABC or less achieves a much higher FP value in a much shorter time compared to the higher concentrations of KidA PAS-ABC (Figure A.4). The bi or multi-phasic trend is clear when the final, seemingly equilibrated FP values for each condition are plotted against KidA PAS-ABC concentration (Figure A.5). It appears as if there are multiple binding modes with different fluorescent signatures.

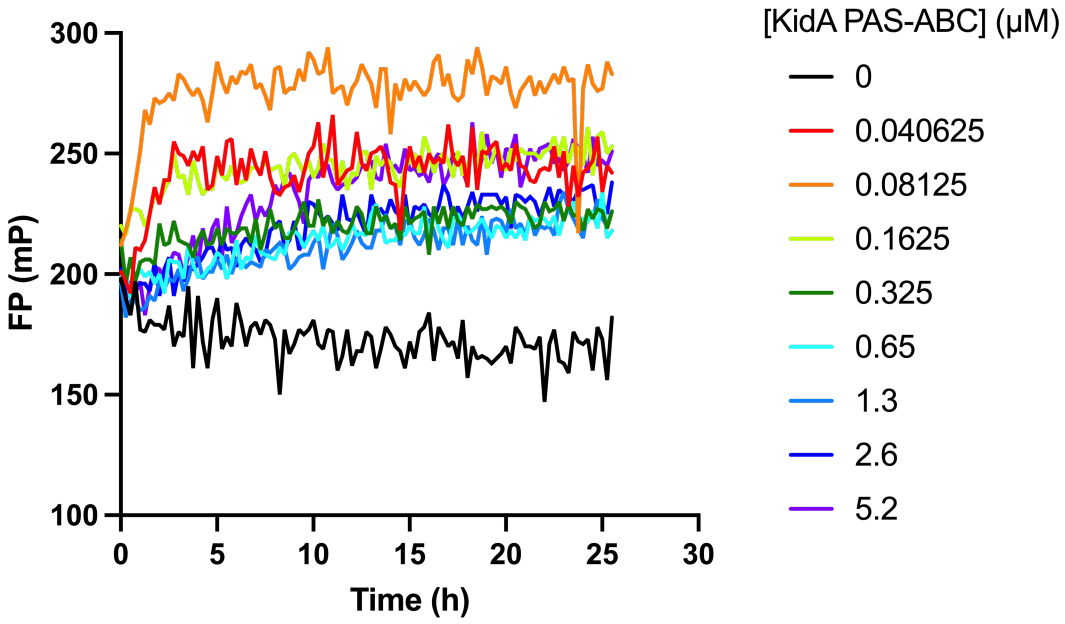

Figure A.4: FP signals from the KidA PAS-ABC + FITC-KaiB reaction. Data from one experiment was shown.

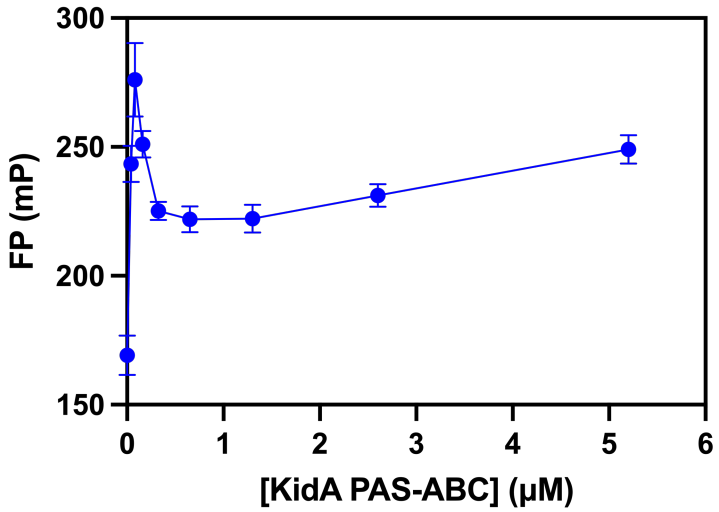

Figure A.5: Averaged FP values in the saturation regime. FP values from t=20 h to t=25h were averaged. Values from the experiment shown in Figure A.4 are plotted. Error bars show the standard deviation.

A.2.2 Discussion and future directions

Further investigation could elucidate the mechanism behind the unexpected FP result we obtained from KidA PAS-ABC and KaiB binding. It is possible that KidA PAS-ABC has different oligomerization states *in vitro* depending on its concentration. As such, characterizing the oligomeric states of KidA PAS-ABC using size-exclusion chromatography or other approaches can help us understand the apparent existence of multiple modes of KidA-KaiB binding. It is also possible that KaiB oligomerization is at play, which is known to exist in tetramer in its ground state and monomer in its fold-switched state [93, 11]. Additionally, the FP assay could be improved for better signal by using a higher concentration of FITC-KaiB.

A.3 In vivo interaction of KidA with KaiC throughout the day

We attempted an *in vivo* time-course co-IP experiment using the KidA-HA overexpression strain to characterize whether KidA rhythmically interacts with the Kai proteins throughout the day. The cells were grown, entrained, and released to constant light, harvested every 4 hours, lysed, and subjected to Anti-HA co-IP, using the same procedures described in Chapter 2. The resulting eluate samples were analyzed by Western blot.

Western blot detection for all three Kai proteins was attempted. However, potentially due to the differences in the effectiveness of Kai protein antibodies/antisera and the natural *in vivo* expression level of each Kai protein, only Anti-KaiC Western blot using a KaiC antiserum (O'Shea lab) resulted in detectable signal.

The amount of KidA-KaiC interaction at each time point was estimated by dividing the KaiC band intensity by the KidA-HA band intensity. The result of this preliminary experiment suggests that KidA's interaction with KaiC changes throughout the day, with more interaction occurring during subjective day compared to subjective night (Figure A.6).

We showed in Chapter 2 and in Kim et al. [35] that KidA binds to fold-switched KaiB, so we could hypothesize that KidA and KaiC interaction is indirect and is mediated by KaiB. Because our current understanding of the KaiB fold-switching is that it only occurs during the subjective night, KidA showing a higher interaction with KaiC during the subjective day than during the subjective night is unexpected. However, it is consistent with the initial fold-switched KaiB IP/MS experiment from which KidA was identified; the high overall signal intensity from KidA in Figure 2.1B was mostly contributed by its signal from the light (L) sample, although it would be inappropriate to interpret the physiological difference between the dark and light sample because the mutant KaiB locked in fold-switched fold is artificially overexpressed in the IP/MS experiment, regardless of the time of day. In the IP/WB(Western Blot) experiment shown here, the Kai proteins are in their natural state, but KidA-HA is overexpressed, which might or might not have a dominant effect that masks

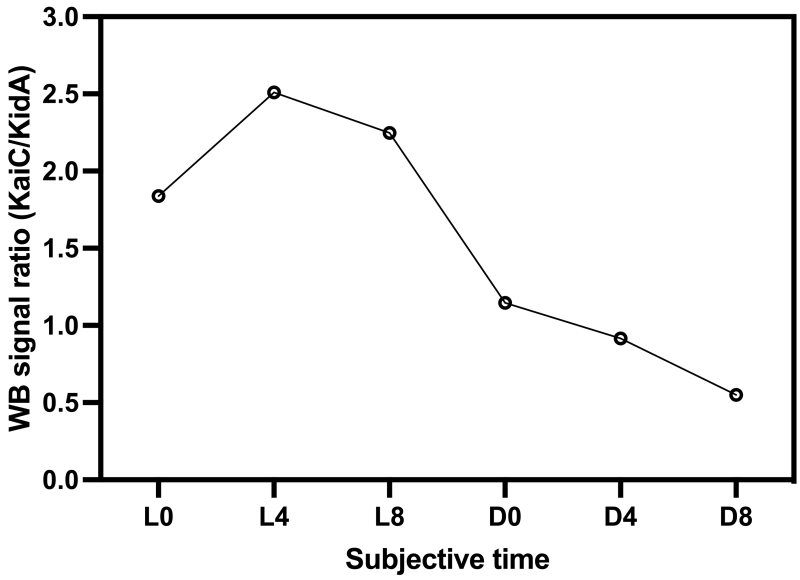

Figure A.6: The amount of KaiC pulled down by KidA *in vivo* changes throughout the day. The Western blot signal of KaiC divided by that of KidA-HA from the *in vivo* co-IP using KidA-HA as bait is shown at each time point. Cells were harvested during the constant light phase after entrainment, and the x-axis shows the subjective time of the day.

the true physiological interactions of KidA and Kai proteins *in vivo*.

Follow-up experiments, as well as repeats of the experiment shown here with more controls, need to be conducted in order to understand the full *in vivo* picture of the interaction between KidA and the Kai proteins. While preliminary, the KaiC-KidA co-IP/WB results suggest that there still are gaps in our understanding of how KidA and the Kai oscillator interface in the cell and possibly also in our knowledge of KaiB fold-switching in the cell. Further investigations will help shed light on this unexpected relationship among KidA, KaiC, KaiB fold-switching, and time.

APPENDIX B

APPENDIX TO CHAPTER 2

Additional information that supplement the results reported in Chapter 2 of this dissertation and Kim et al. [35] is attached in this appendix.

B.1 Predicted structures of KidA

In Chapter 2 and our published article [35], Phyre2 algorithm [45] was used to predict which domains are present in the N-terminal region of KidA based on the structural prediction. The included figure (Figure 2.5B) was generated using prediction results obtained around June 2020. To find out whether other structural prediction algorithms also produce similar results, we looked at the structure predicted by AlphaFold (Figures B.1, B.2) [94]. AlphaFold-predicted structure resulted in low model confidence in the PAS-A and PAS-B region and did not predict a PAS-like fold for the PAS-A region.

For additional confirmation, we submitted partial sequences of KidA as before for structural prediction using Phyre2 (April 2023) using intensive mode, as was previously done to generate Figure 2.5B. Compared to the output obtained in June 2020 using the same input, there were slight changes in the final predicted model and the first-ranked individual model for the PAS-ABC region, in which the PAS-B region was not predicted to fold into a PAS-like fold. However, the second-ranked individual model, which used a structure for PpsR from Rb. sphaeroides (PDB: 4HH2) [96] as template, predicted PAS-like folds for both PAS-A and PAS-B regions. These predicted 3D structures of PAS-A and PAS-B are shown in Figure B.3 along with PAS-C from the AlphaFold prediction and an example PAS domain structure of NifL protein [97] for reference.

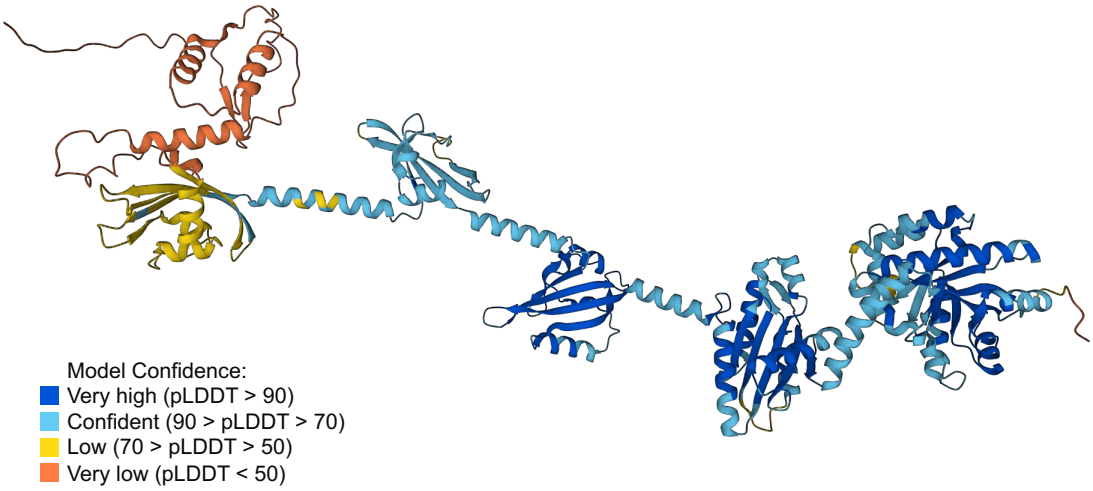

Figure B.1: AlphaFold predicted structure of full length KidA colored by confidence score. Structure deposited for Uniprot code Q31M30 was downloaded from the AlphaFold Protein Structure Database. The colors indicate AlphaFold-reported per-residue confidence score (pLDDT), which ranges from 0 to 100. [94, 95]

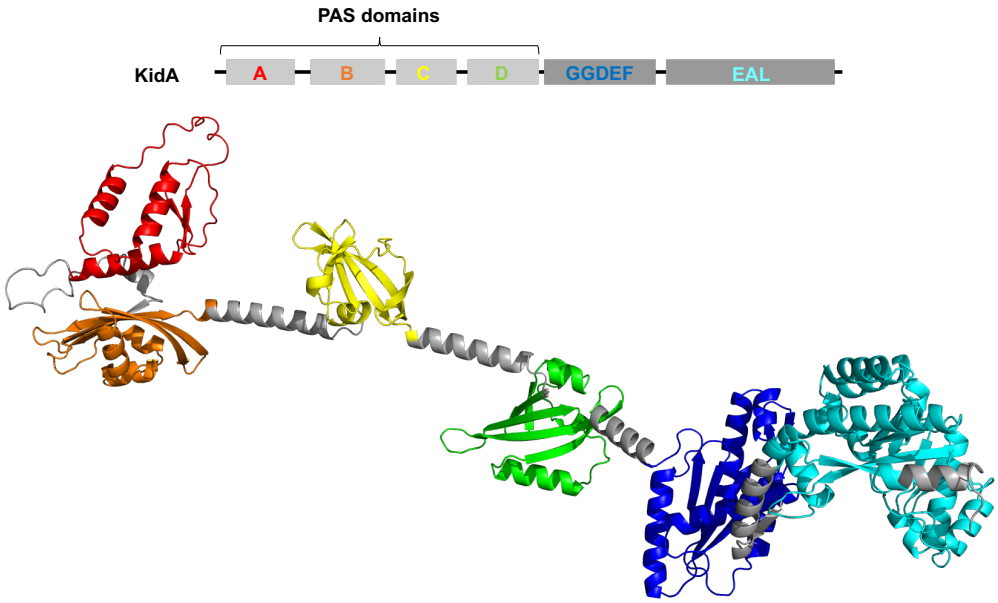

Figure B.2: AlphaFold predicted structure of full length KidA colored by domain assignment as in Figure 2.5

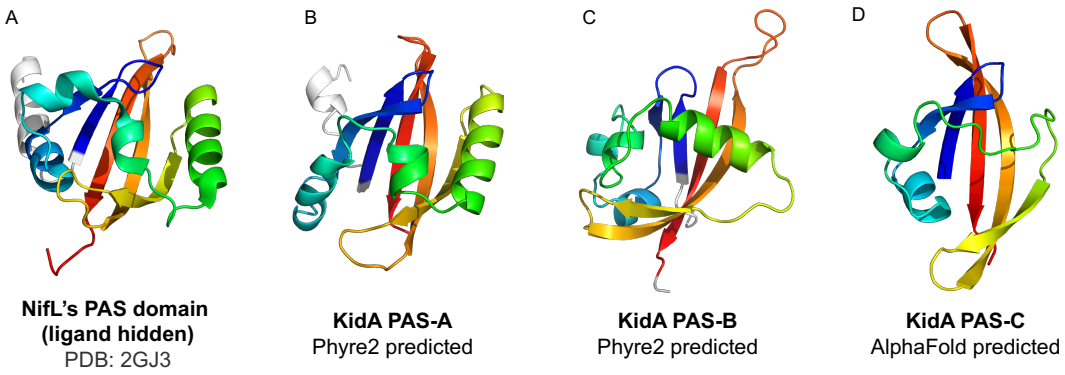

Figure B.3: Predicted 3D structures of individual domains of KidA with PAS-like folds. All structures are colored using the rainbow scheme in PyMOL [98], which is applied to the residues assigned to each PAS domain of KidA as defined in Figure 2.5 in Chapter 2. (A) An example of PAS domain for comparison with predicted structures of KidA's PAS-like domains. A flavin-binding PAS domain from *A. vinelandii* NifL protein [97] is shown. The crystal structure involves the FAD cofactor, which is hidden in this representation. (B-C) Structure of PAS-A region (B) or PAS-B region (C) of KidA predicted using Phyre2 in April 2023 using the KidA amino acid sequence from residue 1 to 359 (spanning PAS-A,B, and C) from the second rank model. *Rb. sphaeroides* PpsR structure (PDB: 4HH2) was used as template for this second rank model. (D) PAS-C region of KidA predicted by AlphaFold, which is the same as the yellow colored region in B.2.

B.2 Additional supplementary data that were not included in Chapter 2 or the published article

B.2.1 Including c-di-GMP in the in vitro clock reaction does not affect the period

Before we performed the domain truncation assay that led us to specify the domains of KidA that are necessary for the period shortening effect, we hypothesized that c-di-GMP might be involved in directly affecting the Kai proteins that leads to changes in the period, because KidA contains enzymatic domains (GGDEF and EAL) that can synthesize or degrade c-di-GMP. To that end, we investigated whether the addition of c-di-GMP (Sigma-Aldrich, SML1228) to the *in vitro* clock reaction containing the Kai proteins shows an effect on the clock rhythms. Consistent with our finding that the GGDEF and EAL domains of KidA are dispensable for the period shortening effect, the addition of c-di-GMP in the clock fluorescence polarization reaction did not show any effect on the period of the oscillation (Figure B.4). The FP reactions were prepared in the same way as in Chapter 2.

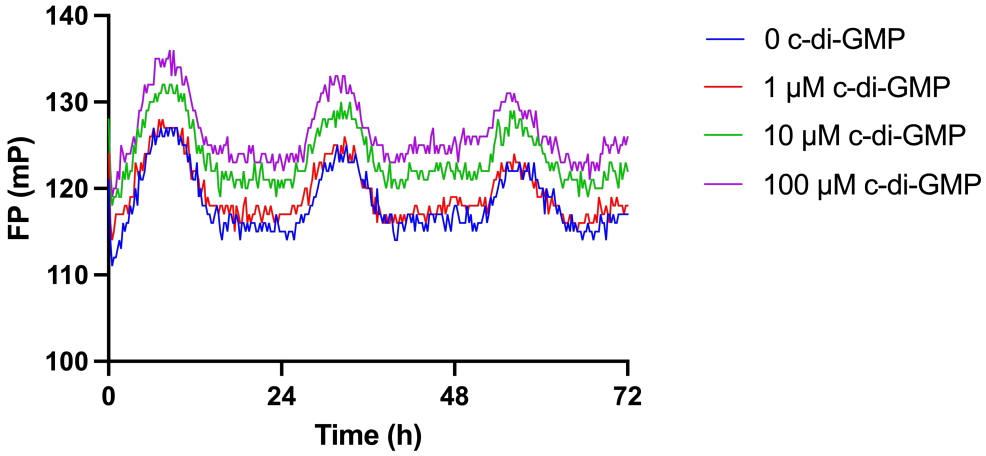

Figure B.4: c-di-GMP addition to the in vitro clock reaction. 0, 1 µM, 10 µM, or 100 µM c-di-GMP was included in the reaction buffer.

B.2.2 Overexpression of a diguanylate cyclase or a phosphodiesterase does not affect the in vivo clock period

To test the hypothesis that c-di-GMP might be involved in the clock period *in vivo*, we made cyanobacterial reporter strains that overexpress an exogenous diguanylate cyclase or phosphodiesterase known to have active enzymatic activity, which would induce significant changes in the intracellular levels of c-di-GMP. We made a strain that overexpresses Slr1143, a GGDEF-domain containing protein from *Synechocystis* sp. PCC 6803, shown to have an active diguanylate cyclase activity [99]. We also made a strain that overexpresses PdeH, an EAL-domain containing protein from *E. coli* with active phosphodiesterase activity [100]. An IPTG-inducible promoter was used in both strains for driving the expression of the added genes.

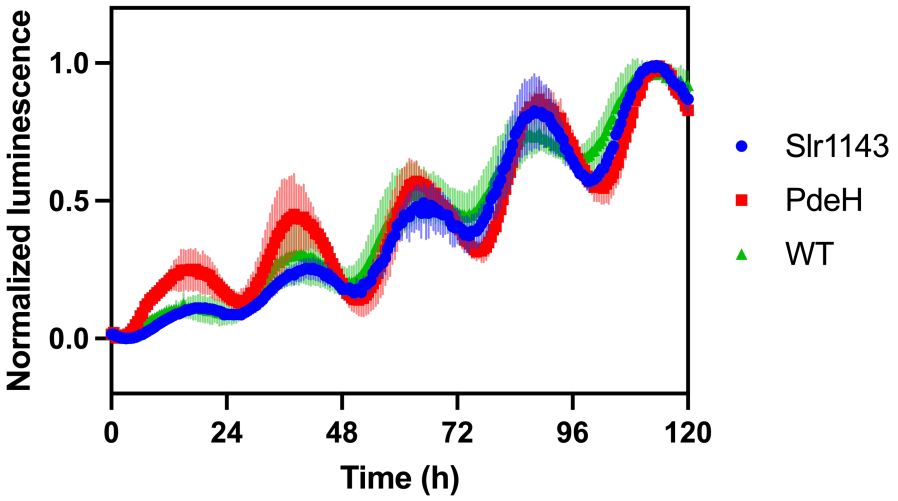

Figure B.5: Overexpression of a diguanylate cyclase and a phosphodiesterase does not affect the *in vivo* clock period. *In vivo* clock rhythms of the WT reporter strain, Slr1143 overexpression strain, and PdeH overexpression strain, while in constant light after a 12 h light-12 h dark cycle entrainment, were measured using TopCount. Mean values of the normalized luminescence traces are plotted, and the spread shows the standard deviation (n = 4-5).

Slr1143 and PdeH overexpression strains were characterized for their clock rhythms using the TopCount bioluminescence assay described in Chapter 2. Even when these proteins were

induced with 100 mM IPTG, the *in vivo* clock rhythms had the same period as the WT reporter (Figure B.5). The result is consistent with our finding that KidA's N-terminal PAS domains are involved in the period shortening phenotype and that the C-terminal GGDEF/EAL region is not.

REFERENCES

[1] Deborah Bell-Pedersen, Vincent M Cassone, David J Earnest, Susan S Golden, Paul E Hardin, Terry L Thomas, and Mark J Zoran. Circadian rhythms from multiple oscillators: lessons from diverse organisms. *Nature Reviews Genetics*, 6(7):544–556, 2005.

[2] Reena Saini, Mariusz Jaskolski, and Seth J Davis. Circadian oscillator proteins across the kingdoms of life: structural aspects. *BMC biology*, 17(1):1–39, 2019.

[3] Alina Patke, Michael W Young, and Sofia Axelrod. Molecular mechanisms and physiological importance of circadian rhythms. *Nature reviews Molecular cell biology*, 21(2):67–84, 2020.

[4] Jay C Dunlap, Jennifer J Loros, and Patricia J DeCoursey. *Chronobiology: biological timekeeping.* Sinauer Associates, 2004.

[5] Susan S Golden and Shannon R Canales. Cyanobacterial circadian clocks—timing is everything. *Nature Reviews Microbiology*, 1(3):191–199, 2003.

[6] Jennifer M Hurley, Jennifer J Loros, and Jay C Dunlap. Circadian oscillators: around the transcription–translation feedback loop and on to output. *Trends in biochemical sciences*, 41(10):834–846, 2016.

[7] Carl Hirschie Johnson and Michael Joseph Rust. *Circadian rhythms in bacteria and microbiomes*, volume 409. Springer, 2021.

[8] Masato Nakajima, Keiko Imai, Hiroshi Ito, Taeko Nishiwaki, Yoriko Murayama, Hideo Iwasaki, Tokitaka Oyama, and Takao Kondo. Reconstitution of circadian oscillation of cyanobacterial kaic phosphorylation in vitro. *science*, 308(5720):414–415, 2005.

[9] Jeffrey A Swan, Susan S Golden, Andy LiWang, and Carrie L Partch. Structure, function, and mechanism of the core circadian clock in cyanobacteria. *Journal of Biological Chemistry*, 293(14):5026–5034, 2018.

[10] Michael J Rust, Joseph S Markson, William S Lane, Daniel S Fisher, and Erin K O'Shea. Ordered phosphorylation governs oscillation of a three-protein circadian clock. *Science*, 318(5851):809–812, 2007.

[11] Yong-Gang Chang, Susan E Cohen, Connie Phong, William K Myers, Yong-Ick Kim, Roger Tseng, Jenny Lin, Li Zhang, Joseph S Boyd, Yvonne Lee, et al. A protein fold switch joins the circadian oscillator to clock output in cyanobacteria. *Science*, 349(6245):324–328, 2015.

[12] Joseph S Markson, Joseph R Piechura, Anna M Puszynska, and Erin K O'Shea. Circadian control of global gene expression by the cyanobacterial master regulator rpaa. *Cell*, 155(6):1396–1408, 2013.

[13] Hiroshi Ito, Michinori Mutsuda, Yoriko Murayama, Jun Tomita, Norimune Hosokawa, Kazuki Terauchi, Chieko Sugita, Mamoru Sugita, Takao Kondo, and Hideo Iwasaki. Cyanobacterial daily life with kai-based circadian and diurnal genome-wide transcriptional control in synechococcus elongatus. *Proceedings of the National Academy of Sciences*, 106(33):14168–14173, 2009.

[14] Andrian Gutu and Erin K O'Shea. Two antagonistic clock-regulated histidine kinases time the activation of circadian gene expression. *Molecular cell*, 50(2):288–294, 2013.

[15] Michael J Rust, Susan S Golden, and Erin K O'Shea. Light-driven changes in energy metabolism directly entrain the cyanobacterial circadian oscillator. *science*, 331(6014):220–223, 2011.

[16] Yong-Ick Kim, David J Vinyard, Gennady M Ananyev, G Charles Dismukes, and Susan S Golden. Oxidized quinones signal onset of darkness directly to the cyanobacterial circadian oscillator. *Proceedings of the National Academy of Sciences*, 109(44):17765–17769, 2012.

[17] Amandine Verlande and Selma Masri. Circadian clocks and cancer: timekeeping governs cellular metabolism. *Trends in Endocrinology & Metabolism*, 30(7):445–458, 2019.

[18] Gopal K Pattanayak, Connie Phong, and Michael J Rust. Rhythms in energy storage control the ability of the cyanobacterial circadian clock to reset. *Current Biology*, 24(16):1934–1938, 2014.

[19] Yi Liao and Michael J Rust. The circadian clock ensures successful dna replication in cyanobacteria. *Proceedings of the National Academy of Sciences*, 118(20):e2022516118, 2021.

[20] Arnaud Taton, Christian Erikson, Yiling Yang, Benjamin E Rubin, Scott A Rifkin, James W Golden, and Susan S Golden. The circadian clock and darkness control natural competence in cyanobacteria. *Nature communications*, 11(1):1688, 2020.

[21] Gopal K Pattanayak, Yi Liao, Edward WJ Wallace, Bogdan Budnik, D Allan Drummond, and Michael J Rust. Daily cycles of reversible protein condensation in cyanobacteria. *Cell reports*, 32(7):108032, 2020.

[22] Kenya Tanaka, Ginga Shimakawa, and Shuji Nakanishi. Time-of-day-dependent responses of cyanobacterial cellular viability against oxidative stress. *Scientific Reports*, 10(1):20029, 2020.

[23] Guogang Dong, Qiong Yang, Qiang Wang, Yong-Ick Kim, Thammajun L Wood, Katherine W Osteryoung, Alexander van Oudenaarden, and Susan S Golden. Elevated atpase activity of kaic applies a circadian checkpoint on cell division in synechococcus elongatus. *Cell*, 140(4):529–539, 2010.

[24] Koji Kawasaki and Hideo Iwasaki. Involvement of glycogen metabolism in circadian control of uv resistance in cyanobacteria. *PLoS Genetics*, 16(11):e1009230, 2020.

[25] Rachelle M Smith and Stanly B Williams. Circadian rhythms in gene transcription imparted by chromosome compaction in the cyanobacterium synechococcus elongatus. *Proceedings of the National Academy of Sciences*, 103(22):8564–8569, 2006.

[26] Yan Ouyang, Carol R Andersson, Takao Kondo, Susan S Golden, and Carl Hirschie Johnson. Resonating circadian clocks enhance fitness in cyanobacteria. *Proceedings of the National Academy of Sciences*, 95(15):8660–8664, 1998.

[27] Francesca Fagiani, Daniele Di Marino, Alice Romagnoli, Cristina Travelli, Davide Voltan, Lorenzo Di Cesare Mannelli, Marco Racchi, Stefano Govoni, and Cristina Lanni. Molecular regulations of circadian rhythm and implications for physiology and diseases. *Signal transduction and targeted therapy*, 7(1):41, 2022.

[28] Anna B Fishbein, Kristen L Knutson, Phyllis C Zee, et al. Circadian disruption and human health. *The Journal of clinical investigation*, 131(19), 2021.

[29] Emily NC Manoogian, Lisa S Chow, Pam R Taub, Blandine Laferrère, and Satchidananda Panda. Time-restricted eating for the prevention and management of metabolic diseases. *Endocrine reviews*, 43(2):405–436, 2022.

[30] Anneleen Segers and Inge Depoortere. Circadian clocks in the digestive system. *Nature Reviews Gastroenterology & Hepatology*, 18(4):239–251, 2021.

[31] Lauren Pickel and Hoon-Ki Sung. Feeding rhythms and the circadian regulation of metabolism. *Frontiers in nutrition*, 7:39, 2020.

[32] Frank AJL Scheer, Michael F Hilton, Christos S Mantzoros, and Steven A Shea. Adverse metabolic and cardiovascular consequences of circadian misalignment. *Proceedings of the National Academy of Sciences*, 106(11):4453–4458, 2009.

[33] Dirk Jan Stenvers, Frank AJL Scheer, Patrick Schrauwen, Susanne E la Fleur, and Andries Kalsbeek. Circadian clocks and insulin resistance. *Nature Reviews Endocrinology*, 15(2):75–89, 2019.

[34] Federica Catalano, Francesca De Vito, Velia Cassano, Teresa Vanessa Fiorentino, Angela Sciacqua, and Marta Letizia Hribal. Circadian clock desynchronization and insulin resistance. *International Journal of Environmental Research and Public Health*, 20(1):29, 2023.

[35] Soo Ji Kim, Chris Chi, Gopal Pattanayak, Aaron R Dinner, and Michael J Rust. Kida, a multi-pas domain protein, tunes the period of the cyanobacterial circadian oscillator. *Proceedings of the National Academy of Sciences*, 119(37):e2202426119, 2022.

[36] Eugene Leypunskiy, Jenny Lin, Haneul Yoo, UnJin Lee, Aaron R Dinner, and Michael J Rust. The cyanobacterial circadian clock follows midday in vivo and in vitro. *Elife*, 6:e23539, 2017.

[37] Archana G Chavan, Jeffrey A Swan, Joel Heisler, Cigdem Sancar, Dustin C Ernst, Mingxu Fang, Joseph G Palacios, Rebecca K Spangler, Clive R Bagshaw, Sarvind Tripathi, et al. Reconstitution of an intact clock reveals mechanisms of circadian timekeeping. *Science*, 374(6564):eabd4453, 2021.

[38] Roger Tseng, Nicolette F Goularte, Archana Chavan, Jansen Luu, Susan E Cohen, Yong-Gang Chang, Joel Heisler, Sheng Li, Alicia K Michael, Sarvind Tripathi, et al. Structural basis of the day-night transition in a bacterial circadian clock. *Science*, 355(6330):1174–1180, 2017.

[39] Fábio Madeira, Young Mi Park, Joon Lee, Nicola Buso, Tamer Gur, Nandana Madhusoodanan, Prasad Basutkar, Adrian RN Tivey, Simon C Potter, Robert D Finn, et al. The embl-ebi search and sequence analysis tools apis in 2019. *Nucleic acids research*, 47(W1):W636–W641, 2019.

[40] Ute Römling, Michael Y Galperin, and Mark Gomelsky. Cyclic di-gmp: the first 25 years of a universal bacterial second messenger. *Microbiology and Molecular Biology Reviews*, 77(1):1–52, 2013.

[41] Ryan K Shultzaberger, Joseph S Boyd, Spencer Diamond, Ralph J Greenspan, and Susan S Golden. Giving time purpose: The s. elongatus clock in a broader network context. *Annual review of genetics*, 49:485, 2015.

[42] Mitsunori Katayama, Takao Kondo, Jin Xiong, and Susan S Golden. ldpa encodes an iron-sulfur protein involved in light-dependent modulation of the circadian period in the cyanobacterium synechococcus elongatus pcc 7942, 2003.

[43] Oliver Schmitz, Mitsunori Katayama, Stanly B Williams, Takao Kondo, and Susan S Golden. Cika, a bacteriophytochrome that resets the cyanobacterial circadian clock. *Science*, 289(5480):765–768, 2000.

[44] Hideo Iwasaki, Stanly B Williams, Yohko Kitayama, Masahiro Ishiura, Susan S Golden, and Takao Kondo. A kaic-interacting sensory histidine kinase, sasa, necessary to sustain robust circadian oscillation in cyanobacteria. *Cell*, 101(2):223–233, 2000.

[45] Lawrence A Kelley, Stefans Mezulis, Christopher M Yates, Mark N Wass, and Michael JE Sternberg. The phyre2 web portal for protein modeling, prediction and analysis. *Nature protocols*, 10(6):845–858, 2015.

[46] Jonathan T Henry and Sean Crosson. Ligand binding pas domains in a genomic, cellular, and structural context. *Annual review of microbiology*, 65:261, 2011.

[47] Joel Heisler, Jeffrey A Swan, Joseph G Palacios, Cigdem Sancar, Dustin C Ernst, Rebecca K Spangler, Clive R Bagshaw, Sarvind Tripathi, Priya Crosby, Susan S Golden, et al. Structural mimicry confers robustness in the cyanobacterial circadian clock. *BioRxiv*, 2020.

[48] Kazuki Terauchi, Yohko Kitayama, Taeko Nishiwaki, Kumiko Miwa, Yoriko Murayama, Tokitaka Oyama, and Takao Kondo. Atpase activity of kaic determines the basic timing for circadian clock of cyanobacteria. *Proceedings of the National Academy of Sciences*, 104(41):16377–16381, 2007.

[49] Jun Abe, Takuya B Hiyama, Atsushi Mukaiyama, Seyoung Son, Toshifumi Mori, Shinji Saito, Masato Osako, Julie Wolanin, Eiki Yamashita, Takao Kondo, et al. Atomic-scale origins of slowness in the cyanobacterial circadian clock. *Science*, 349(6245):312–316, 2015.

[50] Joris Paijmans, David K Lubensky, and Pieter Rein Ten Wolde. A thermodynamically consistent model of the post-translational kai circadian clock. *PLoS computational biology*, 13(3):e1005415, 2017.

[51] Silvia A Bustos and Susan S Golden. Expression of the psbdii gene in synechococcus sp. strain pcc 7942 requires sequences downstream of the transcription start site. *Journal of bacteriology*, 173(23):7525–7533, 1991.

[52] Connie Phong, Joseph S Markson, Crystal M Wilhoite, and Michael J Rust. Robust and tunable circadian rhythms from differentially sensitive catalytic domains. *Proceedings of the National Academy of Sciences*, 110(3):1124–1129, 2013.

[53] Jenny Lin, Justin Chew, Udaysankar Chockanathan, and Michael J Rust. Mixtures of opposing phosphorylations within hexamers precisely time feedback in the cyanobacterial circadian clock. *Proceedings of the National Academy of Sciences*, 111(37):E3937–E3945, 2014.

[54] Yong-Gang Chang, Roger Tseng, Nai-Wei Kuo, and Andy LiWang. Rhythmic ring–ring stacking drives the circadian oscillator clockwise. *Proceedings of the National Academy of Sciences*, 109(42):16847–16851, 2012.

[55] Joel Heisler, Archana Chavan, Yong-Gang Chang, and Andy LiWang. Real-time in vitro fluorescence anisotropy of the cyanobacterial circadian clock. In *Circadian Clocks*, pages 3–18. Springer, 2021.

[56] Lu Hong, Danylo O Lavrentovich, Archana Chavan, Eugene Leypunskiy, Eileen Li, Charles Matthews, Andy LiWang, Michael J Rust, and Aaron R Dinner. Bayesian modeling reveals metabolite-dependent ultrasensitivity in the cyanobacterial circadian clock. *Molecular systems biology*, 16(6):e9355, 2020.

[57] Kumiko Ito-Miwa, Yoshihiko Furuike, Shuji Akiyama, and Takao Kondo. Tuning the circadian period of cyanobacteria up to 6.6 days by the single amino acid substitutions in kaic. *Proceedings of the National Academy of Sciences*, 117(34):20926–20931, 2020.

[58] Urs Jenal, Alberto Reinders, and Christian Lori. Cyclic di-gmp: second messenger extraordinaire. *Nature Reviews Microbiology*, 15(5):271–284, 2017.

[59] Rami Parnasa, Elad Nagar, Eleonora Sendersky, Ziv Reich, Ryan Simkovsky, Susan Golden, and Rakefet Schwarz. Small secreted proteins enable biofilm development in the cyanobacterium synechococcus elongatus. *Scientific reports*, 6(1):1–10, 2016.

[60] Thomas H Mann and Lucy Shapiro. Integration of cell cycle signals by multi-pas domain kinases. *Proceedings of the National Academy of Sciences*, 115(30):E7166–E7173, 2018.

[61] Andreas Möglich, Rebecca A Ayers, and Keith Moffat. Structure and signaling mechanism of per-arnt-sim domains. *Structure*, 17(10):1282–1294, 2009.

[62] Zheng Eelderink-Chen, Jasper Bosman, Francesca Sartor, Antony N Dodd, Ákos T Kovács, and Martha Merrow. A circadian clock in a nonphotosynthetic prokaryote. *Science advances*, 7(2):eabe2086, 2021.

[63] Maria Loza-Correa, Tobias Sahr, Monica Rolando, Craig Daniels, Pierre Petit, Tania Skarina, Laura Gomez Valero, Delphine Dervins-Ravault, Nadine Honoré, Aleksey Savchenko, et al. The l egionella pneumophila kai operon is implicated in stress response and confers fitness in competitive environments. *Environmental microbiology*, 16(2):359–381, 2014.

[64] Susan S Golden, Judy Brusslan, and Robert Haselkorn. Expression of a family of psba genes encoding a photosystem ii polypeptide in the cyanobacterium anacystis nidulans r2. *The EMBO journal*, 5(11):2789–2798, 1986.

[65] Shannon R Mackey, Jayna L Ditty, Eugenia M Clerico, and Susan S Golden. Detection of rhythmic bioluminescence from luciferase reporters in cyanobacteria. In *Circadian Rhythms*, pages 115–129. Springer, 2007.

[66] Gopal K Pattanayak, Guillaume Lambert, Kevin Bernat, and Michael J Rust. Controlling the cyanobacterial clock by synthetically rewiring metabolism. *Cell reports*, 13(11):2362–2367, 2015.

[67] Lukas Käll, John D Storey, and William Stafford Noble. Non-parametric estimation of posterior error probabilities associated with peptides identified by tandem mass spectrometry. *Bioinformatics*, 24(16):i42–i48, 2008.

[68] William Humphrey, Andrew Dalke, and Klaus Schulten. Vmd: visual molecular dynamics. *Journal of molecular graphics*, 14(1):33–38, 1996.

[69] Jonathan Goodman and Jonathan Weare. Ensemble samplers with affine invariance. *Communications in applied mathematics and computational science*, 5(1):65–80, 2010.

[70] Gabriela Da Silva Xavier. The cells of the islets of langerhans. *Journal of clinical medicine*, 7(3):54, 2018.

[71] Jonathan E Campbell and Christopher B Newgard. Mechanisms controlling pancreatic islet cell function in insulin secretion. *Nature reviews Molecular cell biology*, 22(2):142–158, 2021.

[72] Cara Ellis, Adam Ramzy, and Timothy J Kieffer. Regenerative medicine and cell-based approaches to restore pancreatic function. *Nature reviews Gastroenterology & hepatology*, 14(10):612–628, 2017.

[73] Morris F White and C Ronald Kahn. Insulin action at a molecular level–100 years of progress. *Molecular Metabolism*, 52:101304, 2021.

[74] Gary F Lewis, Andre C Carpentier, Sandra Pereira, Margaret Hahn, and Adria Giacca. Direct and indirect control of hepatic glucose production by insulin. *Cell metabolism*, 33(4):709–720, 2021.

[75] Philippe A Halban, Kenneth S Polonsky, Donald W Bowden, Meredith A Hawkins, Charlotte Ling, Kieren J Mather, Alvin C Powers, Christopher J Rhodes, Lori Sussel, and Gordon C Weir. β-cell failure in type 2 diabetes: postulated mechanisms and prospects for prevention and treatment. *The Journal of Clinical Endocrinology & Metabolism*, 99(6):1983–1992, 2014.

[76] Jay S Skyler, George L Bakris, Ezio Bonifacio, Tamara Darsow, Robert H Eckel, Leif Groop, Per-Henrik Groop, Yehuda Handelsman, Richard A Insel, Chantal Mathieu, et al. Differentiation of diabetes by pathophysiology, natural history, and prognosis. *Diabetes*, 66(2):241–255, 2017.

[77] Unai Galicia-Garcia, Asier Benito-Vicente, Shifa Jebari, Asier Larrea-Sebal, Haziq Siddiqi, Kepa B Uribe, Helena Ostolaza, and César Martín. Pathophysiology of type 2 diabetes mellitus. *International journal of molecular sciences*, 21(17):6275, 2020.

[78] Mohammed Bensellam, D Ross Laybutt, and Jean-Christophe Jonas. The molecular mechanisms of pancreatic β-cell glucotoxicity: recent findings and future research directions. *Molecular and cellular endocrinology*, 364(1-2):1–27, 2012.

[79] Ioulia B Efanova, Sergei V Zaitsev, Boris Zhivotovsky, Martin Köhler, Suad Efendić, Sten Orrenius, and Per-Olof Berggren. Glucose and tolbutamide induce apoptosis in pancreatic β-cells: a process dependent on intracellular ca2+ concentration. *Journal of Biological Chemistry*, 273(50):33501–33507, 1998.

[80] Mohammed Bensellam, Leentje Van Lommel, Lutgart Overbergh, FC Schuit, and Jean-Christophe Jonas. Cluster analysis of rat pancreatic islet gene mrna levels after culture in low-, intermediate-and high-glucose concentrations. *Diabetologia*, 52:463–476, 2009.

[81] MZ Khaldi, Yves Guiot, Patrick Gilon, Jean-Claude Henquin, and Jean-Christophe Jonas. Increased glucose sensitivity of both triggering and amplifying pathways of insulin secretion in rat islets cultured for 1 wk in high glucose. *American Journal of Physiology-Endocrinology and Metabolism*, 287(2):E207–E217, 2004.

[82] Jean-Christophe Jonas, Mohammed Bensellam, Jessica Duprez, Hajar Elouil, Yves Guiot, and SMA Pascal. Glucose regulation of islet stress responses and β-cell failure in type 2 diabetes. *Diabetes, obesity and metabolism*, 11:65–81, 2009.

[83] Biliana Marcheva, Kathryn Moynihan Ramsey, Ethan D Buhr, Yumiko Kobayashi, Hong Su, Caroline H Ko, Ganka Ivanova, Chiaki Omura, Shelley Mo, Martha H Vitaterna, et al. Disruption of the clock components clock and bmal1 leads to hypoinsulinaemia and diabetes. *Nature*, 466(7306):627–631, 2010.

[84] Mark Perelis, Biliana Marcheva, Kathryn Moynihan Ramsey, Matthew J Schipma, Alan L Hutchison, Akihiko Taguchi, Clara Bien Peek, Heekyung Hong, Wenyu Huang, Chiaki Omura, et al. Pancreatic β cell enhancers regulate rhythmic transcription of genes controlling insulin secretion. *Science*, 350(6261):aac4250, 2015.

[85] Vincent Poitout, L Karl Olson, R Paul Robertson, et al. Chronic exposure of betatc-6 cells to supraphysiologic concentrations of glucose decreases binding of the ripe3b1 insulin gene transcription activator. *The Journal of clinical investigation*, 97(4):1041–1046, 1996.

[86] V Poitout, LK Olson, and RP Robertson. Insulin-secreting cell lines: classification, characteristics and potential applications. *Diabetes & metabolism*, 22(1):7–14, 1996.

[87] Masa Skelin, Marjan Rupnik, and Avrelija Cencič. Pancreatic beta cell lines and their applications in diabetes mellitus research. *ALTEX-Alternatives to animal experimentation*, 27(2):105–113, 2010.

[88] Panagiotis D Venieratos, Garyfalia I Drossopoulou, Katerina D Kapodistria, Effie C Tsilibary, and Paraskevi V Kitsiou. High glucose induces suppression of insulin signalling and apoptosis via upregulation of endogenous il-1β and suppressor of cytokine signalling-1 in mouse pancreatic beta cells. *Cellular signalling*, 22(5):791–800, 2010.

[89] Rosalinda Madonna, Yong-Jian Geng, Harnath Shelat, Peter Ferdinandy, and Raffaele De Caterina. High glucose-induced hyperosmolarity impacts proliferation, cytoskeleton remodeling and migration of human induced pluripotent stem cells via aquaporin-1. *Biochimica et Biophysica Acta (BBA)-Molecular Basis of Disease*, 1842(11):2266–2275, 2014.

[90] Omer Karin and Uri Alon. Biphasic response as a mechanism against mutant takeover in tissue homeostasis circuits. *Molecular systems biology*, 13(6):933, 2017.

[91] Martina Valentini and Alain Filloux. Biofilms and cyclic di-gmp (c-di-gmp) signaling: lessons from pseudomonas aeruginosa and other bacteria. *Journal of Biological Chemistry*, 291(24):12547–12555, 2016.

[92] Daniella Schatz, Elad Nagar, Eleonora Sendersky, Rami Parnasa, Shaul Zilberman, Shmuel Carmeli, Yitzhak Mastai, Eyal Shimoni, Eugenia Klein, Orna Yeger, et al. Self-suppression of biofilm formation in the cyanobacterium s ynechococcus elongatus. *Environmental microbiology*, 15(6):1786–1794, 2013.

[93] Ryo Iwase, Katsumi Imada, Fumio Hayashi, Tatsuya Uzumaki, Megumi Morishita, Kiyoshi Onai, Yukio Furukawa, Keiichi Namba, and Masahiro Ishiura. Functionally important substructures of circadian clock protein kaib in a unique tetramer complex. *Journal of Biological Chemistry*, 280(52):43141–43149, 2005.

[94] John Jumper, Richard Evans, Alexander Pritzel, Tim Green, Michael Figurnov, Olaf Ronneberger, Kathryn Tunyasuvunakool, Russ Bates, Augustin Žídek, Anna Potapenko, et al. Highly accurate protein structure prediction with alphafold. *Nature*, 596(7873):583–589, 2021.

[95] Mihaly Varadi, Stephen Anyango, Mandar Deshpande, Sreenath Nair, Cindy Natassia, Galabina Yordanova, David Yuan, Oana Stroe, Gemma Wood, Agata Laydon, et al. Alphafold protein structure database: massively expanding the structural coverage of protein-sequence space with high-accuracy models. *Nucleic acids research*, 50(D1):D439–D444, 2022.

[96] Andreas Winkler, Udo Heintz, Robert Lindner, Jochen Reinstein, Robert L Shoeman, and Ilme Schlichting. A ternary appa–ppsr–dna complex mediates light regulation of photosynthesis-related gene expression. *Nature structural & molecular biology*, 20(7):859–867, 2013.

[97] Jason Key, Marco Hefti, Erin B Purcell, and Keith Moffat. Structure of the redox sensor domain of azotobacter vinelandii nifl at atomic resolution: signaling, dimerization, and mechanism. *Biochemistry*, 46(12):3614–3623, 2007.

[98] Schrödinger, LLC. The PyMOL molecular graphics system, version 2.1.1. March 2018.

[99] Veronika Angerer, Philipp Schwenk, Thomas Wallner, Volkhard Kaever, Andreas Hiltbrunner, and Annegret Wilde. The protein slr1143 is an active diguanylate cyclase in synechocystis sp. pcc 6803 and interacts with the photoreceptor cph2. *Microbiology*, 163(6):920–930, 2017.

[100] Alex Boehm, Matthias Kaiser, Hui Li, Christian Spangler, Christoph Alexander Kasper, Martin Ackermann, Volkhard Kaever, Victor Sourjik, Volker Roth, and Urs Jenal. Second messenger-mediated adjustment of bacterial swimming velocity. *Cell*, 141(1):107–116, 2010.